**Title**

Mechanical modes of amoeboid cell migration : role of F-actin polymerization, F-actin crosslinking and substrate properties

**Author**

Bastounis, Effie Efthymia

**Publication Date**

2012

UNIVERSITY OF CALIFORNIA, SAN DIEGO

# Mechanical Modes of Amoeboid Cell Migration: Role of F-actin Polymerization, F-actin Crosslinking and Substrate Properties

A dissertation submitted in partial satisfaction of the
requirements for the degree Doctor of Philosophy

in

Bioengineering

by

Effie Efthymia Bastounis

Committee in charge:

Juan C. Lasheras, Chair
Shu Chien, Co-Chair
James Butler
Juan C. del Álamo
Richard Firtel
Ruedi Meili
Geert Schmid-Schönbein

2012

The Dissertation of Effie Efthymia Bastounis is approved and it is acceptable in quality and form for publication in microfilm and electronically:

Co-Chair

Chair

University of California, San Diego

2012

# DEDICATION

To my parents, Elias and Argyro

# EPIGRAPH

I know one thing, that I know nothing.

Ἓν οἶδα ὅτι οὐδὲν οἶδα.

Socrates 469-399 B.C.

# TABLE OF CONTENTS

# LIST OF FIGURES

# LIST OF TABLES

# NOMECLATURE

| | |
|---|---|
| $A$ | Time average area of a cell (μm$^2$) |
| $A_{cell}$ | Average cell area during the last three observations (pixels) |
| $A_{features}$ | Area of features detected after application of threshold (pixels) |
| Abp120 | Protein Abp120 or Filamin A, which is an F-actin crosslinker |
| $AF$ | Area flux (μm$^2$/s) |
| $AF_{deform}$ | Area flux of deformation (μm$^2$/s) |
| $AF_{trans}$ | Area flux translocation (μm$^2$/s) |
| AFM | Atomic force microscope |
| APS | Ammonium persulfate, initiator of polymerization of acrylamide |
| $AR$ | Time average aspect ratio of a cell (Cell length/Cell width) |
| $abp120^-$ | Abp120 (Filamin A) null cell |
| a.f. | Actin focus or actin bright spot, located at the ventral side of a cell |
| $\alpha$ | Wavenumber in x-direction |
| $\alpha_0$ | Function for the calculation of the Young's modulus |
| $\beta$ | Wavenumber in y-direction |
| $\beta_0$ | Function for the calculation of the Young's modulus |
| cAMP | Cyclic adenosine monophosphate used as chemoattractant |
| DC | Detergent compatible |
| DIC | Digital interference contrast microscopy |
| $DOP$ | Degree of periodicity of a time record expressed as percentage (%) |
| $\Delta\tau_{U\_L}$ | Time delay between strain energy, $U_s(t)$ and cell length, $L(t)$ (s) |
| $\Delta\tau_{L\_G}$ | Time delay between cell length, $L(t)$ and maximum frontal fluorescence, $G_{max}(t)$ (s) |
| $\Delta\tau$ | Time duration of a motility mode (s) |
| $\Delta z$ | Distance between consecutive z-axis focal planes (μm) |
| $\delta z$ | Indentation depth of Tungsten carbide sphere (μm) |
| E | Young's modulus of the polyacrylamide substrate (Pa) |
| $E_{AFM}$ | Young's modulus of the polyacrylamide substrate measured through AFM |
| $E_{IND}$ | Young's modulus of the polyacrylamide substrate determined through the indentation of the Tungsten carbide sphere |
| $E_{REF}$ | Young's modulus of the polyacrylamide substrate predicted by Engler et al |
| ECM | Extracellular matrix |
| $\varepsilon$ | Perturbation parameter |

| | |
|---|---|
| $\bar{\boldsymbol{\varepsilon}}$ | Strain tensor |
| $\boldsymbol{F_b}$ | Average values of the axial stresses exerted by the cell in its back half (nN) |
| $\boldsymbol{F_f}$ | Average values of the axial stresses exerted by the cell in its frontal half (nN) |
| $\boldsymbol{F_l}$ | Average values of the lateral stresses exerted by the cell in its lower half (nN) |
| $\boldsymbol{F_u}$ | Average values of the lateral stresses exerted by the cell in its upper half (nN) |
| $\boldsymbol{F_y}$ | Lateral contractility (nN) |
| $\boldsymbol{F_x}$ | Axial contractility (nN) |
| FTFM | Fourier traction force microscopy |
| $f$ | Frequency of a signal's oscillations determined by fitting it to a sinusoidal function |
| $\varphi$ | Phase of the sinusoidal function that best fits a time record |
| $\phi$ | Angle between cell longitudinal axis and x-axis of laboratory reference frame (rad) |
| G-G | Gliding-Gliding motility mode |
| GFP | Green fluorescent protein |
| G-S | Gliding-Stepping motility mode |
| $g$ | *Lifeact* fluorescence intensity field |
| $H$ | Polynomial fit to the histogram of $I$ |
| HEPES | Zwitterionic organic chemical buffering agent |
| $h$ | Substrate thickness (μm) |
| $h_0$ | Vertical location of fluorescent beads plane (μm) |
| $\eta$ | Vertical coordinate in cell based reference system |
| $I$ | Cell width (μm) |
| $I_1$ | Inferior limit of the intensity region to determine threshold $I_{thr}$ (-) |
| $I_2$ | Superior limit of the intensity region to determine threshold $I_{thr}$ (-) |
| $I_0$ | Location of the global maximum of $H(I)$ |
| $I_{ave}$ | Average intensity field of DIC images used to remove the background from the original |
| $I_{inter}$ | Intensity of the intermediate image resulting after subtracting from the original the average |
| $I_{orig}$ | Intensity field of the original DIC image |
| $I_{thr}$ | Threshold intensity for cell segmentation |
| $J$ | Integral across the cell width of *Lifeact* fluorescence intensity |
| $L$ | Cell length (μm) |
| *Lifeact* | Abp140-GFP, a 17 amino-acid peptide which binds F-actin |
| $\lambda$ | Step length of the motility cycle (μm) |

| | |
|---|---|
| MyoII | Protein myosin II |
| $mhcA^-$ | Myosin II heavy chain null cell |
| $N$ | Number of cells |
| NPF | Nucleation Promoting Factor |
| NS | Nearly Stationary motility mode |
| PBS | Phosphate buffered saline |
| PIR121 | Protein Pir121 of the Scar/Wave complex |
| P.A. | Protein amount of a cell (μm/cell) |
| $pirA^-$ | Pir121 null cell |
| poly-L-Lys | Natural homopolymer ε-poly-L-lysine, used to increase cell adherence |
| R | Radius of tungsten carbide sphere (μm) |
| $R_{L\_L}$ | Autocorrelation function of the cell length |
| $R_{L\_G}$ | Cross-correlation function of the cell length, $L(t)$ with the maximum fluorescence intensity at the front of the cells, $G_{max}(t)$ |
| $R_{L\_U}$ | Cross-correlation function of the cell length, $L(t)$ with the strain energy, $U_s(t)$ |
| RMSE | Root mean square error |
| Roco2 | *LRRK2*-related Roco kinase protein |
| $roco2^-$ | Roco2 null cell |
| SCAR | Protein Scar of the Scar/Wave complex |
| SCAR/WAVE | Pentameric protein complex that through activation of the Arp2/3 complex promotes the dendritic polymerization of F-actin |
| S-G | Stepping-Glidiing motility mode |
| S-S | Stepping-Stepping motility mode |
| $S_0$ | Size of first structuring element (pixels) |
| $S_1$ | Size of second structuring element (pixels) |
| Sulfo-Sanpah | Protein crosslinker used to covalently bind proteins to the polyacrylamide gels |
| $scrA^-$ | Scar null cell |
| s.d. | Stress disk |
| $\sigma$ | Poisson's ratio |
| $\boldsymbol{T}$ | Traction Tension (nN/μm) |
| $T$ | Period of the oscillations of a time record determined by fitting it to a sinusoidal function |
| $T_0$ | Period of the oscillations of a time record determined through its autocorrelation function |

| | |
|---|---|
| $T_G$ | Period of the oscillations of the maximum fluorescence intensity at the front of the cells, $G_{max}(t)$ (s) |
| $T_i$ | Duration of the phases of the motility cycle (s) |
| $T_L$ | Period of the oscillations of the cell length, $L(t)$ (s) |
| $T_{mode}$ | Period of the oscillations of a time record during a specific motility mode (s) |
| $T_U$ | Period of the oscillations of the strain energy, $U_s(t)$ (s) |
| TEMED | Tetramethylethylenediamine, catalyst of polymerization of acrylamide |
| $\bar{\boldsymbol{\tau}}$ | Stress tensor (Pa) |
| $\boldsymbol{\tau}$ | Stress vector field at substrate free surface ($\tau_{zx}$, $\tau_{zy}$, $\tau_{zz}$) (Pa) |
| $\hat{\boldsymbol{\tau}}_{\boldsymbol{\alpha},\boldsymbol{\beta}}$ | Fourier coefficients of $\boldsymbol{\tau}$ (μm) |
| $\tau_{ik}$ | Stress tensor (Einstein's notation) (Pa) |
| $U_s$ | Strain energy exerted on the substrate (pNμm) |
| $u$ | Horizontal displacement in the x-direction |
| $\boldsymbol{u}$ | Displacement vector field (μm) |
| $\hat{\boldsymbol{u}}_{\boldsymbol{\alpha},\boldsymbol{\beta}}$ | Fourier coefficients of $\boldsymbol{u}$ (μm) |
| $\upsilon$ | Horizontal displacement in the y-direction |
| $\upsilon_{ij}$ | Strain tensor (Einstein's notation) |
| $V$ | Velocity of migration of the cell (centroid) (μm/min) |
| $V_i$ | Velocity of migration of each phase of the motility cycle (centroid) (μm/min) |
| $v$ | Horizontal displacement in the x-direction |
| $\omega$ | Angular frequency of the oscillations of a time record (rad/s) |
| $W$ | Apparent weight of tungsten carbide sphere used (μN) |
| WT | Wild-type cell |
| $w$ | Vertical displacement (μm) |
| $x_c$ | $x$-coordinate of cell centroid |
| $\xi$ | Horizontal coordinate in cell based reference frame |
| $\mathrm{y}$ | Horizontal coordinate parallel to the gel surface laboratory reference frame (μm) |
| $y_c$ | $y$-coordinate of cell centroid (μm) |
| $\mathrm{z}$ | Vertical coordinate perpendicular to the substrate (μm) |
| $\mathrm{z}_1$ | Vertical location of the measurement plane (μm) |

# ACKNOWLEDGEMENTS

Looking back at the last six years of my life, I realize how much support I've received from various people throughout these years, and I would like to acknowledge them. Without their contributions and help, this Dissertation would not have been possible. In addition, my interactions with them have certainly shaped me as a person and have led me to where I am today.

Firstly, I am deeply grateful to Professor Juan C. Lasheras, my advisor, for giving me the confidence to work with him. His support, guidance, perceptiveness, advice and feedback were invaluable. Joining his research group at UCSD is the reason I could accomplish my PhD in this exceptional and renowned institution. I also want to thank my co-advisor, Professor Richard Firtel, in the Section of Cell and Developmental Biology at UCSD, with whom I had the opportunity to be trained and work in a biology laboratory and perform these multidisciplinary studies. I am grateful for his wise guidance, insightful advice, discussions and continuous support throughout all the years of my PhD studies.

I would also like to gratefully acknowledge the continuous supervision of Professor Juan C. del Álamo, with whom I have had the fortune to work and receive guidance and help throughout the years I was studying at UCSD. Most of the codes and computational techniques used or developed for the purposes of my studies, were either provided by him or made due to his invaluable advice and ideas. Although officially he was not my co-advisor, I consider him as my third advisor, and I am grateful to him.

Thanks to Ruedi Meili, who spent a lot of time patiently teaching me most of the biological techniques and methods I used during these five years. Prior to my PhD studies, I did not have a strong biological background; thus, the studies I performed during these five years, would not have been possible without his invaluable input, ideas and help. Thanks also to Baldomero Alonso-Latorre, for being my mentor in the mechanical and technical part of my studies, back when he was a graduate student at our lab. I consider myself really fortunate to have had such a patient and knowledgeable teacher as Baldo, who tolerated my numerous questions on a daily basis, and who always offered his advice and guidance willingly both in a scientific, and on occasion, more personal level.

There are many more people that I would like to thank not only for their scientific help, but also personal throughout these five years in San Diego. Among them, I would like to thank Professor James Butler and Professor Shu Chien, both members of my thesis committee, for their helpful advice and support. Thanks also to Alexis Lasheras, whose help was invaluable throughout my five-year studies. She carefully edited all my scientific papers, including the present Dissertation. Moreover, Alexis contributed significantly in teaching me how to write scientific papers in English and also patiently guided me on how to organize my ideas and data before starting to write a paper. I want to thank her for her encouragement, optimism and support in times that I really needed it. I also would like to thank Christos Tzitzilonis, for his moral, emotional and scientific support and for being, among other things, my best friend throughout these years.

Finally, my parents, Argyro and Elias Bastounis, have been a constant source of support, encouragement and unflagging love. Without them, this thesis would certainly not have existed. It is thanks to my father, that I first became interested in biomedical science and thanks to my mother and her patience, that I managed to carry on my studies through periods that were hard for me.

San Diego, California. 25 November, 2012.

Chapters 2 in part, has been published in the Conference Proceedings of the IEEE Engineering in Medicine and Biology Society. Distribution of traction forces associated with shape changes during amoeboid cell migration. Alonso-Latorre B., Meili R., Bastounis E., del Álamo J.C., Firtel R., Lasheras J.C. (2009: 3346-3349). In addition the Traction Force Cytometry method presented has been published in the Proceedings of the National Academy of Sciences of the United States of America. Spatio-temporal analysis of eukaryotic cell motility by improved force cytometry. del Álamo J.C., Meili R., Alonso-Latorre B., Rodriguez-Rodriguez J., Aliseda A., Firtel R., and Lasheras J.C. (2007: (104), 13343-13348).

Chapters 3 and 4 have been published in part in the Molecular Biology of the Cell journal, "The SCAR/WAVE complex is necessary for proper regulation of traction stresses during amoeboid motility", by Bastounis E., Alonso-Latorre B., Meili R., del Álamo J.C., Firtel R. and Lasheras J.C. (2011: (22), 3995-4003).

Chapters 3, 6 and 7 in part are being prepared for publication, "Chemotaxing amoeboid cells migrate by switching between distinct modes of adhesion dynamics and contractility", by Bastounis E., Meili R., Álvarez-González B., del Álamo J.C., Meili R., Firtel R., Lasheras J.C..

This investigation was partially funded by the U.S. National Institutes of Health.

# VITA

| | |
|---|---|
| February-July, 2006 | Erasmus Scholarship,<br>Department of Electrical Engineering,<br>Universidad Polytechnica de Valencia, Spain. |
| July, 2007 | Bachelor in Electrical and Computer Engineering,<br>Department of Electrical and Computer Engineering,<br>National Technical University of Athens, Greece. |
| August-December 2007 | Research Assistant,<br>Department of Mechanical Engineering,<br>University of Illinois at Urbana-Champaign, USA. |
| 2007-2009 | Teaching Assistant,<br>Department of Bioengineering,<br>University of California San Diego, USA. |
| 2007-2012 | Research Assistant,<br>Department of Bioengineering,<br>University of California San Diego, USA. |
| September 2010-April 2011 | HHMI Med into Grad Training Program,<br>School of Medicine,<br>University of California San Diego, USA. |
| December 2009 | Master of Science in Bioengineering,<br>Department of Bioengineering,<br>University of California San Diego, USA. |
| 2011-2012 | Awarded NHLBI Training Grant<br>Department of Bioengineering,<br>University of California San Diego, USA. |
| December 2012 | Doctor of Philosophy in Bioengineering,<br>Department of Bioengineering,<br>University of California San Diego, USA. |

# PUBLICATIONS

B. Alonso-Latorre, J.C. del Álamo, **E. Bastounis**, R. Meili, R. Firtel, J.C. Lasheras. Distribution of traction forces associated with shape changes during amoeboid cell migration. Conf. Proc. IEEE Eng. Med. Biol. Soc., 2009:3346-3349.
J.C. Lasheras, B. Alonso-Latorre, **E. Bastounis**, J.C. del Álamo, R. Meili, R. Firtel. Distribution of traction forces and intracellular markers associated with shape changes during amoeboid cell migration. Internat J Transport Phenomena, 2011: *(12)*, 3-12.
**E. Bastounis**, B. Alonso-Latorre, R. Meili, J.C. del Álamo, R. Firtel, J.C. Lasheras. The Scar/WAVE Complex is necessary for proper regulation of traction stresses during amoeboid motility. Mol Biol Cell, 2011: (22), 3995-4003.
*Cover image selected for the issue of October 15, 2011 in Mol Biol Cell
**Article selected among highlights of current issue

J.C. del Álamo, Meili, B. Álvarez-González, B. Alonso-Latorre, **E. Bastounis**, R. Meili, R. Firtel, J.C. Lasheras. Three-Dimensional Quantification of Cellular Traction Forces and Mechanosensing of Thin Substrata by Fourier Traction Force Microscopy. *PLoS ONE, 2012: (in press).*

**E. Bastounis**, R. Meili, B. Álvarez-González, J.C. del Álamo, R. Meili, R. Firtel, J.C. Lasheras. Chemotaxing amoeboid cells migrate by switching between distinct adhesion dynamics and contractility modes. (In preparation).

# FIELDS OF STUDY

Major Field: Bioengineering (focused on Biomechanics)

Studies in Biomechanics
Professors Gaudenz Danuser, Geert W. Schmid-Schönbein, Marcos Intaglietta and Juan C. Lasheras

Studies in Medical Imaging
Professor Thomas Liu

Studies in Microscopy Techniques
Professors Mark Ellisman, Maryann E. Martone, James Bouwer and Gina E. Sosinsky

Studies in Fluid Mechanics
Professors Eric Lauga and Daniel Tartakofsky

Studies in Tissue Engineering
Professors Christman Karen and Robert Sah

Studies in Cell Biology and Biochemistry
Professors Amy Sung and Michael Heller

Studies in Systems Biology
Professors Shankar Subramaniam

Studies in Biomedical Transport Phenomena
Professors Marcos Intaglietta and David Gough.

# ABSTRACT OF THE DISSERTATION

## Mechanical Modes of Amoeboid Cell Migration: Role of F-actin Polymerization, F-actin Crosslinking and Substrate Properties

by

Effie Efthymia Bastounis

Doctor of Philosophy in Bioengineering

University of California, San Diego, 2012

Professor Juan C. Lasheras, Chair
Professor Shu Chien, Co-Chair

Directed cell migration is involved in a broad spectrum of biological phenomena, ranging from the metastatic spreading of cancer to the active migration of neutrophils in response to bacterial infection. It requires a tightly regulated, spatiotemporal coordination of underlying biochemical processes. However, our understanding of how these processes are spatiotemporally coordinated with the mechanics of cell migration is poor. The objective of this Dissertation is, therefore, to investigate the mechanics of cell migration using Fourier Traction Force Microscopy (FTFM) measurements to shed light onto the key role of specific cytoskeletal proteins in the migration process.

Using an improved traction force cytometry method, we calculated the traction stresses of wild-type cells and a range of mutants with cytoskeletal deficiencies. We confirmed that for both wild type and mutants, the strength of the traction stresses and the cell length followed a quasi-periodic temporal evolution, supporting the existence of a motility cycle. In addition, we found that the cells with misregulated SCAR/WAVE-mediated, dendritic F-actin polymerization at the cell's leading edge were unable to move periodically, rendering their efficiency in migrating poor. We were able to

demonstrate that wild type and cells lacking the SCAR/WAVE complex protein PIR121 (*pirA*$^{-}$) or SCAR (*scrA*$^{-}$) exert stresses of different strength that correlate with their levels of F-actin, suggesting that the amount of F-actin present within a cell is a determinant of its stress strength.

In addition to FTFM, we also constructed traction tension kymographs to obtain a space-time representation of traction stresses. Kymographic representation of the traction stresses allowed us to determine, for the first time, how the formation and disassembly of adhesions are coupled with the generation of axial and lateral traction stresses to control cell migration. Our findings revealed that wild-type cells migrate by switching between two motility modes with distinct adhesion and contractility dynamics. These two modes are not conserved when wild-type cells migrate on highly adhesive substrates, where cells implement modes that rely on lateral contractility.

Finally, we observed that cells with cytoskeletal crosslinking defects (*mhcA*$^{-}$ and *abp120*$^{-}$ cells) also move by developing increased lateral contractility. However, under conditions of increased adherence, they were unable to move due to their inability to augment the strength of their traction stresses, break their back adhesions, and migrate forward.

# Chapter 1
# Introduction

## 1.1 Background

### 1.1.1 Cell migration is involved in many physiological and disease processes

Cell migration is crucial in a wide range of physiological processes essential to survival and life (1-3). For instance, embryonic development and organogenesis require the mobilization of cells to generate new structures and organs (4, 5). Furthermore, both immunity and wound healing are two homeostatic processes in the body that rely on the ability of cells to migrate (6, 7). During the immune response against pathogens, leukocytes from the circulation make their way through the walls of vessels and migrate into the surrounding infected tissue to engulf and destroy the pathogens. Similarly, wound healing, angiogenesis (new blood vessel formation) and re-epithelialization occur due to the proliferation and migration of vascular endothelial cells and epithelial cells respectively (8).

The failure of cells to migrate, or any inappropriate migratory movements, are key components of many serious and life-threatening diseases (9, 10). The metastatic spreading of cancer is such an example. Cancer cells characterized by increased motility, leave the initial site of tumor growth, enter the blood or lymph vessels and, then cross the vessel wall to exit the vasculature in distal organs where they can continue to proliferate forming a secondary tumor (11-13). Moreover, a key component to the development of many vascular diseases among which is atherosclerosis, is the migration and proliferation of vascular smooth muscle cells which lead to progressive vessel thickening (14). Subsequent vascular injury leads to endothelial dysfunction, which, in turn, promotes the expression of inflammatory markers and trans-endothelial leukocyte migration (15). Recruitment of leukocytes from the circulation into the vessel intima is a crucial step for the development of fibrous, atherosclerotic plaques (16). Many chronic inflammation processes (asthma, rheumatoid arthritis, multiple sclerosis, psoriasis) are characterized by the constant infiltration of immune cells into inappropriate places which, once they've reached and due to their activation, can cause massive damage and progressive deterioration of the tissue (17). Finally, understanding the mechanisms underlying cell migration is also important to emerging areas of biotechnology that focus on cellular transplantation and the engineering of artificial tissues, as well as to the development of new therapeutic strategies that aim at controlling invasive tumor cells (18, 19).

### 1.1.2 Cells can migrate in different ways

There are many ways cells can move (20). Similar to bacteria, some cells swim in the liquid environment in which they are found in order to propel themselves by using specialized structures (cilia, flagella) (20). Crawling over flat surfaces is another type of cell movement that can be further divided into lamellipodial and amoeboid crawling. In the case of lamellipodial motility, cells migrate by projecting a bi-dimensional, flat veil-shaped protrusion (lamella) with which they move forward together with the continuous retraction of their backs (21). Amoeboid motility refers to the locomotion of all eukaryotic cells that move by protruding their stubby three-dimensional leading edge, called pseudopodium. The migration of these cells consists of a limited repertoire of discrete movements - extension (pseudopods) and retractions (22). Finally, there are cells that move in three-dimensional matrices, as usually occurring in vivo, by projecting specialized structures called podosomes and invadopodia and at the same time by degrading their extracellular matrix (ECM) by means of various enzymes (23).

### 1.1.3 Traction force microscopy used to study the mechanics of cell migration

Several methods have been developed recentely in order to study the mechanics of cell locomotion (24-26). Some of them focus on the study of the traction stresses that the cells exert on the substrate over which they migrate, calculated from the resultant deformation field induced by the cells on the substrate. To this end, several authors relied on the classical solution of the elastostatic equation for a homogeneous, semi-infinite medium proposed by Boussinesq (27). This solution expresses the deformations as functions of the traction stresses and has to be inverted. Since that inversion leads to a numerically-stiff and computationally-expensive problem, Butler et. al inverted Boussinesq's solution, making it trivial in the Fourier space and proposed a spectral method to obtain a computationally-efficient solution of the elastostatic equation (28). Our group extended this method by taking into account the finite thickness of the substrate and the fine distance between the measurement plane and the surface of the substrate (29). Despite the advances made in this direction, there is still an important need to better understand the spatiotemporal integration of the biochemical together with the mechanical processes that lead to cell migration. In order to develop a better understanding of the relation between the mechanics and biochemistry sufficient to predict and control cell motility, each mechanical event characterizing the motility has to be associated with specific biochemical signalling events, thus enabling us to elucidate the effects that the regulation of these signalling pathways has on the mechanics of cell motility.

### 1.1.4 Additional techniques used to examine the spatiotemporal organization of traction stresses and localization of fluorescent protein markers

In the present study a variety of methods and analytical techniques are used to examine the spatiotemporal organization of traction stresses and the localization of fluorescent markers, which tag specific cytoskeletal proteins. As mentioned in the previous section, applying Fourier Traction Force Microscopy (FTFM) and using additional novel Microscopy technics, we measure traction stresses and 3D shape changes with high temporal resolution. By stacking the traction stress measurements jointly in space and time, we obtain kymographs of the traction tension of cells, which enables us to look at the traction adhesion dynamics of motility. In addition, using these kymographs we classify motility into different modes depending on the traction adhesion dynamics of the cells with an unprecedented level of detail. By quantitatively dissecting the dynamics of amoeboid motility into modes and comparing wild-type cells with mutants with defects in their cytoskeletal organization or with cells moving on substrates with altered mechanical properties, we gain further insight into the mechanics of cell locomotion.

In addition to the kymographic analysis of traction stresses, we apply techniques previously developed and applied (29-31) to analyze whether the migrating cells, in addition to the traction adhesion modes they implement during migration, they also follow a motility cycle characterized by periodic oscillations of their cells shape and strain energy (2, 32-34). We first characterize the degree of periodicity of various mechanical and biochemical signals and then analyze their temporal relationship (35). In addition by transforming the fields of the traction stresses and of the fluorescence localization of any protein marker, from the lab-based to a cell-based dimensionless coordinate system, we calculate average traction stress maps of many cells and thus compare different strains but also same strains migrating under different conditions. Finally, for cells exhibiting a motility cycle during migration, we apply conditional statistics based on the oscillations of the cell length and dissect motility into phases. We then compile averages of various fields such as of the traction stresses and the localization of fluorescent protein markers. We thus examine the relationship between the mechanics of cell migration and the underling biochemistry.

### 1.1.5 *Dictyostelium discoideum* as model organism for studying the mechanics of cell migration

We apply the aforementioned techniques to study cell locomotion by using the social amoeba *Dictyostelium discoideum* as our model organism. *Dictyostelium* shares many mechanical traits of its migration and chemotaxis with motile mammalian cells such as neutrophils and macrophages (36); the conservation of the basic principles extends to the biochemical level where many proteins involved in motility of metazoans are conserved as well. The experimental advantages of using *Dictyostelium* as a model system stem from the combination of multiple factors: *Dictyostelium* is a unicellular amoeba, largely eliminating complications from cell-cell interactions, and it has very modest growth requirements (tissue culture of axenic strains). Genetically, *Dictyostelium* is haploid; its genes have only a few and small introns which simplifies the generation of new knockout strains, and a wide range of mutant cell lines is already available.

Amoeboid cells migrate towards attractive stimuli by adopting an elongated shape and orienting parallel to the direction of motion (chemotaxis). This process is controlled by a complex network of signaling biochemical pathways, which drive the continuous remodeling of the cytoskeleton of the cell and its adhesions to the extracellular matrix (ECM). Despite the complexity of these processes, the cell can be viewed as a mechanically interconnected system consisting of a dynamic cytoskeleton cross-linked with motor proteins and attached to a membrane, using its adhesion sites to the substrate to migrate efficiently. By doing so, the mechanical implementation of cell motility can be approximated as a simple cyclic succession of mechanical events called the *motility cycle*, consisting of: 1. protrusion of temporary projections (pseudopodia); 2. attachment to the substrate; 3. contraction of the cell body; 4. detachment and retraction of the back of the cell (Figure 1.1) (2, 32-34). Furthermore, it has been shown that for both leukocytes and *Dictyostelium discoideum* these pseudopodia are successively extending and retracting. These successive extensions and retractions lead to periodic oscillations of the shape morphology of the cells, their velocity and the traction stresses they exert through their adhesions to the substrate (37-44).

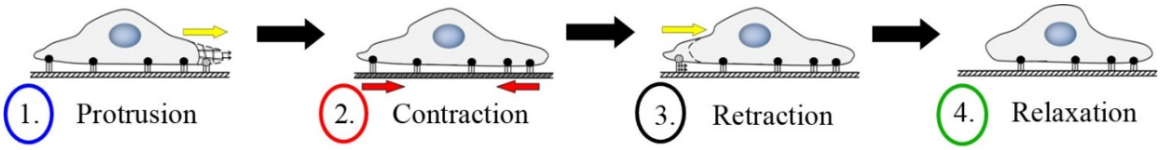

Figure 1.1: Different phases comprising the motility cycle followed by amoeboid cells during chemotaxis. 1. Protrusion: actin polymerization at the cell's front, where new attachments are formed with the substrate. 2. Contraction: increase in the contractile forces exerted on the substrate. 3. Retraction: the cell releases attachments at the back and retracts it by myosin-mediated actin filament contraction. 4. Relaxation: phase before a new motility cycle begins.

### 1.1.6 Key cytoskeletal components involved in cell migration

It is widely accepted that actin assembly (polymerization) generates a major part of the force required for cell movement. Globular actin can polymerize to form polarized actin filaments (F-actin) (45). Together with a multitude of actin interacting proteins, these filaments form the dynamic skeleton of the cell (cytoskeleton) and play an important role in the protrusion of the leading edge and the formation of the pseudopod. Translocation of the leading edge is driven by the formation of actin-based structures at the front of the cell such as filopodia (long parallel or bundled filaments leading to spikes), lamellipodia (branched filaments leading to sheet-like protrusions) or pseudopodia in the case of *Dictyostelium* (branched filaments leading to three-dimensional protrusions) (46). By regulated polymerization and depolymerization, actin filaments allow cells to change shape and contribute to the necessary force needed for cell movement. This dynamic regulation of the actin cytoskeleton is spatiotemporally coordinated by a myriad of actin binding proteins, actin nucleators as well as their upstream signaling regulators (47-49).

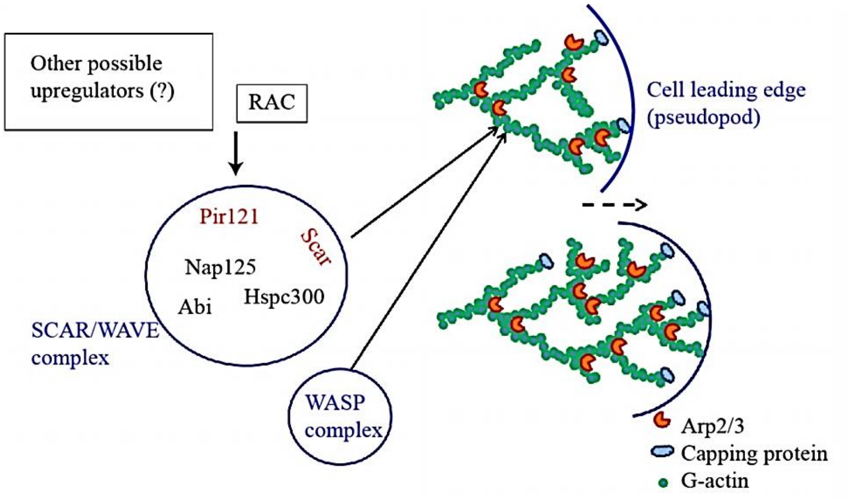

Figure 1.2: The mechanism of action of the Scar/Wave complex. Sketch showing how the activation of the Arp2/3 complex by the Scar/Wave complex leads to the dendritic polymerization of F-actin at the frontal cell edge and thus the pseudopod protrusion. Notice that the Scar/Wave is a pentameric complex that is activated by the Rac-GTPase and other possible signals and through its SCAR component directly interacts with the Arp2/3. The Arp2/3 in turn acts as a catalyst for F-actin polymerization, promoting the growth of the F-actin filaments in a Y-shaped (dendritic) mode. As the dendritic network of F-actin grows at the leading edge of the cell, the pseudopod is eventually pushed forward.

New actin polymerization occurs by either extending existing filaments in a linear fashion or by lateral branching at a roughly 70° angle. Forward extension of a lamellipodium (or pseudopodium in the case of *Dictyostelium)* containing a meshwork of branched filaments occurs by the growth of actin filaments adjacent to the plasma membrane, where branching is initiated in a Y-shaped mode by a heptameric complex called Arp2/3 (Figure 1.2) (48-57). A 70° angle is created between an existing actin filament and a new filament, which Arp2/3 nucleates, forming a dendritically-architectured skeleton at the frontal edge which helps propel the edge of the cell forward. WASP and SCAR/WAVE complexes are nucleation-promoting factors that activate Arp2/3 (Figure 1.2) (50, 58-65). The highly conserved SCAR/WAVE pentameric complex includes PIR121 (Sra-1/CYFIP/GEX-2), SCAR (WAVE), HSPC300, ABI1, and NAP1 (Hem2/KETTE/GEX-3) which bind and activate Arp2/3, and also bind other signaling factors that activate the SCAR/WAVE complex (66-69). Thus, SCAR/WAVE proteins are essential, since they may determine where in the cell actin polymerization will occur.

Actin binding and crosslinking proteins are also essential since they crosslink actin filaments in different ways and contribute to the mechanical integrity of the cytoskeleton. Among them, ABP-120 has been proposed to cross-link actin filaments in nascent pseudopodia and to play a key role in cell motility since it is required for normal pseudopod extension (70-73). ABP-120 is incorporated into the actin cytoskeleton shortly after stimulation with cAMP at a time that correlates with the cross-linking of actin into the cytoskeleton and with the pseudopod extension (74). In vitro, ABP-120 has been shown to orthogonally cross-link actin filaments to form a rigid actin gel (70).

Another important actin cross-linker is the motor protein MyoII. MyoII is important due to its contractile activity that is essential to the retraction of the trailing edge of the cell. The MyoII complex contains two heavy chains, two regulatory light chains, and two essential light chains (75-77). MyoII's motor activity is regulated by phosphorylation of the regulatory light chain and requires the essential light chain (78). The MyoII complexes can assemble into antiparallel bundles with motor head groups at both ends. These bipolar filaments bind and crosslink actin filaments to form a cortical meshwork that increases in density from the front to the back of the cell (79). This cytoskeletal structure is important for the mechanical stiffness of the cell (cortical tension) and can also generate the contractile forces required for efficient cell motility (80).

In addition to motors, translocation requires cell-substrate adhesions to transmit traction forces to the substrate (81). The mechanisms underlying cell-substrate adhesion and their role in the locomotion efficiency have been investigated in fibroblasts, keratocytes, and other eukaryotic cells, which attach to the substrate via discrete and localized focal adhesions (82, 83). Unlike fibroblasts, *Dictyostelium* and other amoeboid cells do not form localized focal adhesions, but rather attach to the substrate via more diffuse areas (38, 84, 85).

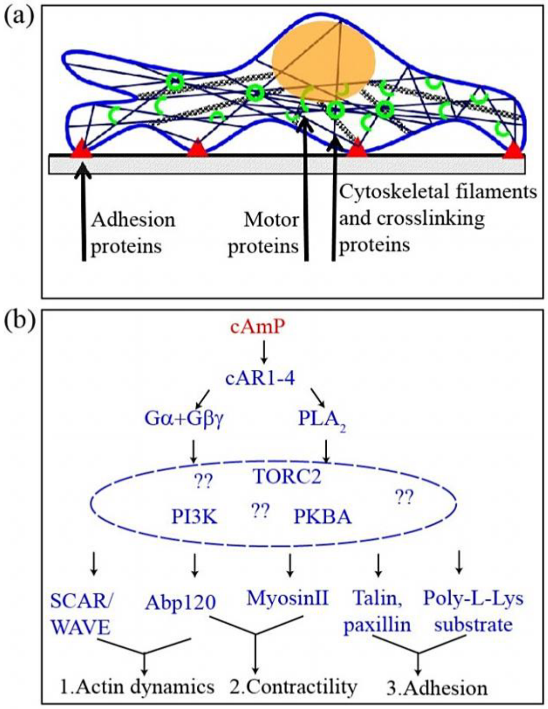

Figure 1.3: F-actin dynamics, motor proteins and adhesion are key components that drive cell migration. (a) Sketch of the cell depicting the key components comprising the dynamic cell's cytoskeleton, which are essential for cell migration. The blue contour represents the cell's surface, the orange circle the nucleus of the cell and the gray rectangle under the cell, the substrate. Notice the cytoskeletal filaments (blue and white-black lines), the F-actin crosslinking proteins (green arches), the adhesion proteins (red triangles) and the motor proteins (hollow green circles). (b) Diagram showing how the presence of cAmP eventually elicits a sequence of signaling events that lead to directional motility (chemotaxis). On the bottom of the diagram, key proteins of the cytoskeleton are shown as well as which aspect of motility their presence controls.

The composition and structure of these adhesions is less well understood in molecular terms. More importantly, the high speed of these cells means that they undergo much quicker assembly and disassembly of adhesions, which renders them challenging to study. For both of these two classes of motile cells, little is known about how key biochemical processes coordinate the formation and breakage of adhesions with the generation of traction stresses to control movement.

### 1.1.7 Aims of this dissertation

The present dissertation intends to elucidate how the regulation of F-actin polymerization by SCAR/WAVE, the proper F-actin crosslinking, and the adhesion of the cell to the substrate affect the production and dynamics of the traction stresses that drive cell movement. Traction Force Cytometry (TFC) has been used to measure the spatiotemporal distribution of the traction stresses exerted by wild-type cells and relevant mutant strains migrating up a chemoattractant gradient on flat elastic substrates (Figure 1.3). By jointly stacking these traction stress measurements in space and time, high-resolution kymographs that capture the key features of the adhesion and traction tension dynamics were also produced. The precise characterization of each traction stress and adhesion phenotype was then used to determine the role that SCAR/WAVE-mediated dendritic F-actin polymerization plays in the modulation of the cellular traction stresses and in the implementation of the motility cycle. In a similar manner by comparing wild-type cells with mutants with defective crosslinking, we elucidate the role of proper F-actin crosslinking in the mechanics of cell movement and highlight its importance for efficient cell migration. Finally, to gain more insight into the role of cell-substrate adhesion in cell migration we have analyzed cells migrating on substrates of varying stiffness and adhesivity, emphasizing as well the important role of the extracellular environment on cell migration.

## 1.2 Outline of dissertation

In Chapter 2, we present the experimental methodology used for the experiments carried out for this Dissertation. Using an exact solution of the elastostatic equation based on Fourier expansions that expresses the tractions explicitly as functions of the deformations, we calculate both the axial and lateral components of the traction stresses, and by jointly stacking these measurements in space and time, we produce traction tension kymographs that allow us to gain insight into the adhesion dynamics. Moreover, we present the methodology by which motility is divided in different motility modes with distinct contractility and adhesion dynamics based on the traction tension kymograph data. Finally, by studying and characterizing the periodicity of the cell length and strain energy time records, we categorize the various cell lines depending on whether they move quasi-periodically or not, and in the former case apply our cycle-splitting algorithm to gain further insight on the cyclic movement of the specific strains.

In Chapter 3, using the above-mentioned methodology, we study the dynamics of wild-type cell*s* moving up a chemoattractant gradient on an elastic substrate. We reconfirm that their migration is composed of a repetitive sequence of canonical steps where the cells adhere, on average, at two sites at their back and front halves and are in a contractile state constantly. Our analysis shows that the temporal evolution of the cell length, strain energy exerted on the substrate, and maximum F-actin florescence at the front of the cell present a quasi-periodic evolution. All the above three time records oscillate with the same frequency and are in phase while their frequency correlates with the mean migration velocity of the cells. Using the traction tension kymographs, we split motility into modes and find that wild-type cells move by switching mainly between two modes of distinct adhesion and contractility dynamics. Moreover, we find that changes in adhesion dynamics accompany contractility and migration speed changes.

In Chapter 4, similar to the wild type, we analyze two mutant strains that lack two key proteins of the SCAR/WAVE complex that regulates the dendritic F-actin architecture at leading cell edge (*scrA*$^-$ and *pirA*$^-$ cells). We find that the polarity and speed of the SCAR/WAVE mutants do not correlate with their F-actin levels. Moreover, disruption of the SCAR/WAVE complex causes the misregulation of the motility cycle. The strength of traction stresses differs in the SCAR/WAVE mutants and correlates with their altered F-actin levels while the spatial organization of the stresses and their F-actin localization remains similar to wild-type. Finally, using the traction tension kymographs, we show that *scrA*$^-$ move by employing one motility mode solely unlike the wild-type or *pirA*$^-$ cells.

In Chapter 5, we compare the mechanics of cell migration of wild-type cells with cells with defects in F-actin crosslinking (*abp120*$^-$ and *mhcA*$^-$). Our findings indicate that cells with cytoskeletal defects rely on lateral contractility in order to move, which emphasizes the key role of lateral contractility for cell migration. Unlike *mhcA*$^-$ cells, which constantly contract laterally using many adhesion sites located at the cell's periphery, *abp120*$^-$, which lack an effective pseudopod, move by establishing two adhesion areas and by periodically switching from a mode in which they contract axially to a mode in which they contract laterally.

In Chapter 6, we investigate the role of adhesion in amoeboid cell migration by altering the mechanical properties of the substrate on which cells migrate. We find that when wild-type cells chemotax on substrates of increasing stiffness, they increase the strength of their traction stresses but decrease their velocity while their shape becomes less polarized. Moreover, the area gain/loss of the cell due to deformation remains constant while the area gain/loss of the cell due to pure translocation reduces when moving on stiffer substrates. When wild-type cells migrate on substrates of increased adhesiveness, lateral contractility becomes essential while the motility modes utilized by the wild-type cells to move are completely different from those observed in regular substrates.

Finally, in Chapter 7, general conclusions are made and specific areas and subjects that would require further study are pinpointed and briefly discussed.

# Chapter 2
# Experimental Methods [†]

## 2. 1 Polyacrylamide Gel Fabrication

We prepared polyacrylamide gels of 5% acrylamide and 0.06% bis-acrylamide coated with 0.2 mg/ml collagen to use as substrates for our cells. We constructed the gels similar to those described elsewhere (86, 87). The gel consisted of two layers with the bottom layer containing no beads and the upper layer containing 4 μL of 2% carboxylate modified yellow latex beads of 0.1 μm diameter (Fluospheres, Molecular Probes, Eugene, Oregon). The thickness of the gels was ≈43 μm. The exact protocol we followed is described in detail below.

### 2.1.1 Upper and lower glass coverslips treatment

The first step of the procedure consisted of the treatment of the coverslips on which our gels would attach. Initially, 25 mm glass coverslips were placed on a hot plate and 500μL of 0.1 M NaOH were added so that they covered the entire surface of the coverslips. Once the liquid evaporated leaving a uniform, white thin film of NaOH on the surface to allow uniform gel attachment, the coverslips were removed from the plate and placed in a fume hood. The coverslips were covered with 100μL of 3-Aminopropyltriethoxysilane (APES) for 5 minutes and then rinsed thoroughly with distilled water. After verifying that the coverslips were dry, 100μL of a premixed solution of 0.5%

---

[†] Chapter 2 in part, has been published in the Conference Proceedings of the IEEE Engineering in Medicine and Biology Society. Distribution of traction forces associated with shape changes during amoeboid cell migration. Alonso-Latorre B., Meili R., Bastounis E., del Álamo J.C., Firtel R., Lasheras J.C.. In addition, the Traction Force Cytometry method presented has been published in the Proceedings of the National Academy of Sciences of the United States of America. Spatio-temporal analysis of eukaryotic cell motility by improved force cytometry. del Álamo J.C., Meili R., Alonso-Latorre B., Rodriguez-Rodriguez J., Aliseda A., Firtel R., and Lasheras J.C..

glutaraldehyde in PBS buffer was added to them and was let stand for 30 minutes up to 2 hours. The coverslips were then rinsed thoroughly and the excess liquid was aspirated. The dry coverslips were then ready for gel attachment.

### 2.1.2 Preparation of the two gel layers

The polyacrylamide gel consisted of two layers: the bottom one containing no beads and the upper one containing 4µL of 2% carboxylate modified yellow latex beads. The second step of this procedure consistsed of the preparation of these two layers. In order to make these two layers, two tubes were initially prepared. The tube with the beads contained: 25µL of 40% acrylamide, 4µL of 2.5% bis-acrylamide, 150µL of Na/K phosphate buffer and 4 µL of of a 2% carboxylate modified red latex beads with 0.1nm diameter (Fluospheres, Molecular Probes, Eugene, Oregon). The tube without beads is similar but contained no beads and 154µL of Na/K phosphate buffer. The solutions were mixed and placed on ice in vacuum for 15 minutes to reduce dissolved oxygen, which inhibits polymerization. 0.8µL of TEMED (crosslinker) and 1.2µL of 10% APS (catalyst) were added to the tube containing no beads and then 3.6µL of the mixture was placed at the center of circular glass coverslips which were positioned on top of the treated square ones to "sandwich" the polyacrylamide gel. Once the gel was polymerized (10-30 minutes later), the second layer containing the tracker beads was added in a similar manner and some weight was placed on the top coverslip to make the bead-containing layer slightly thinner. The square coverslips with the two layers on top of them were then mounted into Petri dishes filled with 50mM HEPES buffer (pH=8.5) using silicon grease (Dow Corning, Midland, Michigan).

### 2.1.3 Inspection of the gel under the microscope and activation with Sulfo-SANPAH

The last step involved the examination of the gels under the microscope to verify that the distribution of beads was uniform and the layer of beads was confined essentially in one focal plane (the uppermost) and the subsequent procedure for collagen attachment. For the second part, 200µL of

1mM Sulfo-SANPAH in HEPES buffer were added to the gel surface, which was then placed under 365nm UV light for approximately 10 minutes until the solution turns from bright red to brownish. After thoroughly washing the gel from the Sulfo-SANPAH, 0.2mg/ml collagen protein was added, and the gels were incubated with it overnight. The next day, the gel was rinsed, and then 4ml of HEPES buffer and 40 µL Ampicillin were added. The gel was stored in $4^{o}$C and could be used for one week.

### 2.1.4 Altering the substrate stiffness and adhesivity

To test the effect of increased substrate stiffness on cell migration, we constructed a stiffer substrate with increased bis-acrylamide concentration (from 0.06% to 0.15%) and kept the acrylamide concentration constant (5%). The expected stiffness of the resulting substrates was E= 5.6 kPa. To test the effect of increased cell adherence, 20 mg/ml of poly-L-Lys (MW=30000-70000, P9155 Sigma-Aldrich) were mixed together with the collagen solution, while the remaining protocol steps were the same as described above (88). Different concentrations of poly-L-lysine were tested, and the one selected was chosen since wild-type cells were still able to chemotax, but with deeply decreased speed.

## 2.2 Determination of the Elasticity of the Substrates

To verify that the published values of our gels' elasticity were the real ones, we performed sphere indentation experiments and also used AFM measurements. We used a tungsten carbide sphere (R=150µm, W=1.898µN, Hoover Precision, East Gramby, CT USA) which we carefully deposited on our substrate using a micro-aspirator. The microsphere caused an indentation on the elastic substrate. Dimitriadis et al. showed that the relation between Young's modulus of a gel slab of thickness h, an indentation depth of the sphere z, and a radius R and weight W, can be described by the following equation:

$$E = \frac{3W(1-\sigma^2)}{4R^{1/2}\delta z^{3/2}}\left[1 - \frac{2\alpha_o}{\pi}\Lambda + \frac{2{\alpha_o}^2}{\pi^2}\Lambda^2 + \frac{8}{\pi^3}\left({\alpha_o}^3 + \frac{2\pi^2}{15}b_o\right)\Lambda^3 + \frac{16\alpha_o}{\pi^4}\left({\alpha_o}^3 + \frac{3\pi^2}{5}b_o\right)\Lambda^4\right]^{-1} \quad (1),$$

where $\Lambda = \sqrt{R\delta z}/h$, the Poisson's ratio is assumed $\sigma=0.45$ and the coefficients $\alpha_o$ and $b_o$ are functions of $\sigma$:

$$\alpha_0 = -(1.2876 - 1.4678\sigma + 1.3472\sigma^2)/(1-\sigma),\ b_0 = -(0.6387 - 1.0277\sigma + 1.5164\sigma^2)/(1-\sigma) \quad (2).$$

Further details on the method can be found elsewhere (89). It should be noted that the above methodology is subjected to the need of small strains within the gel ($\frac{z}{h} \ll 1$). That is, gels of thickness ≈40μm can be indented up to 4μm in order to have a solution using the above equations. To solve that problem, we needed to change the material of the ball we were using, switching, for instance, to glass (density ~3000kg/m$^3$) or alternatively, to create thicker gels and assume that the elastic properties of the gels are conserved, which is what we did. We confirmed that our hypothesis was right by performing AFM measurements of the original thin gels. We then acquired a z-stack of images every $\delta z=0.4$μm. The indentation depth z was determined as the depth where the beads displaced by the sphere came into focus. The in-focus beads were detected using the SOBEL function in MATLAB. We also used AFM to measure the elasticity of the gels. Below Table 2.1 shows the expected elasticity predicted by Engler et al. (3rd column) (90), the one we measured using AFM (4th column) and the one we found using the indentation of a tungsten sphere (5th column) and its standard deviation (6th column) for both stiffness gels.

Table 2.1: Young's Modulus of the PA gels. Upper and lower rows show the two different stiffness gels constructed. The six columns show: acrylamide concentration (%); bis-acrylamide concentration (%); expected Young's modulus, $E_{REF}$ (kPa) from Engler et al (90); average value of AFM measured Young's modulus (average of N=5 gels for each case), $E_{AFM}$ (kPa); average value of calculated Young's modulus, $E_{IND}$ (kPa) by measuring the identation of a tungsten carbide sphere in the gel (average of N=12 gels and N=7 gels respectively). +/- values indicate standard deviation from the mean value. Notice that the calculated modulus using the indentation of a tungsten carbide sphere gives values similar to the measured modulus using the atomic force microscope (AFM).

| Acrylamide | Bis-acrylamide | $E_{REF}$ (kPa) | $E_{AFM}$ (kPa) | $E_{IND}$ (kPa) |
|---|---|---|---|---|
| 5% | 0.06% | 2 | 1.31+/-0.46 | 1.06+/-0.41 |
| 5% | 0.15% | 5.6 | 3.74+/-1.38 | 3.75+/-0.57 |

## 2.3 Actin-Myosin Assay

*Dictyostelium* cells were grown under axenic conditions in HL5 growth medium in tissue culture plates. Aggregation competent cells were prepared by starving them for 1 hour and then pulsing them for 5 hours by placing 10 ml of a 5 x $10^6$ cells/ml suspension in a starvation buffer (20 mM MES pH 6.8, 0.2 mM $CaCl_2$, 2 mM $MgSO_4$,) with cAMP to a concentration of 30 nM every 6 minutes. The cells were then pelleted, washed once in the starvation buffer, and then resuspended in 10 ml of starvation buffer to get rid of the cAMP and then incubated for 30 minutes with 2 mM caffeine at room temperature. Tubes were then prepared for time points 0”, 5”, 10”, 20”, 30”, 40”, 50”, 60”, 2’, 3’, and 4’, and 300 µl of 2x lysis buffer (20 mM TES pH 6.8, 1% Triton X-100, 2 mM $MgCl_2$, 5 mM EGTA, 10 µg/ml aprotinin, 10 µg/ml leupeptin) was added to each tube while they were kept on ice. An additional 30 µl of Na/K phosphate buffer was added to the 0” time point. A 270 µl cell sample was taken for the zero time point and added to the lysis buffer and 300 µl of cells stimulated with 1 µM cAMP were lysed for the other time points. The cell lysates were vortexed and incubated on ice for 10 minutes. After spinning at 15000 rpm for 10 min at 4° C, the supernatant was removed, and the pellet was washed once in 1X lysis buffer. After the washing step, the residual liquid was carefully removed and the pellet was resuspended in 20 µl 2x SDS sample buffer. The samples were then boiled for 5 minutes and 10 µl were loaded on an 8% polyacrylamide protein gel. Actin bands were approximately 45 kD. The gel was stained with Coomassie blue and the band intensities were quantified with Image-J. A rectangle encompassing the sample lane was drawn around each protein band and converted to an intensity graph for each lane from which the area of the peak corresponding to the actin band was determined.

## 2.4 Total DC Protein Assay

The *DC* (detergent compatible) protein assay (Bio-Rad Laboratories, Hercules, CA) is a colorimetric assay for protein concentration following detergent solubilization. The reaction is similar to the well-documented Lowry assay. A 10 µl sample of cell lysates prepared during the actin/myosin assay was mixed with the reagents provided by Biorad to a final volume of 0.94 ml according to the manufacturer's protocol. The absorbencies were read at 750 nm using a spectrophotometer. These measurements were used to normalize the F-actin content according to the relative total protein content of the initial lysates.

## 2.5 Cell Contour Identification

Differential interference contrast (DIC) images were acquired by using a 40X air lens at 4 s intervals when the cells where chemotaxing on polyacrylamide gel substrates. To identify the contours of the cells using the DIC images, MATLAB (Mathworks Inc, Natick, MA) was used to perform the digital processing of the image sequences. Since while recording the cells are moving on the polyacrylamide substrate, imperfections of the substrate can easily interfere with the outline identification of the cell. Consequently, it was necessary to use a custom algorithm to automatically determine the cell outline for each given cell. This procedure is comprised of five steps: First static imperfections from the original DIC image (Figure 2.1.a) were removed from the individual images by using the average of the image series as follows:

$$I_{inter}(x,y) = \frac{(I_{orig}(x,y) - I_{ave}(x,y))}{(I_{ave}(x,y) + \varepsilon)} \qquad (3)$$

where $I_{orig}(x,y)$, $I_{ave}(x,y)$, $I_{inter}(x,y)$ are the intensity fields of each raw image, the average image and the resulting intermediate image (Figure 2.1.b). The small parameter $\varepsilon$ is defined by the bit depth of $I_{orig}$

that was introduced to avoid division by zero; Second, the logarithm of the absolute value of the intensity field of the intermediate image $I_{inter}(x,y)$ was taken, and the resulting intensity field $I(x,y)$ was thresholded to extract its brightest features (Figure 2.1.c). The threshold was calculated using the histogram of intensities of the image resulting from the previous step, $H(I)$, and is given by:

$$I_{thr} = \frac{\int_{I_1}^{I_2} H(I)\cdot I\cdot dI}{\int_{I_1}^{I_2} H(I)\cdot dI} \qquad (4)$$

where $I_0$, $I_2$ are the intensities at which $H$ reaches its global maximum, and its next local maximum to the right of $I_0$ ($I_2>I_0$) respectively and $I_1$ is the intensity at which $H$ has maximal curvature in the interval $[I_0, I_2]$ (Figure 2.1.d). These calculations were performed on a polynomial fit to $H$ of an order high enough to represent the basic features of the distribution. Because $H$ is the slope of the cumulative distribution of intensities, the present choice of a threshold is in a region of high $H$ yet away from the global maximum of $H$ balances robustness and sensitivity. To ensure that the evolution of the threshold was smooth from frame to frame, the threshold at each frame was chosen as the average of the most recent ten thresholds. Third, the features obtained after the application of the threshold were refined using a process of image dilation and erosion with a structuring element of small size, $S_0$ ($S_0$=4-6 pixels~0.7-1 μm) (Figure 2.1.e). This procedure coalesces the nearby image features detected in the previous step (Figure 2.1.f). Fourth, a second image dilation and erosion was applied having a second structuring element $S_1$, whose size was determined empirically by comparing the resulting cell contours with manually traced contours on a number of cases (typically 1 every 50 frames). This comparison yielded the semi-empirical expression:

$$S_1(pixels) = 80\cdot\frac{A_{cell}}{A_{features}} - (80 - S_0(pixels)) \qquad (5)$$

where $A_{cell}$ is the average area of the cell contours of the previous three images, and $A_{features}$ is the area of the features obtained after the initial dilation and erosion in step 3, so that the ratio $A_{cell}/A_{features}$ is typically larger than 1. This step is based on the percolation theory, a mathematical theory that studies the behavior of connected clusters in a random graph that has applications in different areas of science. The main difference between our case and the aforementioned theory is that, the latter deals with large or infinite networks, whereas our network is highly reduced since it is composed of just a few features obtained after step 3. For this reason the determination of the structuring element size to be used is semi-empirical. Finally, the centroid coordinates $(x_c,y_c)$ and principal axes of each cell were calculated (major and minor second moments of inertia). The front and back were determined as the two parts in which the cell is divided by its minor axis of inertia, with the front pointing towards the direction of motion. Given that $\alpha$ is the angle between the x axis and the cell's major axis, the front is defined as:

$$[(x - x_c) cos a + (y - y_c) sin a][(dx_c/dt) cos a + (dy_c/dt) sin a] > 0 \qquad (6).$$

(a) Original DIC Image (b) Removal of Static Imperfections (c) Intensity field logarithm

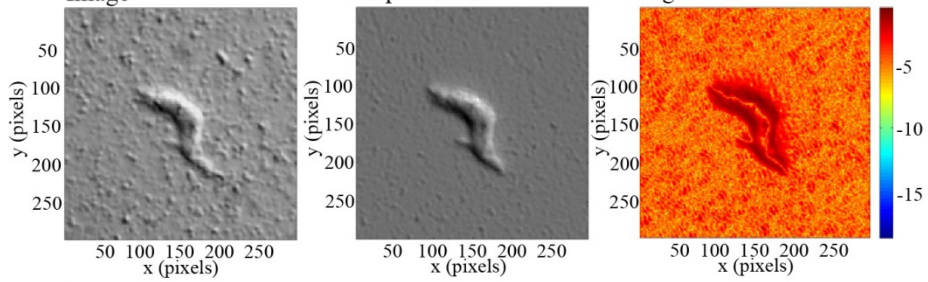

(d) Threshold determination (e) Threshold application (f) First dilation/erosion (g) Second dilation/erosion

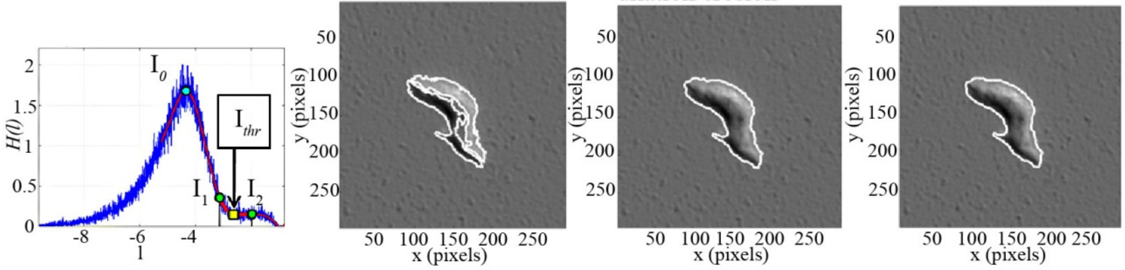

Figure 2.1: Cell shape segmentation. (a) Raw instantaneous DIC image of a *WT* cell. (b) Image resulting after removing static imperfections of DIC image in panel (a). (c) $I(x, y)$, natural logarithm of the absolute value of the image in panel (b). (d) Probability density function (PDF) of $I(x, y)$ (blue line); $H(I)$, polynomial fit to that PDF (red line); $I_0$, location of the global maximum of $H(I)$ (cyan dot); $I_1$ and $I_2$ (green dots) define the region of $H(I)$ whose centroid provides the instantaneous threshold $I_{thr}$ for the detection of the cell shape (yellow square). (e) Features detected (white contours) after application to image in panel (c) of threshold $I_{thr}$. (f) Cell shape (white contour) resulting from application of dilation/filling/erosion with structuring element of size $S_0$ = 6 pixels to features in panel (e). (g) Detected cell shape (white contour) after application of dilation/filling/erosion with structuring element of size $S_1$ to features in panel (f). Scale-bar in panel (a) represents 10 nm and ≈ 60 pixels. Background image in panels (e-g) is the same as in panel (b).

To retrieve the 3D shape of the cell time-lapse, fluorescent confocal images were acquired using a 40 X air lens at 12 s intervals. For each time point, *z*-stacks along the cell height were also acquired having a *z*-interval of 1 µm (typically 15 images). In this specific case, the 3D reconstruction (rendering) of the cell was performed using IMARIS.

## 2.6 Determination of the Substrate Deformation, Calculation of the Traction Stresses, and Construction of the Traction Tension Kymograph

### 2.6.1 Determination of the substrate deformation

The deformation of the substrate was determined from the displacements of fiduciary fluorescent beads embedded in the substrate which were measured using image correlation techniques similar to Particle Image Velocimetry (PIV), a technique commonly used for fluid flow visualization (91, 92) (Figure 2.2.e). To do so, we modified an already existing, open-source Matlab toolbox for PIV analysis named Urapiv, so that it suited the needs of this specific application and could be used to obtain the horizontal displacements of the beads (Figure 2.2.f). Square windows of 16 pixels with an overlap of 50% were used to perform the correlation. In each experimental session, the beads were imaged at the plane where their fluorescence intensity was maximal in order to minimize any systematic errors caused by out-of-focus beads (29).

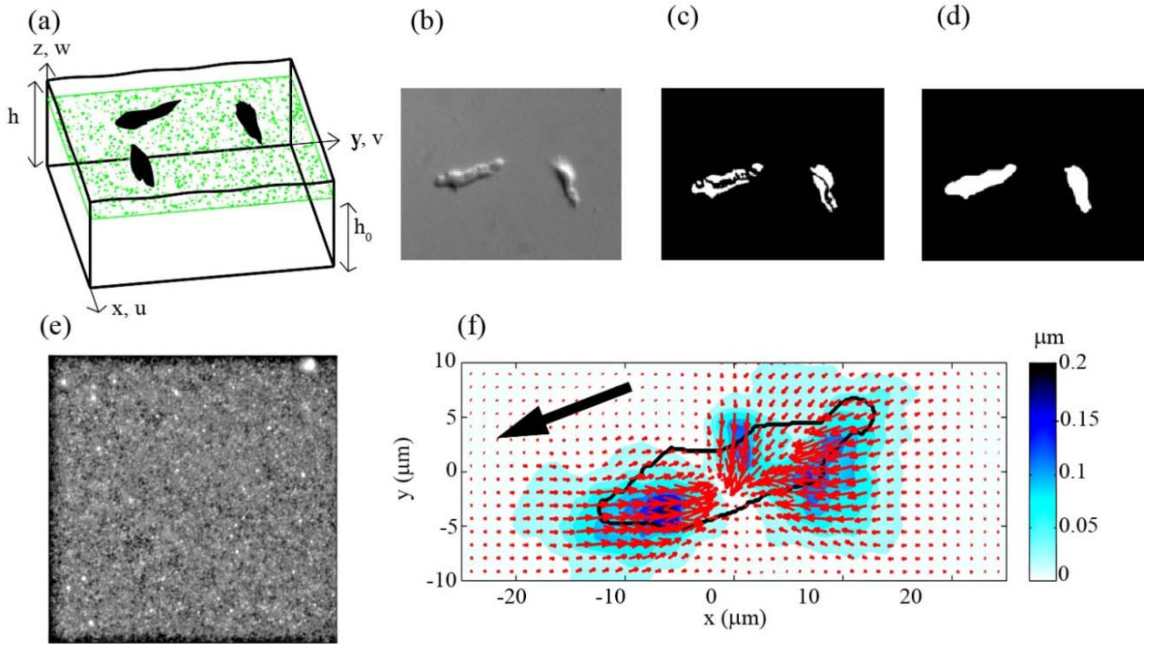

Figure 2.2: Sketch showing the methodology followed to calculate the displacement field induced on the substrate on which amoeboid cells crawl. (a) Setup of the experiment. The black irregular shapes represent the cells and the green fluorescent dots the beads embedded on the upper substrate portion. The black box represents the plate that contains the substrate on which the cells migrate. $h_0$ is the height from the bottom of the substrate to the plane where the intensity of the fluorescent beads is maximum and at which we acquire the image of the beads. h is the height from the bottom of the substrate to the plane at which we acquire the DIC image of the cells. (b) DIC image of the cells. (c) Binary image of the cells after automatically determining the threshold of the image. (d) Binary image after application of dilations/erosion using a certain circular morphological structuring element (strel). (e) Fluorescent image of the beads. (f) Calculated displacement field. The black line shows the cell's contour, the red arrows the direction and magnitude of the displacements of the beads and the color-map the amplitude of the displacements.

### 2.6.2 Calculation of the traction stresses

The traction stress field $\boldsymbol{\tau} = (\boldsymbol{\tau}_{zx}, \boldsymbol{\tau}_{zy})_{z=h}$ applied by a cell on its substrate surface was calculated by solving the elasticity equation of equilibrium for a linear, homogeneous, isotropic, 3D body of finite thickness *h.* For the calculations high-resolution Fourier Traction Force Cytometry techniques (FTFC) were used, developed by del Álamo et al (29), which consist of solving the elastostatic equation in the Fourier space, as originally proposed by Butler et al (28) taking into account the finite thickness of the substrate. Thus the method used is based on an explicit calculation of the adhesion force field in Fourier space, which takes into account the finite thickness of the elastic substrate, thus improving the accuracy and resolution of previous methods (89). The Young's modulus E of the substrate was 1.2 kPa (93), and the Poisson's ratio σ was assumed ≈0.45, as reported in previous studies (94, 95).

We assumed that the cell was moving on a free surface of finite known thickness $h$ of a linearly elastic substrate (Figure 2.2.a). The distance between the focal plane of the beads' maximal intensity where we calculated the displacement field $\mathbf{u}= (u, v, w)$ and the free surface is $h\text{-}h_o$ (in our PA substrates the beads seem to be confined to a layer just where the cells move so that $h_0 \approx h$). Because the densities of the cells and the surrounding buffer were similar and the contractile fibers of the cytoskeleton tend to predominantly orient horizontally, we also assumed that $\boldsymbol{\tau}_{zz}(z=h) \approx 0$. Thus the equations governing the displacement field for a linear, homogeneous, isotropic, 3D body of finite thickness are:

$$\frac{\nabla(\nabla\cdot\boldsymbol{u})}{(1-2\sigma)} + \Delta\boldsymbol{u} = 0 \qquad (7)$$

The boundary conditions are no slip at the bottom of the substrate, $\boldsymbol{u}_{\boldsymbol{z=0}} = (u, v, w)_{z=0} = 0$, and the measured lateral displacements $u_{h0}$ and $v_{h0}$ at the average vertical position of the beads, at $z = h_0 = h$. We assume periodicity in the horizontal directions and that $\boldsymbol{\tau}_{\boldsymbol{zz}}(z = h) = 0$. In order to find the analytical solution of the equation, we expressed the displacements in Fourier series such that:

$$\boldsymbol{u}(x, y, z) = \sum_{\alpha=-\infty}^{\infty} \sum_{\beta=-\infty}^{\infty} \widehat{\boldsymbol{u}}_{\boldsymbol{\alpha},\boldsymbol{\beta}} \exp(i\alpha x) \exp(i\beta y) \ (8)$$

where $\alpha$, $\beta$ were the wavenumbers for the x, y directions and $\widehat{\boldsymbol{u}}_{\boldsymbol{\alpha},\boldsymbol{\beta}}$ were the complex Fourier coefficients of $\boldsymbol{u}$. We expressed the traction stresses in a similar manner and thus solved analytically the elastostatic equations using Fourier series. The details of the method can be found elsewhere (29, 89). Using this force cytometry method both the forces exerted on the front and back halves of the cell can be calculated ($\boldsymbol{F}_f$ and $\boldsymbol{F}_b$) and the strain energy ($U_s$) imparted by the cell to the substrate can be calculated.

### 2.6.3 Construction of the traction tension kymograph

Once the cell contour was determined from the differential interference contrast (DIC) images, we identified the location of the major and minor second moments of inertia and the orientation of their axes.

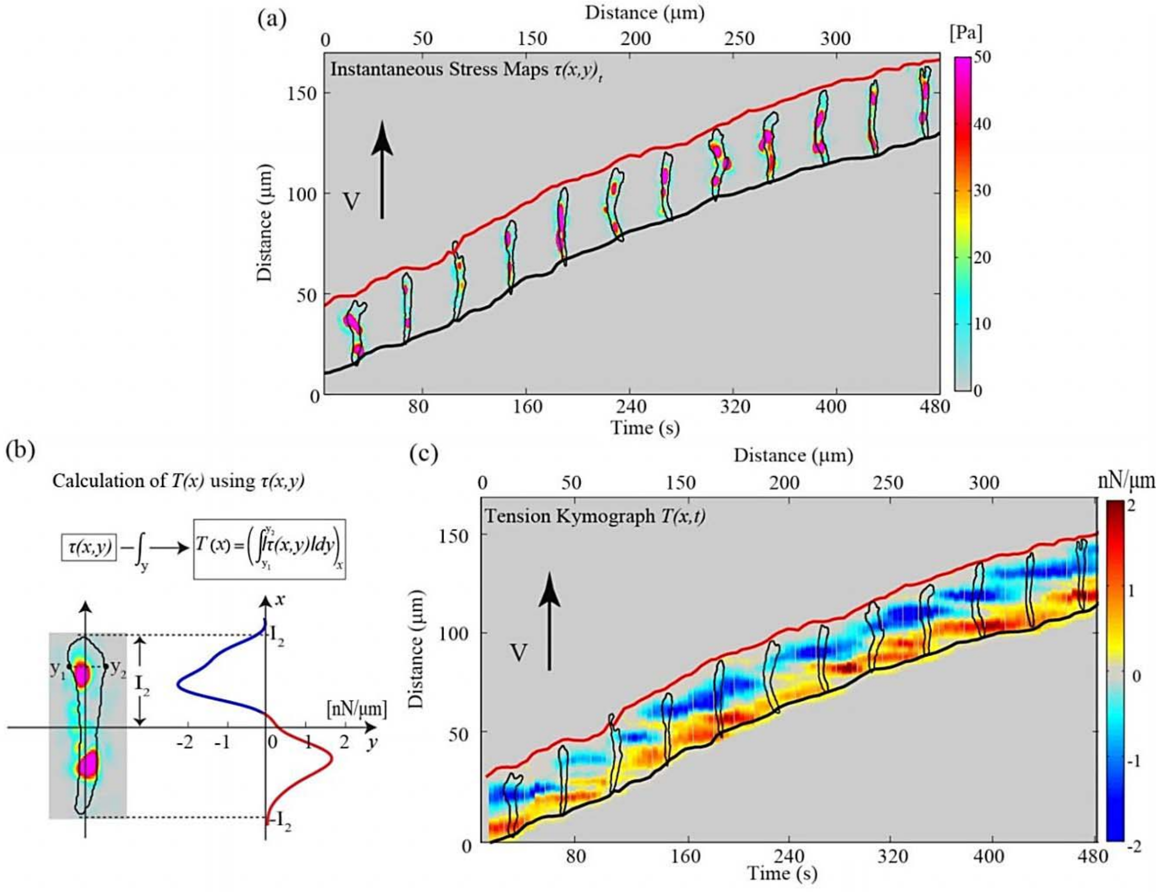

Figure 2.3: Traction stress and tension kymographs quantify the dynamics of amoeboid cell motility with high spatio-temporal resolution. (a) Spatio-temporal map of a cell's instantaneous magnitude of stresses *τ(x,y)*, taken every 40 s. The cell's major moment of inertia has been aligned with the y-axis, so that the cell is moving from bottom to top with the centroid velocity *V(t)*. The black contour superimposed onto the stress maps shows the instantaneous cell outline. Red and black lines indicate the front and back cell edge positions respectively. The color contours depict the magnitude of the total traction stresses (axial and lateral) in [Pa]. (b) Calculation of the traction tension *T* as a function of the position along the cell's length, *x*. (c) Tension *kymograph* showing the spatio-temporal dynamics of the traction tension, *T(x,t),* as a function of the position along the cell length, *x*, and time, *t*, for the cell shown in panel a. The black contours and red and black lines are the same as in (A). The color map represents the magnitude of *T(x,t)* in [nN/μm]. Red (blue) patches represent positive (negative) values of *T* corresponding to tensions pointing towards (away from) the direction of cell motion.

The traction stress field $\boldsymbol{\tau}(x,y)$ was then calculated and rotated to make the cell's major axis parallel to the vertical direction at each instant of time, as shown in Figure 2.3.a. In this coordinate system, we calculated the axial tension (traction force per unit length) at each instant of time by integrating the x-component of the traction stresses across the cell width (minor axis, y-direction), as shown in Figure 2.3.b:

$$T(x,t) = \int_{y1}^{y2} \boldsymbol{\tau_{xz}}(x,y,t)dy \qquad (9).$$

The tension kymograph was then constructed by stacking different temporal measurements and plotting *T(x,t)* in two dimensions with *t* in the horizontal axis and *x* in the vertical axis (Figure 2.3.c). This representation allows for a detailed quantitative analysis of the coupled evolution of shape changes and traction stresses during migration with very high temporal resolution.

In order to investigate how directed contractility contributes to the cell motility, we decomposed the traction force vector exerted by the cell on the substrate into its axial and lateral components $\boldsymbol{F_x}$ and $\boldsymbol{F_y}$. We define the axial and lateral contractility $\boldsymbol{F_x}$ and $\boldsymbol{F_y}$ as:

$$F_x = \frac{|\boldsymbol{F_f}|+|\boldsymbol{F_b}|}{2} \text{ and } \boldsymbol{F_y} = \frac{|\boldsymbol{F_r}|+|\boldsymbol{F_l}|}{2} \qquad (10),$$

where $\boldsymbol{F_f}$ and $\boldsymbol{F_b}$ are the average values of the axial traction forces exerted by the cell in its frontal and back halves, while $\boldsymbol{F_r}$ and $\boldsymbol{F_l}$ are the average values of the lateral traction stresses that the cell exerts at its right and left halves:

$$\boldsymbol{F_f} = \iint_{x>0} \boldsymbol{\tau_{xz}}(x,y)dxdy \text{ and } \boldsymbol{F_b} = \iint_{x<0} \boldsymbol{\tau_{xz}}(x,y)dxdy \qquad (11),$$

$$\boldsymbol{F_r} = \iint_{y>0} \boldsymbol{\tau_{yz}}(x,y)dxdy \text{ and } \boldsymbol{F_l} = \iint_{y<0} \boldsymbol{\tau_{yz}}(x,y)dxdy \qquad (12).$$

Note that $F_f = -F_b$ and $F_r = -F_l$ as the inertia of the cell is negligible. We calculate at each instant of time the strain energy $U_s$ (mechanical work) that the cells exert on their substrate as described elsewhere (29). Further details of the calculation of the traction stresses were provided previously (29, 89).

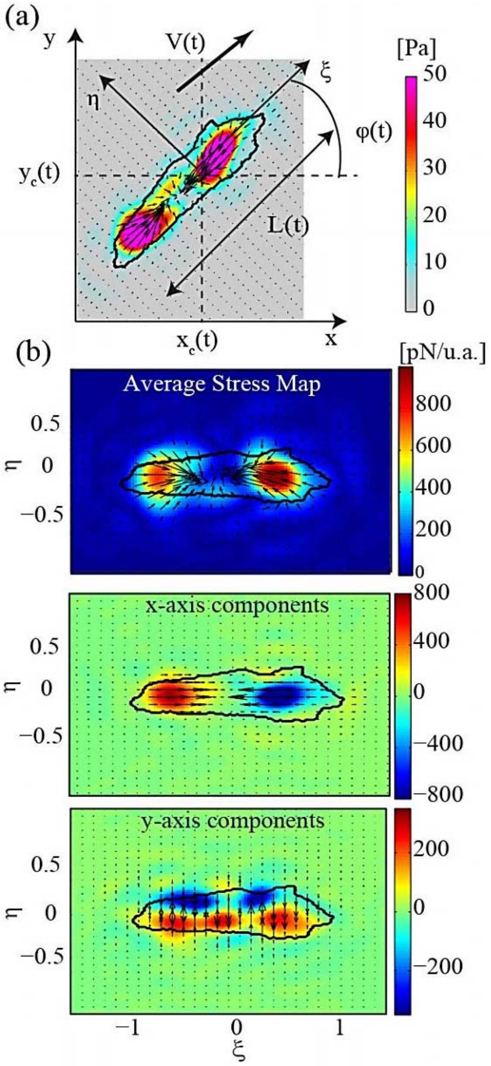

Figure 2.4: Traction stresses in the cell based coordinate system. (a) Representation of the cell-based reference system in which both traction stresses and shape of the cell are expressed. The black contour indicates the instantaneous contour of the cell, of length *L(t)*. The laboratory reference frame is indicated by axes (*x,y*). The axes of the cell-based reference frame (ξ, η) are centered at the instantaneous centroid of the cell ($x_c(t)$, $y_c(t)$) and are aligned with its major and minor axes, which lie at an angle *φ(t)* with respect to (*x,y*). The color-map and arrows indicate respectively the strength [Pa], and the direction of the total traction stresses exerted by the cell on the substrate. The thick black arrow indicates the direction of motion of the cell, moving with velocity *V(t)*. (b) The upper map shows the instantaneous traction stress field of a cell, measured in a reference frame rotated to coincide with the instantaneous principal axes of the cell and scaled with its half-length, *L(t)*/2 (cell based). The colors indicate the magnitude of the stresses in [pN/unit area] and the arrows indicate their direction. The black contour is the outline of the cell. The front of the cell corresponds to ξ> 0 and the back corresponds to ξ < 0. Middle and lower maps show the components of the axial and lateral traction stresses, which are parallel and perpendicular to the major axis of the cell respectively. In these two latter cases the color-maps indicate the magnitude and direction of the axial and lateral stresses respectively. The red color indicates positive value, in the direction of the positive ξ and η axis, and the blue color indicates negative value, in the opposite direction.

In order to perform proper statistical analysis and to compute average stress maps, we also converted the instantaneous stress maps into a "cell-based, dimensionless coordinate system" $(\xi,\eta)$ as defined in del Álamo et al (29), where $\xi=x/a$ and $\eta=y/a$ are the axial and lateral coordinates made dimensionless with the half length of the instantaneous major moment of inertia of the cell $a$ (29). In the "cell-based coordinate system" the axis of the major moment of inertia of the cell is always aligned with the positive horizontal axis $(\xi)$, and the origin is located at the instantaneous centroid of each cell. This coordinate system allowed us to compile statistics of the distribution of stresses and shapes at different instants of time coming from a large number of cells (Figure 2.4.a). We calculate at each instant of time the strain energy $U_s$ (mechanical work) that the cells exert on their substrate as:

$$U_S = \frac{1}{2}\int_A \boldsymbol{\tau}(x,y) \cdot \boldsymbol{u}(x,y)dxdy \quad (13),$$

where $\boldsymbol{u}$ is the measured displacement vector field at each point on the surface of the substrate and $\boldsymbol{\tau}(x,y)$ the corresponding stresses at each location. Additional details of the calculation of the traction stresses are provided elsewhere (29, 96).

## 2.7 Classifying of Motility in Different Modes

To dissect motility into different modes, we used the information provided by the tension kymographs. First, we located for each time point the maxima of the tension $T(x,t)$ at the front (negative stresses) and at the back (positive stresses) of the cell by calculating the fourth moment of inertia. The resulting time records were smoothed by convolving them with a triangular smoothing kernel. We then found the time derivative of the two smoothed time records by calculating their centered second order finite difference. The aforementioned time derivatives represent the velocity of the location of maximum tension at the front and back of the cell and their magnitude shows how stationary the adhesion sites are or conversely how much the adhesion sites are gliding, while their peaks show the number of adhesion sites formed as the cell migrates (Figure 2.5).

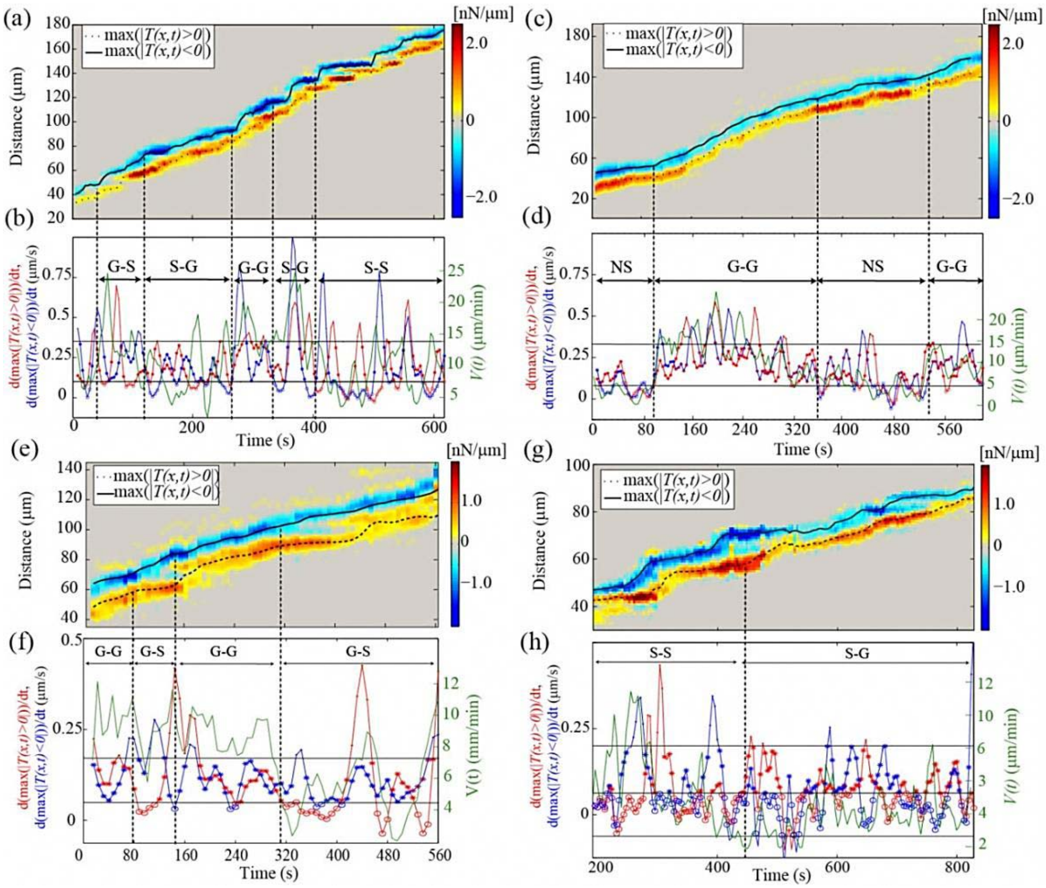

Figure 2.5: Identification of the motility modes. (a) Same tension kymograph as in Figure 3.2.a. Black solid (dotted) lines track the spatio-temporal evolution of the peak value of the negative (front) (positive (back)) traction tension, *T(x,t)*. The two lines are smoothed in time using a triangular 5-point kernel. (b) Criterion for the identification of the motility modes based on the speed of adhesion regions. Blue and red solid lines show the speed of the adhesion regions, defined as the slope of the solid and dotted lines in panel A. The green line shows the velocity of the cell centroid, obtained after smoothing its trajectory with the same kernel used for the adhesion regions. Black solid lines indicate the first and third quartiles of the distribution of the adhesion speeds. Speed points that are lower than the first quartile are marked with a hollow circle, while those between the first and third quartiles are marked with an asterisk. Speed points above the third quartile were observed only when new adhesions were created or existing adhesions were broken. These points are not considered for mode sorting, together with their two previous and posterior data points. Four different modes can arise from this classification; 1) S-S or stepping-stepping, when both frontal and rear adhesion sites are stationary. 2) S-G or stepping–gliding, when the frontal adhesion is stationary but the rear adhesion is moving forward. 3) G-S or gliding-stepping, when the frontal adhesion site is moving but the rear one is stationary. 4) G-G or gliding-gliding, when both adhesion sites are moving forward. (c) Same as panel (a) for a wild-type cell migrating on poly-L-lysine coated substrate. (d) Same as panel (a) referring to the tension kymograph of panel (c). Notice that the velocity of migration oscillates in phase with the speeds of the front and back adhesions (R>0.6, *p*=0.000). Thus, when the adhesion sites are stationary the velocity of migration is minimal and the cell is in a nearly stationary (NS) mode. (e) Same as panel (a) for a *mhcA*$^{-}$ cell chemotaxing on regular collagen-coated substrate. (f) Same as panel (b) referring to the tension kymograph of panel (a). (g) Same as panel (a) for an *abp120*$^{-}$ cell chemotaxing on regular collagen-coated substrate. (h) Same as panel (b) referring to the tension kymograph of panel (g).

We calculated the cumulative histogram of the distribution of the adhesion velocities for the front and back of the cell and located where the 25th and 75th percentiles lie. We assumed that all values lower than the 25th percentile suggest stationary adhesion sites, while values between the 25th and 75th percentiles, suggest gliding adhesion sites. Finally, values higher than 75th percentile were not taken into account since they coincide with peaks of the two time records due to creation of either front or back adhesion sites (Figure 2.5.b, d). In cases where the correlation coefficient between the instantaneous velocity of migration *V(t)* and the two time derivatives was higher than 0.4, we considered that the cell is quasi-stationary.

## 2.8 Determination of the Location of the Actin Foci and the Local Maxima of Instantaneous Stresses

We used a custom Matlab function (localMaximum.m) to detect the local maxima of stresses (traction adhesion sites) of the instantaneous stress maps. The aforementioned function receives three input parameters: the matrix containing the data, the minimum distance between peaks, and a flag that allows for the exclusion of equal points. After locating the local maxima, we calculated the integral of stresses of circles centered on the maxima with a radius equal to 1/10 the length of the cell. The magnitude of those vector integrals are a good estimation of the force strength of the specific traction adhesion sites while their direction indicates towards where the cell is contracting.

We used the same function to locate the maxima of *Lifeact* (marker for F-acitn) fluorescence intensity at the ventral side of the cells (actin foci). Actin foci are very dynamic and transient structures that remain static with respect to the substrate during cell migration and are thought to be indicative of adhesion sites (38). They have a lifetime that varies between 15 to 25 s. During their lifetime, the actin foci appear to be stationary, consistent with the adhesion sites remaining on average stationary while cells move. The velocity seems to be inversely proportional to the number of actin foci (we found a similar relationship for the strain energy within a cell). An interesting question is does the number of actin foci correlate with the strength of the stresses? To address that question, we calculated the number of foci that lie within a traction adhesion circle and correlated the number of foci with the magnitude of the integral of the stresses within the specific circle. We also constructed traction tension kymographs and superimposed the actin foci (bright dots at the ventral side of the cell shown as hollow circles) on them at each instant of time depending on their axial position. Data points coming from the spatio-temporal evolution of one single actin spot were automatically connected by lines, while the appearance of each new spot was highlighted by a bold circle.

## 2.9 Determination of the Periodicity of the Cell Length and Strain Energy Time Records

We applied wave analysis to test if the measured time records of the cell length and strain energy were periodic (i.e. narrow-band spectrum) and to calculate their dominant period (Figure 2.6.a). First, we obtained an initial estimate of the main period, $T_0$, of these records from the peaks in their autocorrelation functions (Figure 2.6.b). Second, we determined the period of the cycle $T$ by fitting the time records to a sinusoidal function of the form $f(t) = a \cdot \sin(\frac{2\pi t}{T} + \varphi)$ in a nonlinear, least squares sense. The signal frequency was estimated as: $f = 1/T$. Since secular fluctuations can shift the detected periods to spurious, long values not related to the changes in cell length associated with the motility cycle, the period $T$ was constrained using the initial estimate between $T_0/2$ and $2T_0$. We observed consistently that the best fit resulted from a sine function of a frequency similar to the one determined initially through the autocorrelation function. The value of the coefficient $a$ was independently set equal to the absolute maximum of the normalized time record, and its value did not affect the estimation of $T$. The value of the coefficient $\varphi$ was not constrained.

After determining the best fitted sine waves forthe time records of the cell length during motility, we cross-correlated them to determine their degree of periodicity. Thus, we were able to quantify the extent to which a sine wave of period $T$ can capture the behavior of the particular cell length time record. We computed the Spearman's correlation coefficients $R_{L\_sine}$ and the p-values $p_m$ for Spearman's $R_{L\_sine}$ to test the hypothesis of no correlation. We also defined the parameter degree of periodicity as: $DOP = R_{L\_sine} \cdot 100$, so that $0<DOP<100$.

We applied a similar analysis in order to find the degree of correlation between the time records of the cell length and strain energy. We computed the Spearman's correlation coefficients $R_{L\_U}$ to assess how well cross-correlated the cell length and strain energy time records were and the p-values $p_m$ for Spearman's $R_{L\_U}$ to test the hypothesis of no correlation between the time records. We also calculated the time delay between the two time records by locating the maximum of their cross-correlation function.

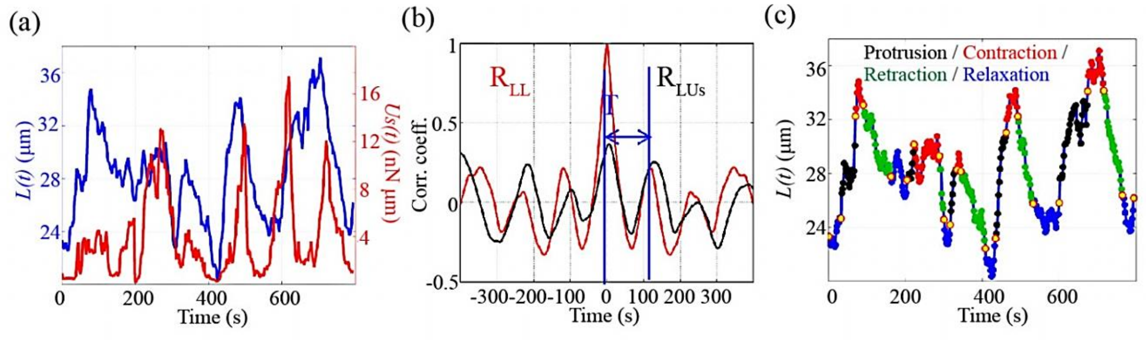

Figure 2.6: Splitting the motility cycle followed by the cells into four distinct phases. (a) Time evolution of the cell length, $L(t)$ (blue), and of the elastic energy $U_s(t)$ (red), of a representative wild-type cell. Notice that both time records oscillate periodically with the same frequency and are in phase. (b) Autocorrelation function of the time records of the cell length, $R_{L\_L}$ (red), and of the strain energy, $R_{L\_Us}$ (black). The distance between the peaks of $R_{L\_L}$ and $R_{L\_Us}$ is equal to the period $T$ of the motility cycle of the given cell. In this particular example $T$ is ~100 s. (c) Splitting of the motility cycle into the four phases based on the oscillations of the cell length (blue) using our semi-automatic algorithm, based on conditional statistics of the cell length. Time points corresponding to protrusion, contraction, retraction and relaxation are shown with black, red, green and blue dots respectively.

To optimally locate the peak of the correlation function, we applied parabolic-fitting interpolation to the vicinity of the peak point of the cross-correlation function, as described elsewhere (97). We followed a similar technique for the cell lines expressing *Lifeact* to analyze the correlation between the time records of the maximum *Lifeact* fluorescence intensity at the cell's front and the cell length.

## 2.10 Phase Statistical Analysis of the Motility Cycle

For those cell lines for which we identified the existence of a motility cycle, we obtained the spatiotemporal organization of cell shape and traction stresses during each stage of the motility cycle by using a phase-averaging technique previously developed in our lab (29, 31). This algorithm uses the time evolution of the cell length or strain energy as a criterion for splitting the motility cycle into four different phases: 1, protrusion, identified as the time during which $L$ and $U_s$ are increasing; 2, contraction, time during which $L$ and $U_s$ are near a local maximum; 3, retraction; time during which $L$ and $U_s$ are decreasing; 4, relaxation time during which $L$ and $U_s$ are near a local minimum (Figure 2.6.c).

Chapter 2 in part, has been published in the Conference Proceedings of the IEEE Engineering in Medicine and Biology Society. Distribution of traction forces associated with shape changes during amoeboid cell migration. Alonso-Latorre B., Meili R., Bastounis E., del Álamo J.C., Firtel R., Lasheras J.C.. In addition the Traction Force Cytometry method presented has been published in the Proceedings of the National Academy of Sciences of the United States of America. Spatio-temporal analysis of eukaryotic cell motility by improved force cytometry. del Álamo J.C., Meili R., Alonso-Latorre B., Rodriguez-Rodriguez J., Aliseda A., Firtel R., and Lasheras J.C..

# Chapter 3

# *Dictyostelium* Cells Regulate Their Migration Speed by Alternating Between Two Motility Modes [†]

Chemotaxing cells integrate the complex signaling networks that regulate their directional migration into a repetitive sequence of shape changes that involve protrusion of the frontal pseudopodia and retraction of the back of the cell (1, 33, 38, 98). The time variation of these shape changes and the mechanical work exerted by the cells on the substrate have a broad frequency spectrum, but both signals exhibit a well-defined periodicity (Figure 2.6) (25, 29, 38). These periodic fluctuations of the cell's shape and traction stresses are coordinated into four broadly defined phases: protrusion of the cell's front, contraction of the cell's body, retraction of its rear, and relaxation (Figure 1.1) (29, 30, 99). Essential to the implementation of these phases are: a) the dynamics of the actin cytoskeleton and its associated crosslinking proteins, b) the regulation of the actin-myosin contraction, and c) the dynamics of assembly and disassembly of substrate adhesions (Figure 1.3) (31).

In amoeboid-type locomotion, the directional dendritic polymerization of F-actin at the front creates a pseudopod and is important for propelling the edge of the cell forward (100). As the pseudopod advances, new substrate adhesions are created which, upon maturation, allow the cell to generate traction forces via actin-myosin contraction. Although it has long been established that these contractile forces are essential to propelling the cell's body forward (31), the precise mechanism

---

[†] Chapter 3 is being prepared in part for publication. Chemotaxing amoeboid cells migrate by switching between distinct modes of adhesion dynamics and contractility. Bastounis E., Meili R., Alvarez-Gonzalez B., del Álamo J.C., Lasheras J.C., Firtel R.

connecting the spatiotemporal coordination of the traction forces implemented by the cell to control its migration speed is still unknown.

Wild-type cells crawling up a chemoattractant gradient adjust their migration speed in response to environmental factors such as changes in the substrate stiffness and/or the substrate adhesiveness (94, 101, 102). Even when cells move on substrates of uniform chemical and mechanical properties, they do not migrate at a constant speed, often switching between periods of fast and slow speeds (103, 104). The dynamics of assembly and disassembly of adhesions to the substratum directly affect the cell migration speed (88, 105). Presently, little is known about the mechanisms by which the adhesion dynamics are coordinated with the traction stresses during migration and the key biochemical processes involved. The mechanisms underlying cell-substrate adhesion and their role in the locomotion speed have been investigated in fibroblasts, keratocytes, and other eukaryotic cells, which attach to the substrate, forming discretely localized focal adhesions (82, 83). However, it has been more challenging to examine how the adhesions dynamics control the cell's migration speed in fast moving cells such as *Dictyostelium*, with their much quicker assembly and disassembly adhesions turnover. Furthermore, unlike fibroblasts, *Dictyostelium* cells do not form localized focal adhesions, but rather attach to the substrate on larger areas (38, 84, 106).

In this chapter, we aim at investigating the coordinated dynamics of substrate adhesions and traction stresses generation by which wild-type *Dictyostelium* cells control and adjust their migration speed. We use high-resolution Fourier Traction Force Cytometry (FTFC), to simultaneously measure the spatiotemporal distribution of traction stress and shape changes of wild-type cells migrating up a chemoattractant gradient. Employing kymographs of adhesion and force dynamics, we demonstrate that *Dictyostelium* cells migrate by switching between two motility modes each of which has distinct adhesion dynamics and axial and lateral contractility.

## 3.1 Quantitative Evidence of a Force Regulated Motility Cycle

It has previously been shown that amoeboid cells move by following a series of well-defined steps that result from periodic oscillations of the cell length, *L(t)* (30, 40) and of the strain energy, $U_s(t)$ deposited on the substrate (30, 31, 37, 38, 107) (Figure 2.6). To determine a measure of the degree of periodicity of wild type chemotactic migration, we first examined and compared the temporal evolution of cell length, *L(t)*, and strain energy, $U_s(t)$ for individual wild-type cells. To that end, we calculated the autocorrelation of *L(t)* and $U_s(t)$ signals as well as their cross-correlation to determine the periodic content of each signal, and the correlation between signals as described previously (Figures 2.6, Chapter 2.10).

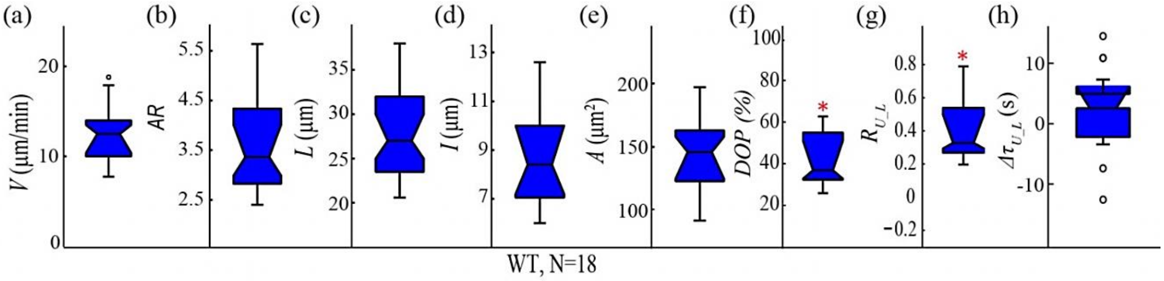

Figure 3.1: Boxplots of kinematic parameters of chemotaxing wild-type cells (N = 14). (a) Speed of migration, *V* (μm/min). (b) Aspect ratio, *AR* (cell length divided by cell width). (c) Cell length, *L* (μm). (d) Cell width, *I* (μm). (e) Area, *A* ($\mu m^2$). (f) *DOP* of the time evolution of the cell length *L(t)*. (g) Correlation coefficients, $R_{L\_U}$, between the time evolution of the strain energy, $U_s(t)$, and the cell length, *L(t)*. (h) Boxplots of the time delay between the cell length and the strain energy ($\Delta\tau_{U\_L}$), where the cell length serves as the reference function. Open circles represent outliers and the notched section of the boxplots shows the 95% confidence interval around the median. The red asterisks indicate a distribution with a median significantly different from zero: *, $p_z < 0.05$ (Wilcoxon signed rank test).

We determined the main frequency component of the motility cycle for each cell line using the autocorrelation function of both *L(t)* and $U_s(t)$. A harmonic sinusoidal signal oscillating with that specific frequency was then fitted to the data in a non-linear least squares sense (Figure 2.6, see Materials and Methods). We found that the distributions of the correlation coefficient between $L(t)$ and $U_s(t)$, respectively, with the best fitting, harmonic sinusoidal signal were positive and significantly different from zero, while the average *p*-values obtained suggested significant correlations (quality of fit) (Figure 3.1.f). This finding proves quantitatively that both the cell length and strain energy (mechanical work) oscillate periodically. The above method can be further used to compare the periodicity of migration of wild type versus mutants.

Consistent with previous findings (29, 31), the correlation coefficients between $L(t)$ and $U_s(t)$ for wild type were significantly greater than zero based on p-value tests, suggesting that the cell length, as represented by the length of the major moment of inertia of the cell, oscillates periodically and in-phase with the strain energy (Figure 3.1.g). We also observed an average 1.3 second time delay between the strain energy, $U_s(t)$ and the length, $L(t)$ for wild type, which appeared not to be significant (Figure 3.1.h). According to these results, cell lengthening and increase of force exertion on the substrate occur nearly simultaneously for wild-type cells (at least within the time resolution of our experiments).

We also reconfirmed that wild-type cells migrate with an average speed, $V$ linearly proportional to the frequency, $f$ of the oscillations in their cell length and strain energy (see Figure 4.5) (31). This suggests the relation $V = f \cdot \lambda = \lambda/T$, in which $\lambda$ is a constant equal to the average step length advanced by the cell per cycle. Interestingly, we found that $\lambda$ is always smaller than the length of the cell but we did not find any correlation between the size of the cell and the migration speed. The above findings suggest first that wild-type cells move as fast as they can repeat their motility cycle, and second, that during a motility cycle, the cells cannot take a step bigger than their own cell length.

## 3.2 Cells Migrate by Switching Between Distinct Motility Modes

While migrating up a chemoattractant gradient, wild-type cells move by periodic elongation and contraction as described in Figure 2.3 (29, 31, 98, 108). Integrating the axial traction stresses across the cell's width yields the contractile tension along the cell's major axis (Figure 2.3.b).

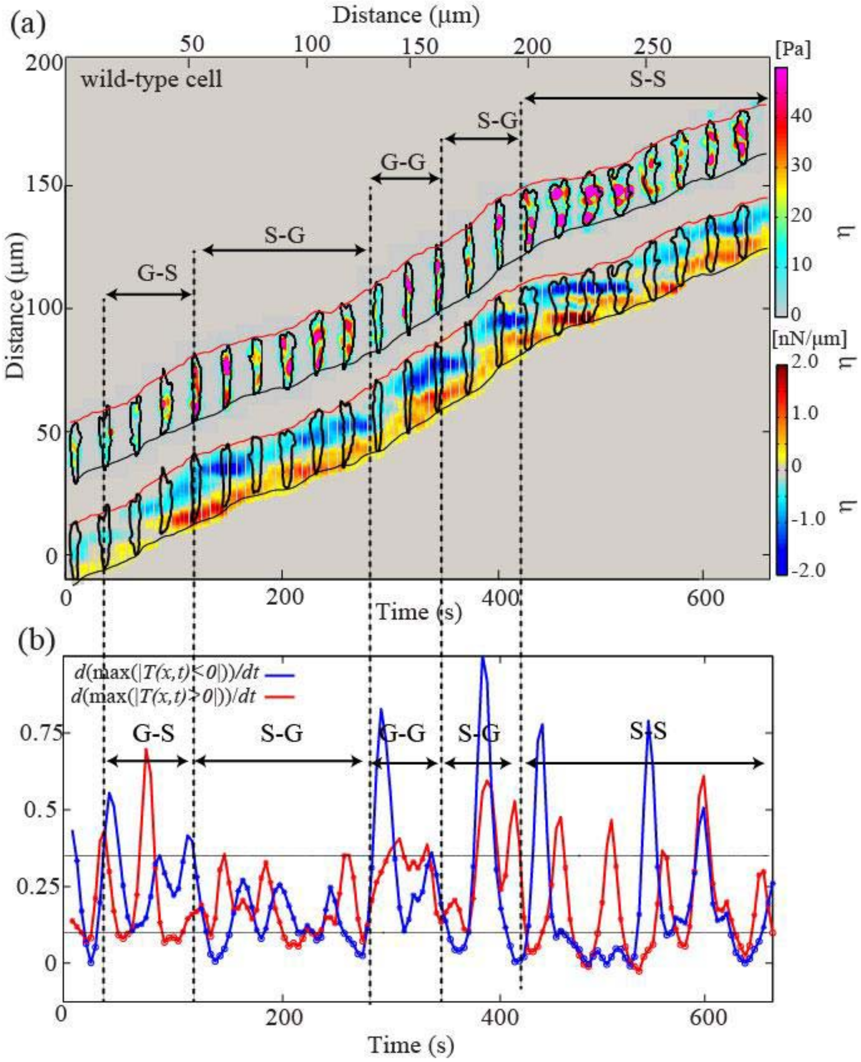

Figure 3.2: Spatio-temporal dynamics and motility modes in wild-type cells migrating on collagen-functionalized polyacrylamide substrata. (a) Kymographs of traction stresses $\tau(x,y)$ (upper part) and traction tension $T(x,t)$ (lower part) for a representative chemotaxing wild-type cell (for explanation see Figure 2.3). The instantaneous traction stresses and cell contours are shown every 28 s. Analysis of spatio-temporal patterns in the traction stresses and tension reveals different motility modes (for explanation see Figure 2.5). The modes are indicated as: S-S (stepping-stepping); S-G (stepping-gliding); G-S (gliding-stepping); G-G (gliding-gliding). The first and second letters correspond to the frontal and to the back adhesion respectively. (b) Identification of the distinct motility modes based on the front and back adhesion speeds. Blue (red) solid lines show the speed of the front (back) adhesion regions defined by $T(x,t)$. Black solid lines show where the first and third quartiles of the distribution of adhesion region speed (0.1 and 0.4 $\mu$m/s) (see Figure 2.5).

Jointly stacking these measurements in space and time produces high-resolution kymographs that capture the key features of the adhesion and traction tension dynamics. Thus, these tension kymographs allow for a detailed analysis of the various motility modes implemented by the cells as they migrate. (Experimental Procedures, Figure 2.3.c)

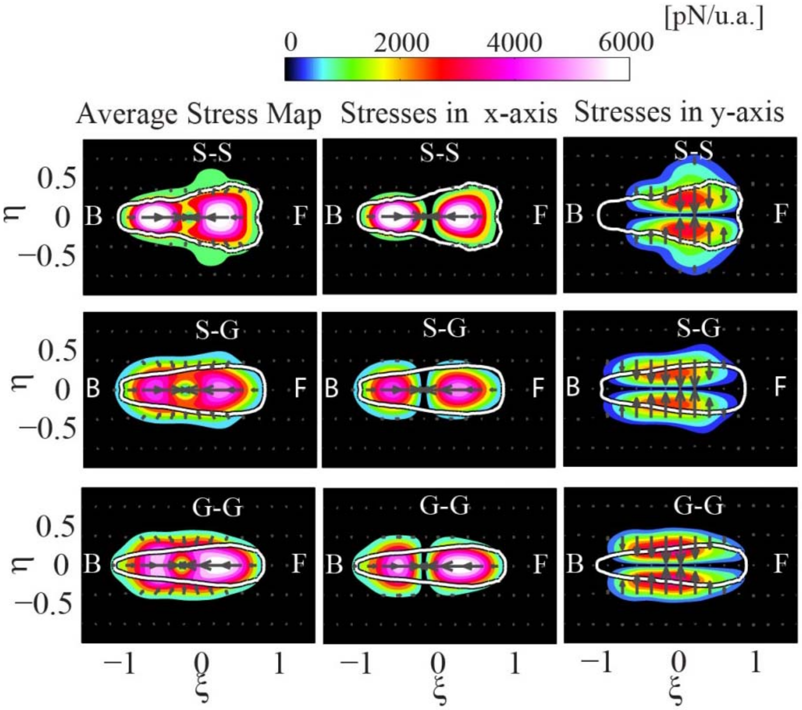

Figure 3.3: Average traction stress maps in the cell-based reference frame. The $\xi$ - and $\eta$ -axes coincide with the instantaneous principal cell axes and the origin is the cell centroid. Spatial coordinates are scaled with the instantaneous length of the major axis of each cell, *L(t)* (Figure 2.4). Left column shows the average stress maps during the S-S (upper), S-G (middle) and G-G (lower) motility modes. Details of how the cell-coordinate system used in these plots is constructed can be found elsewhere (29). The color maps indicate the magnitude of the total stresses in [pN/unit area], and the arrows indicate their direction. The white line contours show the average shape of the cells in this reference frame. The front (F) of the cell corresponds to $\xi > 0$ and the back (B) to $\xi < 0$. The second and third columns show the axial and lateral components of the traction stresses respectively.

Inspection of these kymographs reveals that wild-type cells continuously contract axially and most often form two diffuse adhesion regions located at the front and back halves of the cell. These axial tensions are represented in the tension kymograph by the blue (front-to-back direction) and red (back-to-front direction) patches (Figure 2.3.c). Based on the characteristics of the adhesion dynamics in these kymographs, we can distinguish four motility configurations or modes during the migration of wild-type cells. This classification provides insight into the role played by the forces during cell movement (Figure 2.3.c and Figure 3.2.a). The first mode is defined by the evolution of the red and blue patches parallel to the horizontal time axis, indicating that the adhesion sites where the cell applies traction stresses remain stationary while the cell protrudes a pseudopod (Figure 3.2.a and Figure 3.4.a). After the cell establishes a new adhesion under the nascent frontal pseudopod, the back

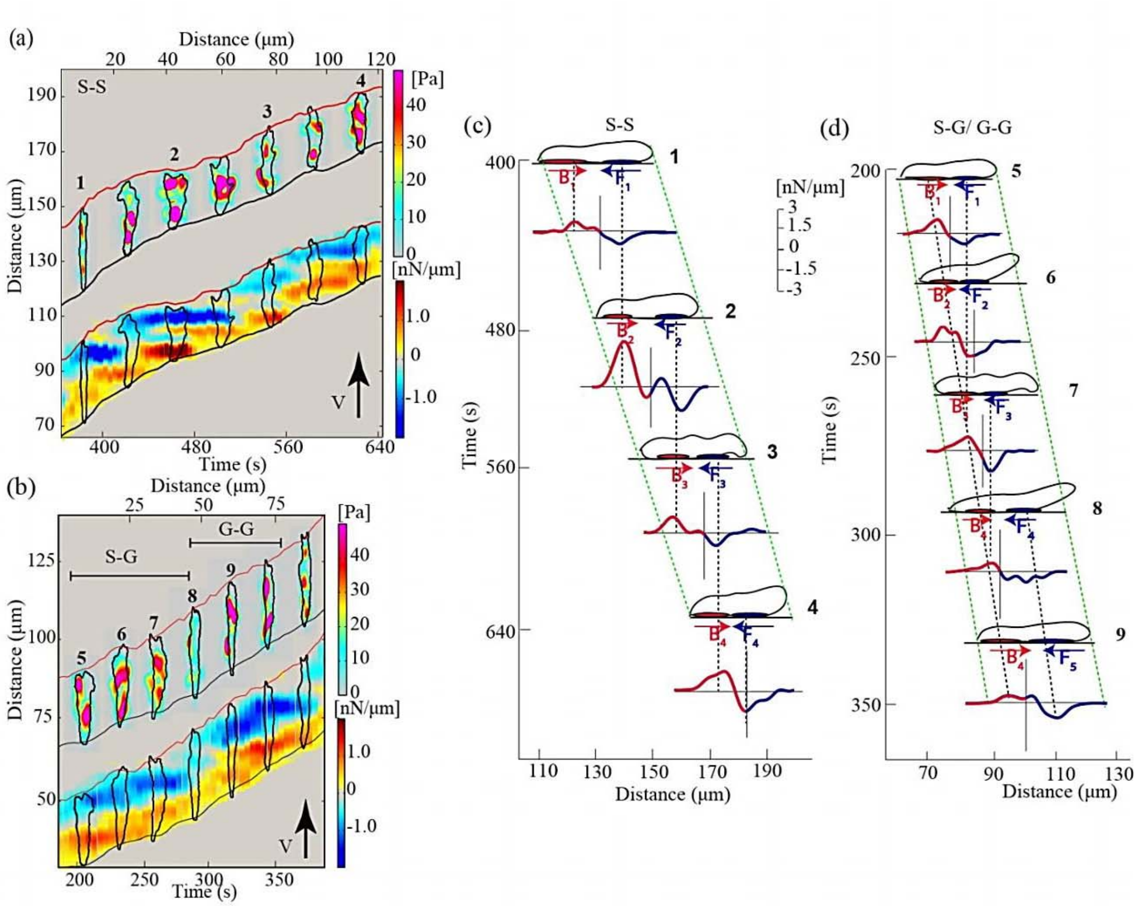

Figure 3.4: Characterization S-S and S-G/G-G motility modes in wild-type cells. (a) Kymographs of traction stresses *τ (x,y)* (upper part) and tension *T(x,t)* (lower part) for the representative wild-type cell of Figure 3.2.a during the S-S motility mode (for explanations see Figure 2.3). Notice that both frontal and back adhesions remain stationary. (b) Same as Figure 3.2.a, for the S-G/G-G motility modes. Notice that in the S-G mode the frontal adhesion remains stationary during the protrusion of the new pseudopod but the back adhesion glides forward. During the G-G mode both frontal and back adhesion sites are gliding forward. (c) Sketch depicting how the cell migrates during the S-S mode. The vertical axis indicates time and the horizontal axis indicates the cell location in the direction of the major axis of the cell. Four representative instants of time are displayed and labeled with the corresponding time frame numbers in panel (a). Black contours are cartoon representations of the cell's side view showing frontal and back adhesion sites with blue and red ovals underneath the cell. Blue and red arrows show the direction of the contractile axial forces at the front and back of the cell respectively. The experimental profiles of traction tension corresponding to each instant of time are plotted underneath its sketch. The insert between graphs C and D indicates the scale for tension values. (d) Sketch depicting how the cell migrates during the S-G (5-8) and G-G (8-9) motility modes, similar to panel (c).

adhesion breaks and the “old” front adhesion now becomes the “new” back adhesion (see the switching from blue to red occurring in the horizontal patches in Figure 3.4.a). This process is repeated periodically (motility cycle) and is illustrated in Figure 3.4.c which shows sketches of thecell’s shape and the measurements of the traction tension $T(x,t)$ during three motility cycles, with each lasting, on average, ~88 s (Figure 3.4.a, c). The sketches show that, as the cell translocates, the back adhesion $\mathbf{B_1}$ breaks when a new frontal adhesion $\mathbf{F_2}$ is formed. The previous stationary frontal adhesion $\mathbf{F_1}$ now becomes the new back adhesion $\mathbf{B_2}$. Subsequently, when a new pseudopod forms, a new frontal adhesion $\mathbf{F_3}$ is created and the back adhesion $\mathbf{B_2}$ breaks. This process can repeat itself in perpetuity. We named this mode *“Stepping-Stepping”* or *“*S-S*”,* since the cell steps through a series of stationary frontal and back adhesions, (Figure 3.4.c and Figure 3.5.c). During this periodic process, the cell always moves forward, with the average speed varying only slightly between cycles.

In the second most frequent mode, we observed that during the formation of new pseudopods, the blue anterior patches (and therefore adhesions) remain nearly stationary, while the red posterior patches are inclined at a constant angle, suggesting that the back adhesions glide forward at a constant speed (Figures 3.2.a and Figure 3.4.b, d). We named this second motility mode “*Stepping-Gliding*” mode (“S-G”) (Figure 3.4.b, d and Figure 3.5.b, d). The cyclic nature of this second mode is further illustrated in Figure 3.4.b, which shows the time evolution of the axial tension over 4 motility cycles. As was the case with the S-S mode, in the S-G mode, the cell is also in a constant axial contraction between the front and back adhesions **F** and **B** (Figure 3.4.b, d and Figure 3.5.b, d). When the cell protrudes a pseudopod forward, the front adhesion $\mathbf{F_1}$ remains stationary while the back adhesion $\mathbf{B_1}$ constantly glides forward. The stationary front adhesion $\mathbf{F_1}$ progressively weakens with time, and a new front adhesion $\mathbf{F_2}$ forms under the extending pseudopod, and this process then repeats itself. In addition, we found that when the temporal changes of the elastic energy are analyzed, the degree of periodicity (*DOP*) is lower in the S-G compared to the S-S mode (Table 3.1). The tension kymograph shown in Figure 3.4.b confirms this finding as it shows that the cell in the S-G mode exhibits periodicity in the formation of frontal adhesion but not in the back, which is continuously sliding forward (Figure 3.4.b, d).

Table 3.1: Summary of the average motility parameters for the S-S, S-G and G-G motility modes for the cell shown in panel (a). The parameters shown in the table include averages of speed of migration ($V$); aspect ratio ($AR$); length of the cell ($L$); strain energy ($U_s$); axial forces ($F_x$); lateral forces ($F_y$); mode time duration ($\Delta\tau$); mode-specific motility cycle period determined through the strain energy time record ($P_{mode}$); mode-specific motility cycle period normalized with the overall motility cycle period ($P_{mode}/P$); mode-specific degree of periodicity of the strain energy time record ($DOP_{Us}$).

| Mode | $V$(μm/min) | $AR$ | $L$(μm) | $U_s$(nNμm) | $F_x$ (nN) | $F_y$ (nN) | $\Delta\tau$ (s) | $P_{mode}$ (s) | $P_{mode}/P$ (s) | $DOP$(%) |
|---|---|---|---|---|---|---|---|---|---|---|
| S-S | 9.76 | 2.75 | 23.8 | 0.72 | 1.23 | 0.67 | 112 | 88 | 1.12 | 40 |
| S-G | 13.7 | 3.55 | 28.0 | 0.54 | 0.94 | 0.51 | 96 | 64 | 0.94 | 29 |
| G-G | 16.2 | 3.87 | 28.4 | 0.56 | 0.93 | 0.57 | 46 | --- | --- | --- |

We also observed a third mode where both the blue and red patches are inclined at a relatively constant angle. We termed this mode "*Gliding-Gliding*" or "G-G" implying that both the front and back adhesions of the cell are simultaneously gliding forward as the cell migrates (Figure 3.4.b, d). Finally, the fourth mode, which occurs rarely, takes place when the back adhesion is stationary (red patch at the back half of the cell that is horizontal) whereas the front adhesion is gliding at a nearly constant speed (blue patch at the front half of the cell that has an upward slope) (Figure 3.2.a). We named this fourth mode "*Gliding- Stepping*" ("G-S"), since the front adhesion is gliding while the back remains stationary.

## 3.3 Changes in the Adhesion Dynamics are Concomitant with Changes in Contractility Dynamics and Cellular Migration Speed

To analyze the tension kymographs of a large number of wild-type cells, we developed a technique to determine automatically when a cell was implementing each of the distinct modes described above (Figure 3.2.a-b and Figure 2.5, Experimental Procedures).

Although wild-type cells always exhibit periodic axial contractions while moving, we found that, in addition, they alternate mainly between the S-S and S-G modes, seldom employing the G-G and G-S modes (Figure 3.2.a and Figure 3.2). Since the *Gliding-Stepping* (G-S) mode was observed <5% of the time, it was not analyzed. further. We observed that the *Gliding-Gliding* (G-G) mode is short-lived and always appears between two S-G modes. Closer inspection of the stress maps of the entire cell revealed that the G-G mode usually appears due to two front adhesions in close proximity, and in the tension kymographs, resemble a single adhesion that is gliding. (Figure 3.2 and Figure 2.5.a-b).

We found that the period of the S-G mode cycle (64 s) is ~30% lower than that of the S-S mode (88 s), and the velocity of cell migration in the S-G mode is ~40% higher than that of the S-S mode (Figure 3.2.a and Table 3.1). During the S-G mode, the cell exerts weaker traction stresses compared to the S-S mode (Figure 3.2 and Table 3.1). The G-G mode appears to be associated with bouts of maximal migration (~65% higher than the average migration speed of the "S-S" mode) (Figure 3.4.b, d and Table 3.1). Inspection of the tension kymograph suggests that this mode may arise due to the increased frequency of front adhesion formation that results in an overlapping of multiple tension patches at the front (Figure 3.2.a and Figure 3.4.b). As seen in Table 3.1, the increase in the frequency of front adhesion formation in the G-G mode is associated with an increase of the velocity of migration, similar to our previous finding that the cell varies its speed by adjusting the period of the motility cycle (29). Figure 3.5 shows the traction stresses together with the three dimensional (3D) reconstruction of the cell body obtained using confocal microscopy for each motility mode. The cell is initially moving implementing the S-S mode where both front and back adhesion sites are stationary ($\Delta\tau$~300 s), and then, while maintaining its front adhesion stationary, it starts gliding its back adhesion forward, thus switching into the S-G mode ($\Delta\tau$~300 s). Notice the slight decrease in the magnitude of stresses when switching into the S-G mode as well as the increase in the cell's speed and aspect ratio.

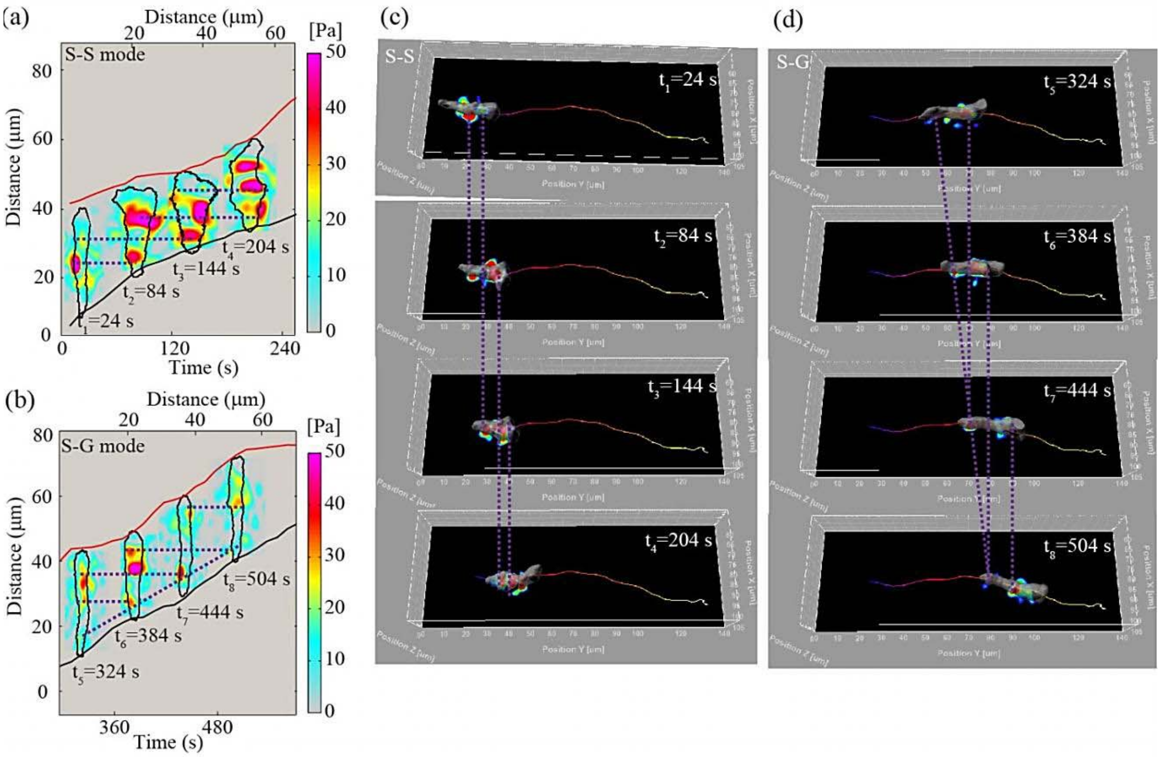

Figure 3.5: Three-Dimensional Characterization of S-S and S-G motility modes. (a, b) Maps of the instantaneous magnitude of the traction stresses *τ(x,y)* for a representative wild-type cell expressing *lifeact*-GFP (F-actin marker) during the S-S (panel a) and S-G (panel b) motility modes. (c) Time evolution of traction stresses and three-dimensional cell shape during the S-S motility mode (see corresponding stress fields in panel a). The purple lines correspond to the dashed horizontal lines in panel a. The specific experiments required simultaneous acquisition of the fluorescence image of the beads and of the entire *lifeact*-GFP expressing cell (*dz*=0.1μm). The 3D cell was rendered using IMARIS and the stresses calculated using MATLAB where imported as additional channel in IMARIS and can be viewed as an ortho-slice just below the semi-transparent cell. (d) Same as panel c for the S-G motility mode (see corresponding stress field in panel b). Notice that in both modes but particularly during the S-G mode the pseudopods tend to protrude initially upwards and then eventually adhere on the substrate.

## 3.4 Traction Strain Energy is Higher in the S-S Mode than in the S-G and G-G Modes

For a statistical description of the distinct motility modes, we analyzed their characteristics using wild-type cells that were tracked for a minimum of 500 s (N=8). For each specific mode, all motility parameters were normalized with their mean value for the whole migration period, so that averages of many cells could be compiled. The normalized averages of the migration speed $V$, aspect ratio $AR$, elastic energy $U_s$, and the axial and lateral contraction forces $\boldsymbol{F_x}$ and $\boldsymbol{F_y}$ for each mode and their durations $\Delta\tau$ are shown in Figure 3.6.

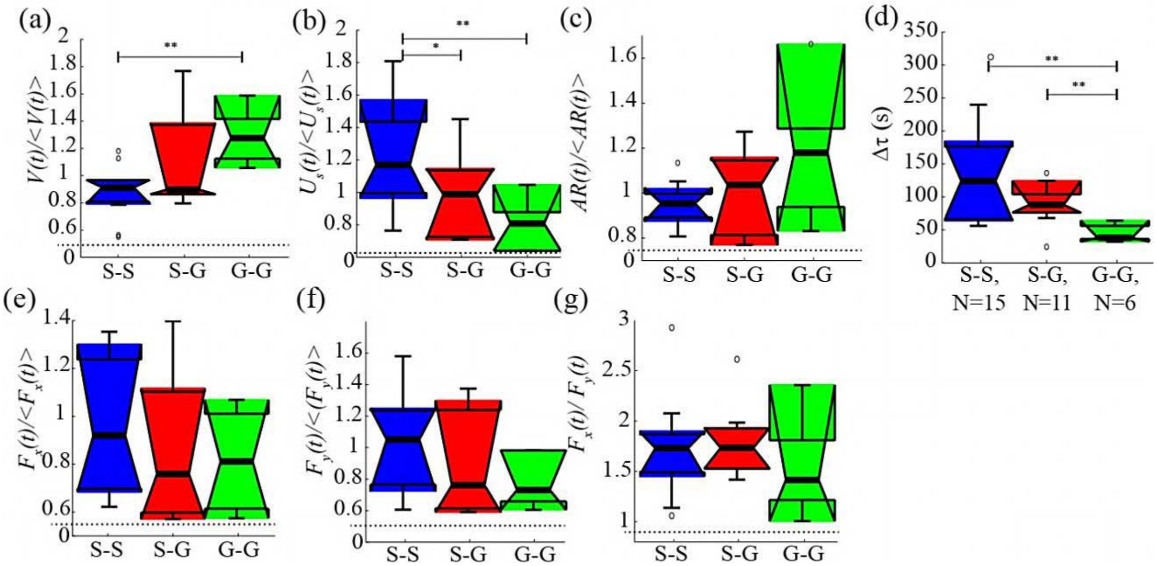

Figure 3.6: Statistical quantification of motility modes in wild-type cells. Boxplots of the motility parameters corresponding to the S-S (blue), S-G (red) and G-G (green) motility modes, for N=8 wild-type cells. Each motility parameter is normalized with the mean value of the specific parameter during the whole time the cell is migrating. (a) Speed of migration ($V$). (b) Strain Energy ($U_s$). (c) Aspect ratio ($AR$). (d) Mode duration ($\Delta\tau$). Below each boxplot the number of modes N identified is indicated. (e) Axial force ($F_x$). (f) Lateral force ($F_y$). (g) Ratio of axial to lateral forces. Circles represent outliers, and the notched section of the boxplots shows the 95% confidence interval around the median. One and two asterisks denote statistically significant differences between the median of two distributions (<0.05 and <0.01 respectively obtained by non-parametric wilcoxon rank sum test).

We found that cells move faster when they impart less mechanical energy on the substrate (Figure 3.6.a, b). The strain energy in the S-S mode is approximately twice that of the S-G or G-G modes, while the average speed is ~30% lower. We observed that the mean aspect ratio during the S-S mode is lower than that of the other two modes although the difference is not statistically significant (Figure 3.6.c and Table 3.2). We found that the average durations of the S-S and S-G modes are similar (Figure 3.6.d). When these modes are implemented, they last considerably longer than the G-G mode (Figure 3.6.d, h), further supporting our hypothesis that the G-G mode is just a hybrid form of the S-G mode as discussed above.

Table 3.2: Summary of average motility parameters for the S-S, S-G and G-G motility modes, for wild-type chemotaxing cells (N=8). The parameters shown include averages of speed of migration ($V$); aspect ratio ($AR$); cell length ($L$); strain energy ($U_s$); mode time duration ($\Delta\tau$); axial force ($F_x$); lateral force ($F_y$).

| Mode | $V$ (μm/min) | $AR$ | $L$ (μm) | $U_s$ (nNμm) | $\Delta\tau$ (s) | $F_x$ (nN) | $F_y$ (nN) |
|---|---|---|---|---|---|---|---|
| S-S | 9.40 | 3.03 | 25.7 | 0.64 | 133 | 0.95 | 0.51 |
| S-G | 11.1 | 3.28 | 27.7 | 0.39 | 97 | 0.70 | 0.41 |
| G-G | 14.6 | 3.81 | 31.2 | 0.37 | 36 | 0.67 | 0.40 |

To investigate whether the different modes also exhibit differences in the lateral contractility, we decomposed the traction stresses for all three modes into their axial and lateral components expressed in cell-based coordinates (Experimental Procedures). In all three modes, the axial contractility was ~50% greater than the lateral contractility (Figure 3.6.g, Table 3.1and Table 3.2). Importantly, we found that in wild-type cells, the axial and lateral stresses decrease proportionally (by ~30%) when the cell switches from the S-S to either the S-G or G-G modes (Figure 3.6.e-f, Table 3.1and Table 3.2).

## 3.5 Actin Foci Localization Corroborate the Existence of Motility Modes

In order that traction stresses be exerted, the areas on the ventral side of the cells where they are exerted, need to be in direct contact with the substrate. However, we cannot claim there the ventral areas of the cell are not adhering on the substrate, if there is no stress exertion on the substrate. Thus, while tractions stress exertion requires attachment of the cell to the substrate, a lack of traction stresses

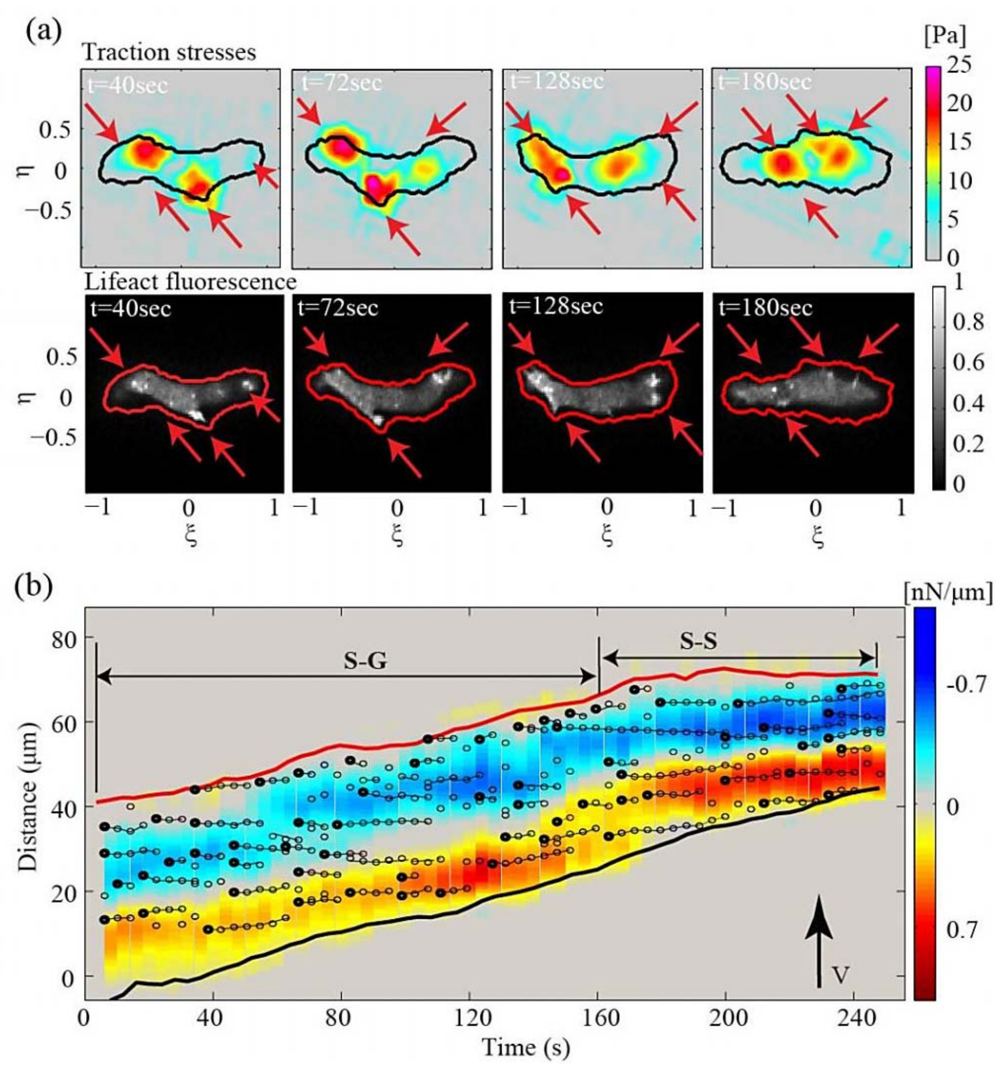

Figure 3.7: Regions of high traction stresses coincide with adhesion sites and traction tension kymographs track the spatio-temporal dynamics of the adhesion sites. (a) Snapshots of the traction stresses (top row) and of the basal *lifeact* fluorescence at the ventral side of a representative chemotaxing wild-type cell, in the cell based coordinate system. Black (top) and red (bottom) contours show the outline of the cell. Red arrows point at local stress maxima, which coincide with the location of spots of increased fluorescence. (b) Traction tension kymograph for the same cell. The local maxima of fluorescence have been tracked and superimposed on the kymograph (black circles). Data points coming from the spatio-temporal evolution of one single actin spot are connected by lines. The appearance of each new spot is highlighted by a bold circle. Adhesion sites at the front of the cell tend to be stationary. Rear adhesions tend to glide forward during the S-G mode and remain stationary during the S-S mode.

does not suffice for non-adhesion to the substrate. Consequently, in order to be able to assess the dynamics of the adhesion sites of the cells through the stress kymographs, we had to correlate the stress kymographs with kymographs of the localization of a fluorescent marker of some adhesion-specific molecule (Figure 3.7). Unfortunately, the receptors controlling the adhesion of free-living *Dictyostelium* cells to their substrate have not been yet identified unambiguously (84). To date, no *Dictyostelium* integrin homologue has been identified, but there are several proteins that are thought to be involved in adhesion, such as paxillin, talin and myosin VII (109). Nevertheless, under the microscope, wild-type cells expressing talin-GFP and myosin VII-GFP showed no localization at their ventral sides.

Yumura et al. proposed that on the ventral side of the *Dictyostelium* cells there are actin-containing structures which act as a "foot" and which they named actin foci (38). Simultaneous observations by internal reflection microscopy (IRM) and confocal fluorescence microscopy revealed that the ventral cell membrane is closest to the substratum at actin foci, and that although they are really transient structures, the actin foci remain spatially stationary during their short life (110). Furthermore, using purely qualitative evidence, they showed that actin foci loci co-localized with areas of traction stress exertion. These findings represent the first evidence that actin foci serve as the feet of *Dictyostelium* cells, and that adhesion sites during migration most probably remain stationary with respect to the substrate.

We reconfirmed that actin foci are very dynamic, transient structures that on average remain static with respect to the substrate during cell migration (Figure 3.8.b, c). They have a lifetime that varies between 15 to 25 s (Figure 3.8.c). During that time, they are stationary, consistent with the hypothesis of the adhesion sites remaining on average stationary while cells move (Figure 3.7.a-b). The velocity was found to be inversely proportional to the number of actin foci. An interesting question we tried to address was whether the number of actin foci correlates with the strength of the traction stresses. To answer that question, we located the instantaneous peaks of stresses, defined a circular area around them, and calculated the integral of stresses at these disks (Figure 3.8.d). We then calculated the number of foci that were found within those disks and compared this number to the

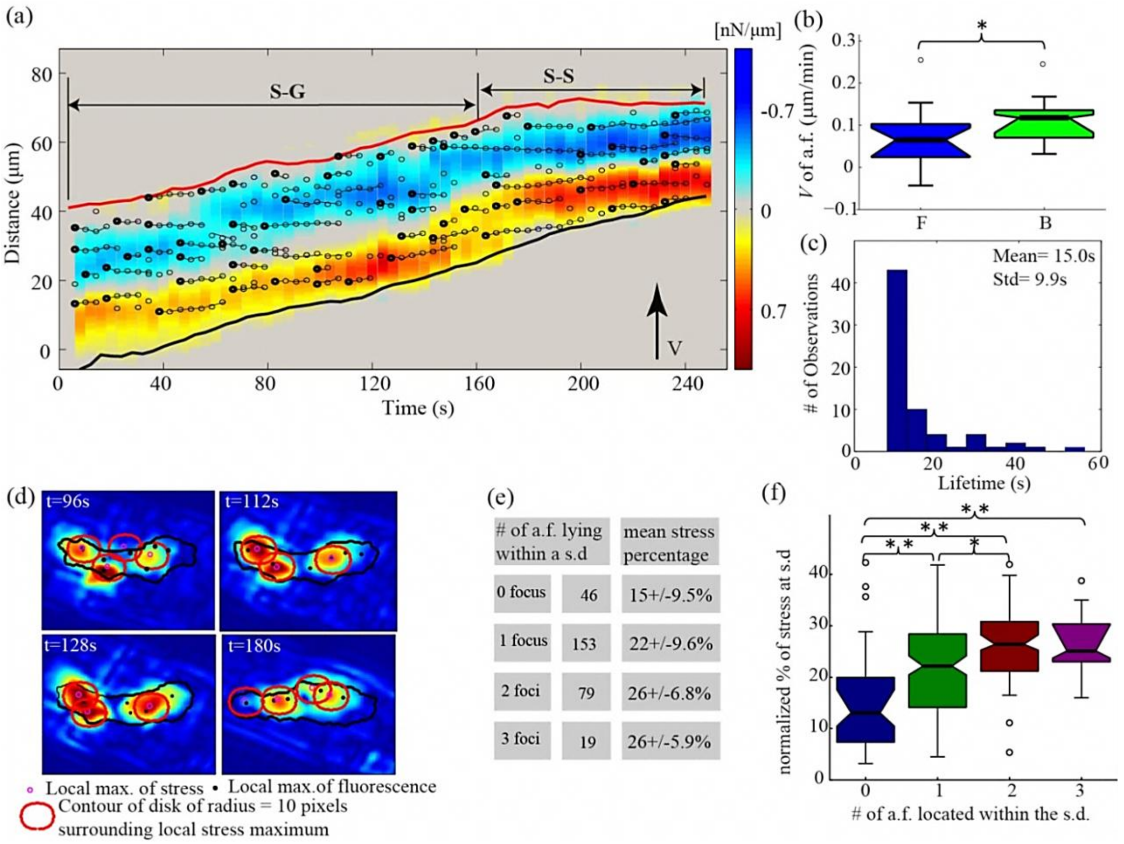

| # of a.f. lying within a s.d | | mean stress percentage |
|---|---|---|
| 0 focus | 46 | 15+/-9.5% |
| 1 focus | 153 | 22+/-9.6% |
| 2 foci | 79 | 26+/-6.8% |
| 3 foci | 19 | 26+/-5.9% |

Figure 3.8: Traction tension kymographs and the spatio-temporal dynamics of the actin foci confirm the existence of motility modes. (a) Traction tension kymograph of the cell shown in Figure 3.7. The local maxima of fluorescence have been tracked and superimposed on the kymograph (black circles). Data points coming from the spatio-temporal evolution of one single actin spot are connected by lines. The appearance of each new spot is highlighted by a bold circle. Adhesion sites at the front of the cell tend to be stationary. Rear adhesions tend to glide forward during the S-G mode and remain stationary during the S-S mode. (b) Boxplot showing the velocity of the adhesion foci tracked and depicted in panel (a) for the half front (F) and half back (B) of the cell. The difference is significant suggesting that the foci at the back slip more than do at the front of the cell and confirming that the frontal adhesion are always stationary. (c) Histogram of the mean lifetime of the adhesion foci tracked and depicted in panel A. Notice that the actin foci are dynamic and transient structures as shown elsewhere (38). (d) Snapshots of the traction stresses (top row) for the representative chemotaxing wild-type cell shown in panel a, in the cell based coordinate system. Stresses are shown in a different colormap to emphasize the local maxima. Black contours show the outline of the cell. Hollow black circles point at calculated local stress maxima and black asterisks point at maxima of fluorescence. A stress disc (s.d.) is defined as a disk that has its center at the position of a certain local maximum and a radius equal to 1μm and all stress disks are shown in red. Notice that most of the actin foci lie within these disks. (e) Table categorizing the stress disks depending on the number of actin foci that lie within them (second column). Notice that the majority of stress disks contain 1 to 2 actin foci. The third column shows the average ratio of the integral of stress within the specific disks to the total integral of instantaneous stresses. The specific value is multiplied by 100 and presented as a percentage. Notice that the more foci a stress disk contains the higher tend to be the stresses applied. (f) Boxplots showing the average ratio of the integral of stress within stress disks (containing 0, 1, 2, and 3 actin foci) to the total integral of instantaneous stresses. Notice that the higher the number of foci that lie within the disks, the more stress applied within the specific stress disk.

strength of the integral of stresses in each "stress" disk. We found that 21%, 26%, 26% of the disks contained 1, 2, 3 foci respectively whereas only 15% of the disks contained zero foci (Figure 3.8.e). Moreover, we found that the magnitude of the integral of stresses within the disks increased significantly when comparing disks that contained 0 versus 1 and 1 versus 2 foci (Figure 3.8.f). Nevertheless, we found no significant difference in the strength of the stresses when comparing disks containing 2 versus 3 foci (plateau) (Figure 3.8.f).

Following the aforementioned analysis, we created stress kymographs and then superimposed the actin foci information on them (Figure 3.7 and Figure 3.8). For every instant of time, we plotted the integral of stresses across the cell width as a function of the cell length. In a similar analogy, we located the actin foci (local maxima) in the instantaneous 2D fluorescence maps and then projected them across the cell length (1D). We developed a code to automatically connect by a line, data points coming from the spatio-temporal evolution of one single actin spot (Figure 3.8.a). After inspecting a large number of individual cells, we concluded that the foci are always localized at the front and back of the cell where the stresses are exerted and not in the middle of the cells where there are typically minimal stresses. We also measured the velocity of gliding of actin foci (the slope of the line that connects in the stress kymograph circles that represent the time history of a specific focus) (Figure 3.8.b). Consistent with our previous findings, we observed that actin foci at the front of the cell tend to be stationary, while rear foci tend to glide forward during the S-G mode and remain stationary during the S-S mode.

## 3.6 Discussion

To shed light on the mechanisms that control amoeboid migration speed, we have used FTFC to measure the spatial and temporal evolution of traction stresses and shape dynamics during migration. This technique, together with the construction of traction tension kymographs, allowed us to study how the formation and disassembly of adhesions coupled with the generation of axial and lateral traction stresses control the migration efficiency of chemotaxing *Dictyostelium* amoebae. We examined the dynamics of locomotion of wild-type cells and demonstrated that wild-type cells control their migration by mainly switching between two motility modes with distinct migration speed, adhesion dynamics, and periodic modulation of axial and lateral contractions of varying strength.

It was previously shown through simultaneous observation of the dynamics of F-actin and traction stresses on *Dictyostelium* migrating cells that forces generated by the cells are transmitted to the substratum at spots where F-actin accumulates (111). This was reconfirmed using interference reflection microscopy indicating that a cell applies the traction stresses at cell-substratum attachment sites, where there is an increased F-actin localization (111). Since our analysis of the dynamics of the locomotion is based on the assertion that the cell is attached to the substrate at the location where we measure the traction stresses, we recorded simultaneously the traction forces and F-actin localization in multiple planes across the height of the cell. We then used the multiple F-actin planes to reconstruct the 3D cell body using the rendering options provided by IMARIS. With this technique, we visually observed where the ventral side of the cell lies and which parts of it are in contact with the substrate or not. By then overlapping the stress maps and ventral F-actin fluorescence maps consecutively in time, we concluded that the localization of the traction stresses precisely coincides with the peaks in fluorescence activity where the adhesions are localized (Figure 3.8).

To examine the dynamics of adhesion formation, we mapped the traction stresses in a new way by creating *traction tension kymographs* (see Materials and Methods). In accordance to previous findings, we found that when amoeboid cells undergo chemotaxis on elastic substrates, they establish, on average, two stationary adhesion sites located at the front and back halves of their cell body and move by periodically modulating the strength of the axial contractility (29, 31). The periodic modulation of the axial contractility coincides with the periodic variation in the cell length and frequency of formation of frontal adhesion, consistent with previous descriptions of the motility cycle

(1, 29). This finding reconfirms that when amoeboid cells chemotax, they follow a relatively coherent (periodic) motion largely dominated by the front protrusion and rear retraction (106, 112).

The stationary nature of the adhesion sites has been mostly investigated in cells that form focal adhesions. For instance in fibroblasts, the protruding lamellipodia form focal adhesions to the substrate that remain stationary until they are ripped off when they reach the back of the cell (50). However, with *Dictyostelium* cells, it has been more challenging to examine the dynamics of adhesion since the receptors controlling the adhesion have not been unambiguously identified and no integrin homologue has been found so far (84). In accordance with our findings, there is evidence suggesting that the adhesion sites in *Dictyostelium* are stationary (38, 106), although these studies do not provide quantitative information nor examine extensively the dynamics of the adhesion sites during migration. Our traction tension kymographs corroborate our findings and provide strong quantitative evidence that the adhesion sites do not always remain stationary while the cell body translocates forward.

Our analysis uncovered several modes of movement with distinct adhesion and contractility dynamics. On a collagen-coated elastic substrate, moving wild-type cells switch between these modes with no apparent order, although the S-S and S-G modes are dominant. *T*he S-S mode, characterized by two discrete adhesion sites located at the front and back halves of the cell, is associated with a slower velocity of migration. Cells protrude an anterior pseudopod that binds to the substrate, forming an anterior adhesion with the former front adhesion that then becomes the posterior adhesion. Both the front and back adhesions remain stationary during the S-S mode with the cell moving across these sites presumably using lateral contractions to allow an almost constant velocity throughout the motility cycle. During the S-S mode, cells protrude an anterior pseudopod, which then binds to the substrate forming an anterior adhesion with the former front adhesion becoming the posterior adhesion. In the S-G mode, the cell also establishes anterior and posterior adhesion sites, but the back adhesion is continuously dragged forward while the magnitude of the traction stresses and motility speed are considerably reduced compared to the S-S mode.

Although the two motility modes have different adhesion dynamics, they also have important characteristics in common. In both modes, the front adhesion sites are stationary, and the frequency of formation of front adhesions determines the cell's speed. Moreover, in both modes, the axial contractility dominates over the lateral one. The signaling and/or mechanical changes responsible for the abrupt switch from one mode to the other are currently unknown. It is possible that slight inhomogeneities of the mechanical or chemical properties of the substrate, either due to the surface topography or in the collagen concentration, could trigger the switch between modes (113). Different motility modes, characterized by varying speed or adhesion dynamics, were observed in other cell types (103, 114). It has been shown that lymphocytes switch between a fast "amoeboid-like" mode that uses sequential, discontinuous contacts to the substrate and a slower mode that uses a single, continuously translating adhesion, similar to mesenchymal motility (103).

In conclusion, our study of the mechanics of wild-type chemotaxing cells has contributed to a more precise understanding of how the coordination of traction stresses together with the adhesion dynamics result in efficient amoeboid cell migration. We have shown that cells migrate by switching between several modes of distinct adhesion dynamics, while at the same time following a motility cycle. Our findings also reveal that changes in cell migration speed are concomitant to changes in both contractility and adhesion dynamics.

Chapter 3 is being prepared in part for publication. Chemotaxing amoeboid cells migrate by switching between distinct modes of adhesion dynamics and contractility. Bastounis E., Meili R., Alvarez-Gonzalez B., del Álamo J.C., Lasheras J.C., Firtel R.

# Chapter 4

# Role of the Scar/WAVE Complex in Regulating Traction Forces during Amoeboid Motility [†]

A key driver for the protrusion of the leading edge and the generation of cell movement is F-actin polymerization. The dynamic regulation of the actin cytoskeleton is spatiotemporally coordinated by upstream signaling regulators, including actin nucleators, and by actin cross-linking proteins whose combined activity results in pseudopod protrusion (45). One important mechanism for F-actin growth is filament branching (dendritic polymerization) initiated by the Arp2/3 heptameric complex (50-53, 55, 56, 64) and regulated by nucleation promotion factors (NPFs), the WASP and SCAR/WAVE protein complexes (Figure 1.2) (115). The highly conserved SCAR/WAVE complex includes PIR121 (Sra-1/CYFIP/GEX-2), SCAR (WAVE), HSPC300, ABI1, and NAP1 (Hem2/KETTE/GEX-3), which have domains that bind and activate Arp2/3, as well as domains that recognize and bind to signaling factors (membrane phospholipids, Rho family GTPases, tyrosine kinases) to locally activate the complex (66, 115). Unlike mammalian cells that lack SCAR protein, *Dictyostelium* cells lacking SCAR (*scrA*$^-$ cells) can still move, albeit with reduced chemoattractant-induced F-actin polymerization, presumably by employing other NPFs such as WASP (116). On the other hand, *Dictyostelium* cells lacking Pir121 (*pirA*$^-$ cells) undergo increased F-actin polymerization, enhanced pseudopod activity, and reduced substrate adhesion (64, 65).

Misregulated dendritic actin polymerization causes a decrease in cell speed and changes in cell shape (66, 117). Despite a growing body of data on the biochemical processes controlling cell

---

[†] Chapter 4 has been published in part in the Molecular Biology of the Cell journal. The SCAR/WAVE complex is necessary for proper regulation of traction stresses during amoeboid motility. Bastounis E., Alonso-Latorre B., Meili R., del Álamo J.C., Lasheras J.C., Firtel R.

motility and F-actin polymerization in particular, our knowledge of how these biochemical events are linked to the spatiotemporal mechanics of cell movement is still in its infancy. Is the decrease in the migration speed of the cell due to an increase of the time needed for the pseudopod to protrude (protrusion phase)? Or, does the misregulation of F-actin polymerization affect the duration of the other phases of the motility cycle as well (contraction of the cell body, retraction of the rear)? Is there still a motility cycle present when F-actin branching in the front of the cell is disrupted? How does the misregulation of F-actin polymerization affect the localization and magnitude of the traction stresses exerted by the cells on their substrate? The objective of this chapter is to answer the aforementioned questions. In order to understand the relationship between the mechanics and biochemistry needed to make a comprehensive description of cell motility, we used traction force cytometry (TFC) techniques, in combination with statistical analysis, to define the traction stress fields of the SCAR/WAVE-complex mutants and to compare them with wild type. Thus, we were able to examine how enhanced or reduced F-actin polymerization alters the biomechanics of chemotactic cell migration. In particular, we were driven by the need to better determine the role of anterior F-actin polymerization in each of the steps of the motility cycle and in mediating the strength and timing of the applied traction forces required for cell movement as well as the adhesion dynamics.

## 4.1 Disruption of the SCAR/WAVE Complex Strongly Affects Cell Shape and Speed of Cells Chemotaxing on Elastic Substrates

To examine the role that SCAR/WAVE mediated dendritic polymerization of F-actin plays in regulating the synchronized mechanics of amoeboid motility, we acquired time-lapse images of two SCAR/WAVE complex mutant strains (*scrA*$^-$ and *pirA*$^-$ cells) moving up a chemoattractant gradient on the surface of a polyacrylamide matrix, as described in Chapter 3 for wild-type cells (Chapter 3, Experimental Methods). When the cells move, they deform the substrate, producing time-dependent displacements of the beads. We used traction force cytometry and field statistical analysis to compare the behavior of wild-type, *scrA*$^-$, and *pirA*$^-$ cells. Previously, *scrA*$^-$ and *pirA*$^-$ cells were shown to have decreased or increased F-actin levels respectively (117).

### 4.1.1 Basal F-actin levels correlate with migration speed

In agreement with previous reports (117), we found that both *scrA*$^-$ and *pirA*$^-$ cells chemotax with approximately half the velocity of wild-type cells (Figure 4.1.a and Figure 4.2.a-c). Moreover, both mutants were less polarized than wild-type (Figure 4.1.b). In addition, *scrA*$^-$ cells have a reduced area (Figure 4.1.c-e). Also in agreement with previous studies (117), *pirA*$^-$ cells have 50% more F-actin/cell than wild-type cells, while *scrA*$^-$ cells have 30% less F-actin/cell than wild-type (Figure 4.1.f and Figure 4.2.e).

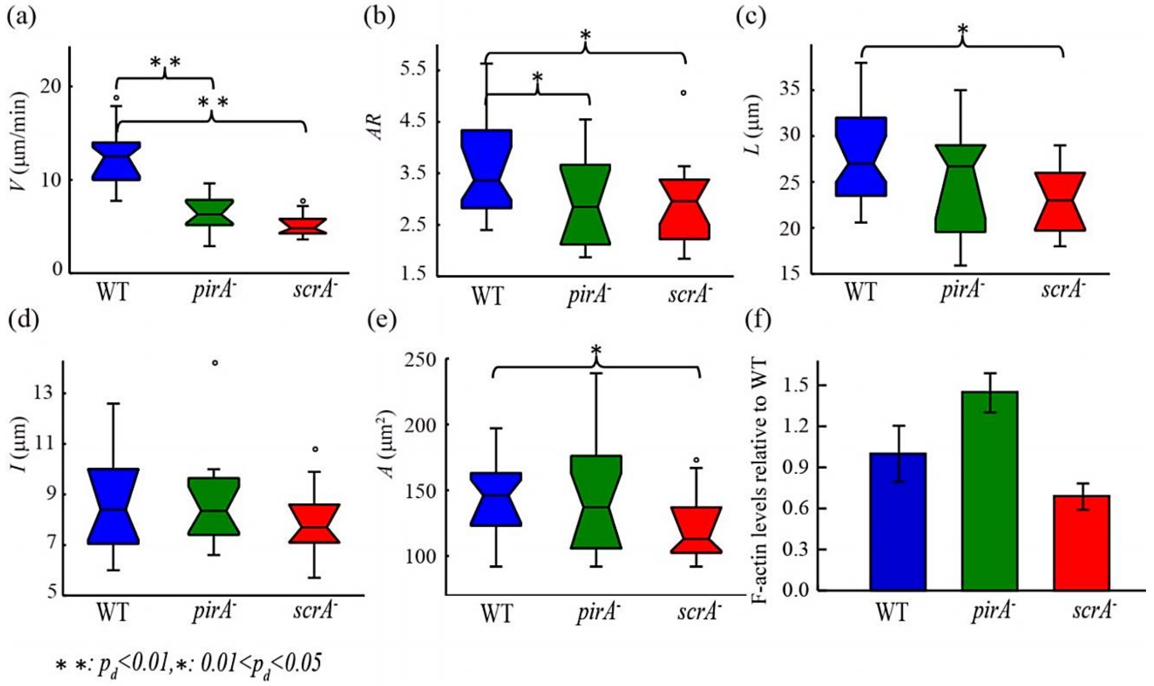

Figure 4.1: Boxplots of kinematic parameters of chemotaxing wild-type (blue), *pirA*$^-$ (green), and *scrA*$^-$ (red) cells. (a) Speed of migration (µm/min). (b) Aspect ratio (cell length divided by cell width). (c) Cell length (µm). (d) Cell width (µm). (e) Area (µm$^2$). Open circles represent outliers, and the notched section of the boxplots shows the 95% confidence interval around the median. Asterisks denote significant differences between distributions: *, $0.01 < p_d < 0.05$; **, $p_d < 0.01$ (Wilcoxon rank sum test for equal medians). (f) Levels of F-actin of unstimulated cells normalized by the corresponding levels of unstimulated wild-type cells (F-actin assay). Error bars, SD from the average.

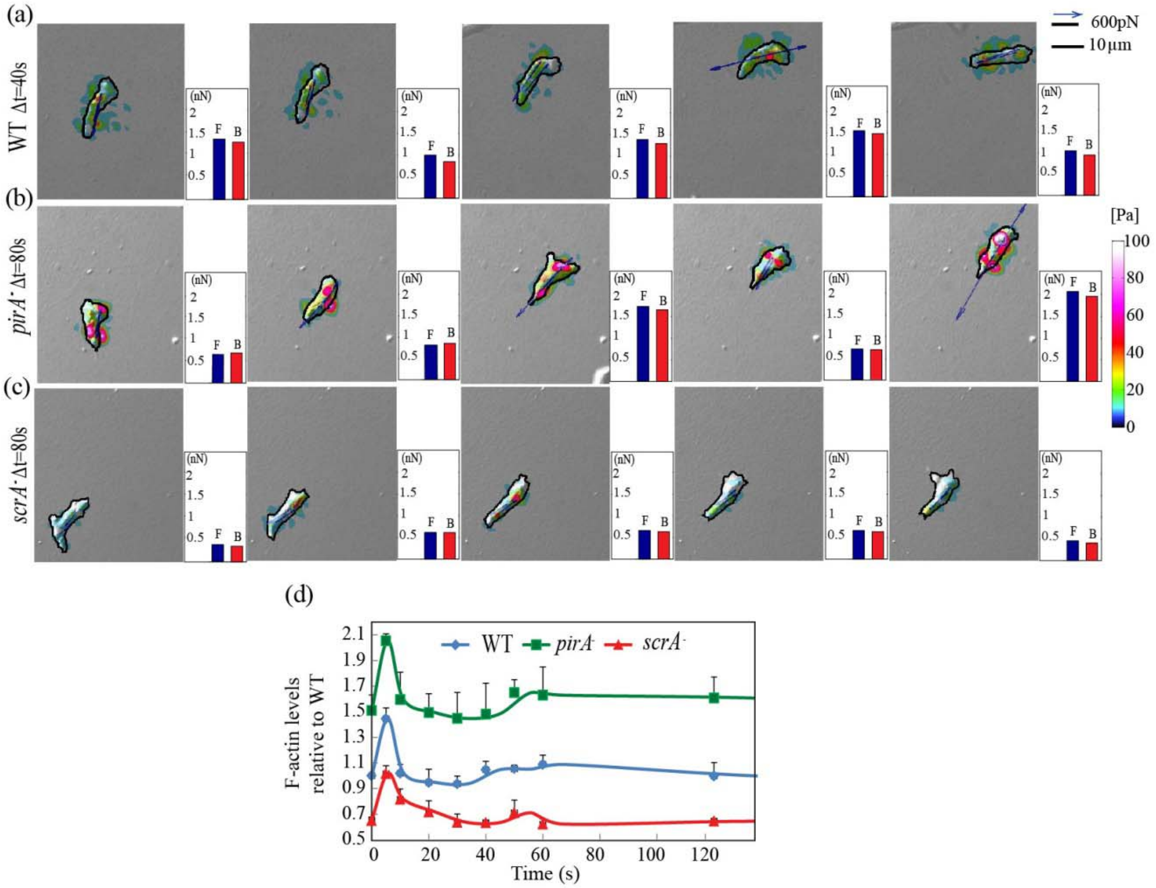

Figure 4.2: The motility phenotype and the mechanics of migration of the Scar/Wave mutants differ considerably from wild type. (a) Time-lapse images of a representative wild-type ($\Delta t$ =40 s) (a), *pirA*$^-$ ($\Delta t$ = 80 s) (b), and *scrA*$^-$ ($\Delta t$ = 80 s) (c) cell. The color map shows the magnitude of the stresses applied to the substrate. The blue arrows show the pole forces applied by the cells. The bar plots on the right of each time-lapse image represent the magnitude of the pole forces exerted on the cell's front F (blue) and back B (red); the similar values of the F and B pole forces indicate that cells are in quasi-static equilibrium. Note the differences in the migration speeds and stresses exerted by the cells of each different cell line. All cells show a marked degree of polarization and apply pole forces simultaneously contracting front and back towards the cell's center. (d) cAMP-induced F-actin polymerization was assessed as described in (Chung and Firtel, 1999). cAMP-induced F-actin levels during different time points after stimulation for the three cell lines, normalized with respect to the corresponding levels of unstimulated wild-type cells.

### 4.1.2 Cell shape is less polarized than wild-type cells

In contrast to Blagg et al. (66, 117) who observed frequent, multiple leading edge formations in both mutant cell lines, we did not observe such extreme phenotypes in our experiments (66, 117) (Figure 4.2.a-c). This difference may be due to differences in the experimental conditions, since our experiments were not performed under agar, and thus, the cells were not constrained in the z direction.

increased pseudopodal activity that is superimposed on the length oscillation mode that drives motility (Figure 4.2.d).

## 4.2.Disruption of the SCAR/WAVE Complex Causes the Misregulation of the Motility Cycle

As described in Chapter 3, wild-type amoeboid cells move by following a series of well-defined steps that result from periodic oscillations of the cell length *L(t)* (30, 40) and of the strain energy $U_s(t)$ deposited on the substrate (30, 31, 37, 38, 107) (Figure 4.3.a). To assess the importance of properly regulated F-actin polymerization for the periodicity of the motility cycle, we examined and compared the temporal evolution of cell length, *L(t)*, and strain energy, $U_s(t)$, in wild-type and the SCAR/WAVE complex mutant strains during chemotactic migration. To that end, we calculated the autocorrelation of *L(t)* and $U_s(t)$ signals as well as their cross-correlation to determine the periodic content of each signal and the correlation between signals as described previously (Figure 4.3.a-b, Materials and Methods).

### 4.2.1 *pirA*$^-$ do not chemotax periodically

The average *p*-values obtained suggested significant correlations (quality of fit) for wild-type and *scrA*$^-$ cells ($p$<0.005) only, indicating quasi-periodic oscillations of the cell length and strain energy (mechanical work) for *scrA*$^-$ cells in a manner similar to the one previously shown for wild-type cells (30). In contrast, the *p*-value (hypothesis of no correlation) for *pirA*$^-$ cells was >0.09 for both time records, indicating that these cells exhibit a more random and uncoordinated variation in both time records during migration (Figure 4.4.a-d). These observations suggest that the mis-regulation of F-actin polymerization observed for *pirA*$^-$ cells results in a more random sequence of protrusions, contractions and retractions leading to aberrant cell motility.

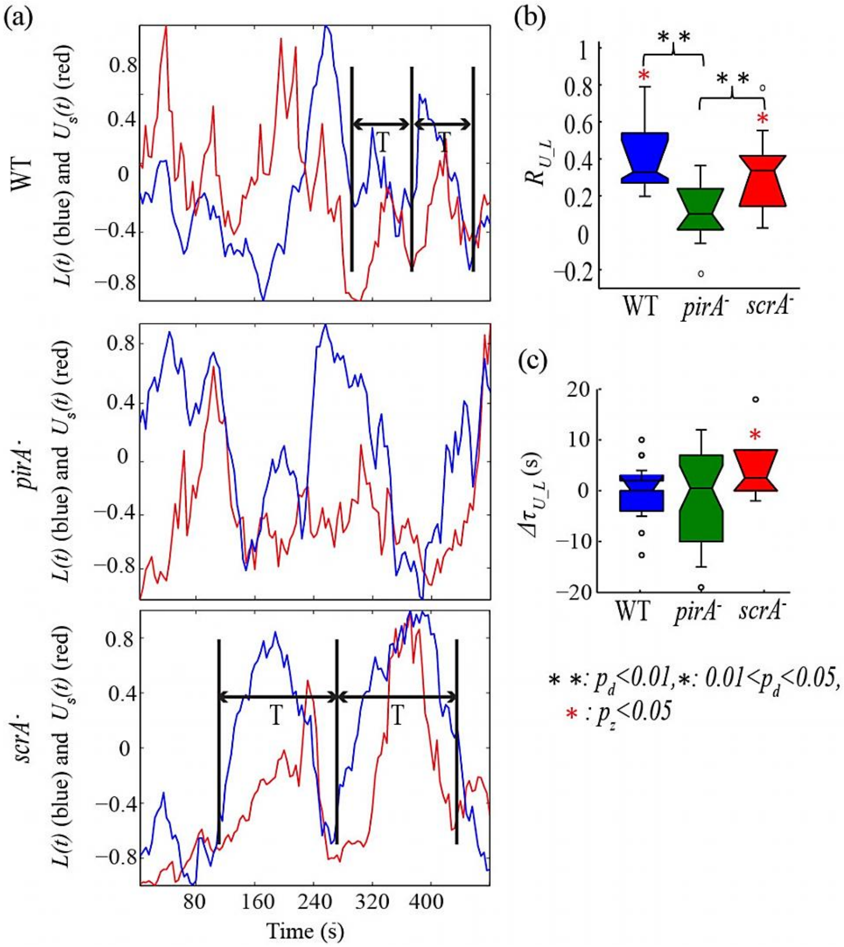

Figure 4.3: The cell length and strain energy time records do not correlate for *pirA*⁻ cells. (a) Time evolution of the cell length *L(t)* (blue) and of the strain energy $U_s(t)$ (red) of a representative cell for each cell line. The amplitude of the variations in both records have been normalized between [-1 1]. *T* indicates the period determined through the autocorrelation function of cell length time record. (b) Boxplots of the correlation coefficients, $R_{L\_U}$, between the time evolution of the strain energy, $U_s(t)$, and the cell length, *L(t)*, for each cell line. Boxplots refer to wild-type (N = 18, blue), *pirA*⁻ (N = 16, green), and *scrA*⁻ (N = 16, red) cells. Black asterisks, significant differences between distributions: *, $0.01 < p_d < 0.05$, **, $p_d < 0.01$; red asterisks, a distribution with a median significantly different from zero: *, $p_z < 0.05$ (Wilcoxon signed rank test). **(c)** Boxplots of the time delay between the cell length and the strain energy ($\Delta\tau_{U\_L}$), where the cell length serves as the reference function. Boxplots refer to wild-type (N = 18, blue), *pirA*⁻ (N = 16, green), and *scrA*⁻ (N = 16, red) cells. Black asterisks denote significant differences between distributions, while red asterisks indicate a distribution with a median significantly different from zero: $p<0.05$ (Wilcoxon signed rank test for zero median). Note the non-zero positive delay in the *scrA*⁻ with a median value of 2.5 s ($p=0.011$).

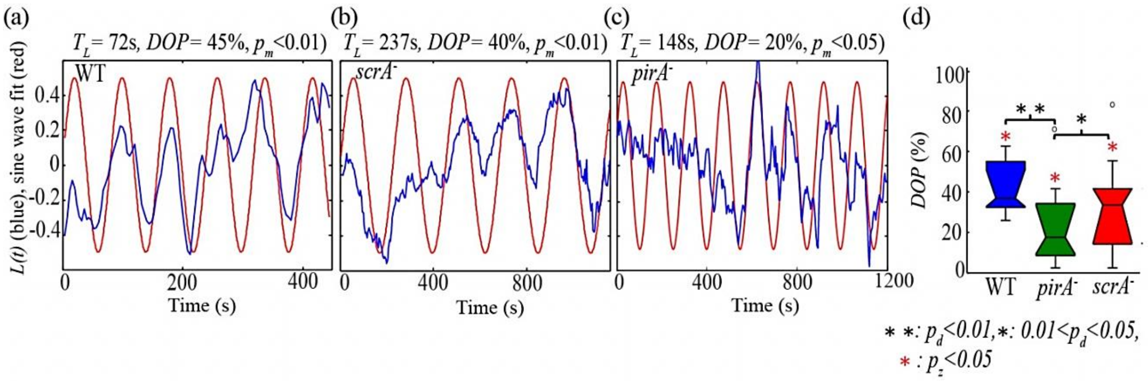

Figure 4.4: *pirA*$^-$ cells do not follow a motility cycle while chemotaxing. (a) Method used to calculate the degree of periodicity (*DOP*) by fitting a sine wave (red) to the cell length *L(t)* time record (blue) of a representative cell for each cell line. The period $T_L$, the degree of periodicity *DOP*, and the p-value $p_m$ for testing the hypothesis of no correlation between the cell length and the sine wave fit are also shown. (b) Boxplots of the *DOP* of the time evolution of the cell length L(t). Boxplots refer to wild-type (N = 29, blue), *pirA*$^-$ (N = 18, green), and *scrA*$^-$ (N = 17, red) cells.

### 4.2.2 No correlation between cell length and strain energy oscillations for *pirA*$^-$ cells

The correlation coefficients between $L(t)$ and $U_s(t)$ for *scrA*$^-$ cells, similar to wild type, were found significantly greater than zero, based on p-value tests, suggesting that the cell length, as represented by the length of the major moment of inertia of the cell, oscillates periodically and in-phase with the strain energy (Figure 4.3.a-b). In marked contrast, the cross-correlation coefficients were much lower for *pirA*$^-$ cells and not significantly different than zero (Figure 4.3.b). This indicates that *pirA*$^-$ cells do not oscillate their length and strain energy in a periodic manner and suggests that the motility of *pirA*$^-$ cells is less coordinated. We also observed an average 4.3 s time delay between the two time records for *scrA*$^-$ cells, representing a statistically significant increase based on p-value tests (Figure 4.3.c). According to this result, cell lengthening occurs ~4 s prior to force exertion for *scrA*$^-$ cells, suggesting a considerable time delay in generating forces as compared to the wild type where cell lengthening and an increase of force exertion on the substrate occur nearly simultaneously (at least within the time resolution of our experiments).

## 4.3 The Frequency of the Motility Cycle and Distance Advanced per Cycle Decrease in Cells Lacking SCAR

We observed previously that wild-type cells and strains with contractility deficiencies (myosin II heavy chain null cells, myosin II essential light chain null cells) exhibit in-phase quasi-periodic oscillations of their cell length and strain energy (31). Furthermore, the speed of migration of these cells ($V$) is linearly proportional to the step length λ (the step length advanced by the cell per cycle) and the frequency $\omega$ of these oscillations according to the relation $V = 2\pi\omega\lambda = \lambda/T$ . Figure 4.5.a suggests that *scrA*⁻ cells also exhibit a strong correlation between their average migration speed $V$ and the frequency of their motility cycle $\omega$, the same way wild-type cells do. Interestingly, the step length is shortened significantly for *scrA*⁻ cells, as shown in Figure 4.5.a-b from the slope of the linear fits to the data (dashed lines), which represent the average values of λ for each strain and the boxplots. Within the population of *scrA*⁻ cells, we found that the value of λ does not correlate with the size of the cells, suggesting that the cause of the reduced value of λ for *scrA*⁻ cells is, most likely, not due to their smaller cell size (Figure 4.5.d). It should be noted that in Figure 4.5.a, the frequencies were calculated from the cell length, *L(t)*, but identical results were obtained for $U_s(t)$ since both signals are highly correlated in wild-type and *scrA*⁻ cells (Figure 4.5.b-c).

Figure 4.5.a illustrates that the motility cycle of *scrA*⁻ cells has a longer period (i.e. lower frequency) than wild-type cells. We previously segmented the motility cycle into four phases protrusion, contraction, retraction, and relaxation based on the changes in cell length and traction forces which were based on similar analyses as described in this work (2, 33, 45). We also showed

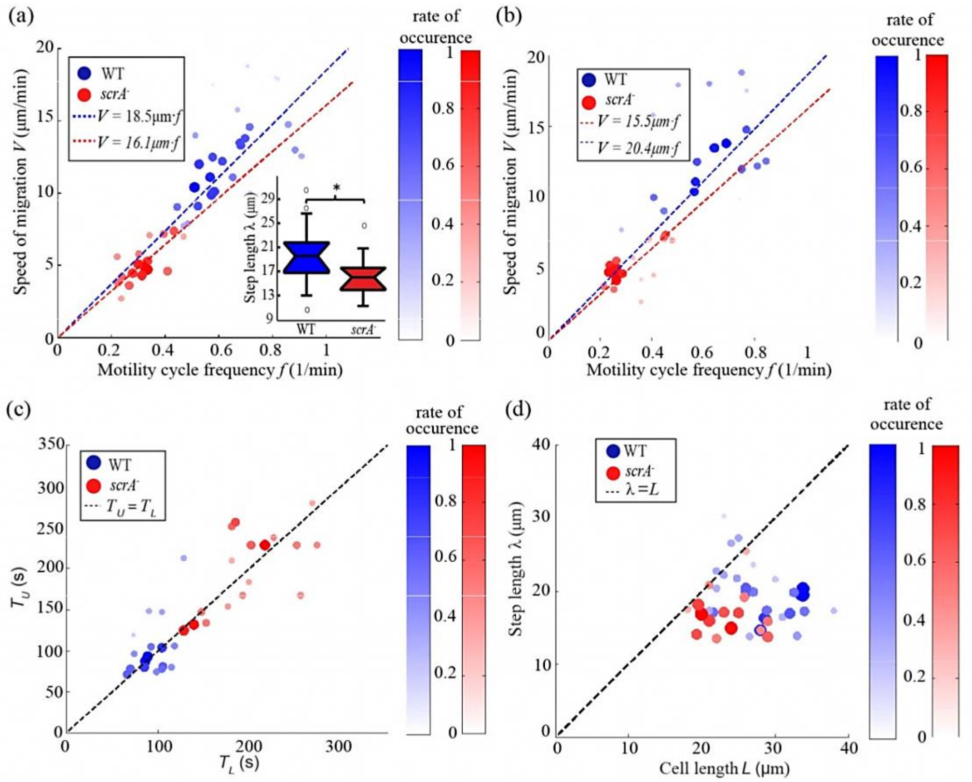

Figure 4.5: The frequency of the motility cycle is determined by the speed of the cells but *scrA*$^-$ travel a lower distance per cycle than wild-type. (a) Scatter plot of the average speed of migration $V$ versus the frequency $f$ of their motility cycle determined through the time evolution of cell length, $L(t)$ (N = 46). The data points refer to N = 29 wild-type (blue circles) and N = 17 *scrA*$^-$ cells (red circles). The dashed blue and red lines are the least square fits to the data for wild-type and *scrA*$^-$ cells, respectively. $V = 18.5\times f$ for wild-type and $V = 16.1\times f$ for *scrA*$^-$ cells, showing that the *scrA*$^-$ cells perform a motility cycle with an average step length of 16.1 μm vs. the 18.5 μm in the wild-type cells. The root mean square errors (RMSEs) when fitting the data linearly were $\text{RMSE}_{\text{WT}} = 3.20$ and $\text{RMSE}_{\text{scrA}} = 0.99$. The correlation coefficients of the two variables were $R_{\text{WT}} = 0.364$ and $R_{\text{scrA}} = 0.785$. To better visualize the correlation, the $f$–$V$ plane was divided into rectangular tiles of equal area, and the size and color of each data point were scaled according to the total number of data points that fall on each specific tile (i.e., its rate of occurrence). As a result, darker, larger circles represent those data points that were observed more often in our experiments, and vice versa. A boxplot of the average step length $\lambda$ advanced per period is shown on the bottom right corner of the plot. Asterisks denote significant differences between distributions: *, $0.01 < p_d < 0.05$; **, $p_d < 0.01$. (b) Scatter plot of the average migration speed of chemotaxing cells (N = 34) versus the frequency of their motility cycle, determined using the strain energy $U_s(t)$ time record. The data points come from N = 18 wild-type (blue circles) and N = 16 *scrA-* (red circles) cells. The dashed blue and red lines are the least square fits to the data, yielding $V = 20.4\times f$ for wild-type and $V = 15.5\times f$ for *scrA*$^-$ cells. Note that the step lengths calculated from the time records of the cell length shown in panel (a) are within 10% of those calculated here with the strain energy, showing the high degree of correlation between these two parameters. As it was the case in panel (a), the average step length per cycle is shown to be markedly reduced in the *scrA*$^-$ cells (almost a 25% reduction). (c) Scatter plot of the periods determined through the cell length, $T_L$ versus the periods determined through the strain energy, $T_U$, indicating the high degree of correlation between these two functions. The dashed black line is $T_L = T_U$. (d) Scatter plot of the step length λ versus the length of the cell $L$. The dashed black line is λ=L. In all three panels, the size and color of each data point are proportional to its rate of occurrence, similar to panel (a).

that the longer period observed in *scrA⁻* cells was the result of a considerable increase in the time duration of the protrusion phase and, to a lesser extent, to the duration of the retraction phase (Figure 4.10.b). This will be discussed in greater detail further on.

## 4.4 The Magnitude of the Front to Back Contraction Forces (Pole Forces) Correlates with F-actin Levels

A critical question not yet addressed is: what effect, if any, does the misregulation of F-actin polymerization have on the localization and magnitude of the traction stresses exerted by the cells on their substrate on average as well as during the different stages of their motility cycle? To answer that, we determined the cell shape changes and calculated the associated distribution of traction stresses from the measured deformation of the elastic substrate (Figure 4.2.a-c, see Materials and Methods). To answer the second part of the question, for the cell lines exhibiting a motility cycle, we used conditional statistics to characterize the traction stresses exerted by the cells during the different phases of their motility cycle (29).

### 4.4.1 Traction stress strength correlates with basal F-actin levels

Figure 4.6.a shows the average stress patterns over multiple motility cycles for all three strains. Figure 4.6.a confirms that for all strains the average stress pattern consists of the localized attachment at the cell's front and back, contracting the substrate towards the cell's center in a similar pattern to that found in our previous observations of wild-type cells moving on gelatin substrates (Figure 4.6.a and Figure 4.7) (30). However, while the overall force pattern is conserved in the SCAR mutants, the magnitude of the traction stresses is quite different. *scrA⁻* cells exert ~50% weaker traction stresses, while the traction stresses exerted by *pirA⁻* cells are slightly larger than those of wild-

type cells. The average magnitude of the pole forces transmitted to the substrate (pairs of opposing contractile forces resulting from the integral of the traction stresses at the front and back of the adhering to the substrate cells) decreases from 1100 pN for wild-type cells to 473 pN for *scrA*$^{-}$ cells and increases to 1249 pN for *pirA*$^{-}$ cells. Similarly, the average strain energy (mechanical work) exchanged with the substrate in wild-type and *pirA*$^{-}$ cells are 0.56 nNμm and 0.7 nNμm respectively, whereas the strain energy for *scrA*$^{-}$ is only 0.13 nNμm (Table 4.1).

Table 4.1: Summary and comparison of the average motility parameters for wild type and Scar/Wave mutants. Rows show different cell types (C.T.). First five columns: cell type; average values of the pole forces obtained from the integration of the stresses in the front and the back halves of the cells ($F_p$); average magnitude of the pole forces normalized by the cell area ($F_p/A_c$); average strain energy ($U_s$); average strain energy normalized by the cell area ($U_s/A_c$). The last two columns show the average protein amount (P.A.) in μg/cell (DC assay) for each cell line and the average protein amounts in the mutants compared with that measured in wild-type cells

| C.T. | $F_p$ (nN) | $F_p/A_c$ (pN/μm$^2$) | $U_s$ (nN μ m) | $U_s/A_c$ (pN/ μ m) | P.A. (μm/cell) | P.A. |
|---|---|---|---|---|---|---|
| WT | 1.08+/-0.44 | 8.68+/-4.49 | 0.64+/-0.35 | 5.4+/-3.2 | 8.33x10$^{-5}$ | 100% |
| *pirA* | 1.24+/-0.68 | 9.97+/-1.75 | 0.86+/-0.41 | 6.6+/-3.5 | 7.76x10$^{-5}$ | 93% |
| *scrA* | 0.60+/-0.28 | 4.49+/-1.96 | 0.23+/-0.11 | 1.2+/-1.1 | 6.54x10$^{-5}$ | 78% |

These differences cannot be attributed simply to differences in cell size between the strains, since statistics of both the pole force and the strain energy per unit area of the cell (Figure 4.6.a, c) reveal that adhesion to the substrate is significantly stronger in wild-type and *pirA*$^{-}$ cells compared to *scrA*$^{-}$ cells. As *scrA*$^{-}$ cells exhibit reduced F-actin, while there is an increase in F-actin in *pirA*$^{-}$ cells (Figure 4.1.f) (66, 117), it is possible that the differences in the magnitude of the cellular traction forces may be partially due to the changes in the levels of polymerized actin present in the cells.

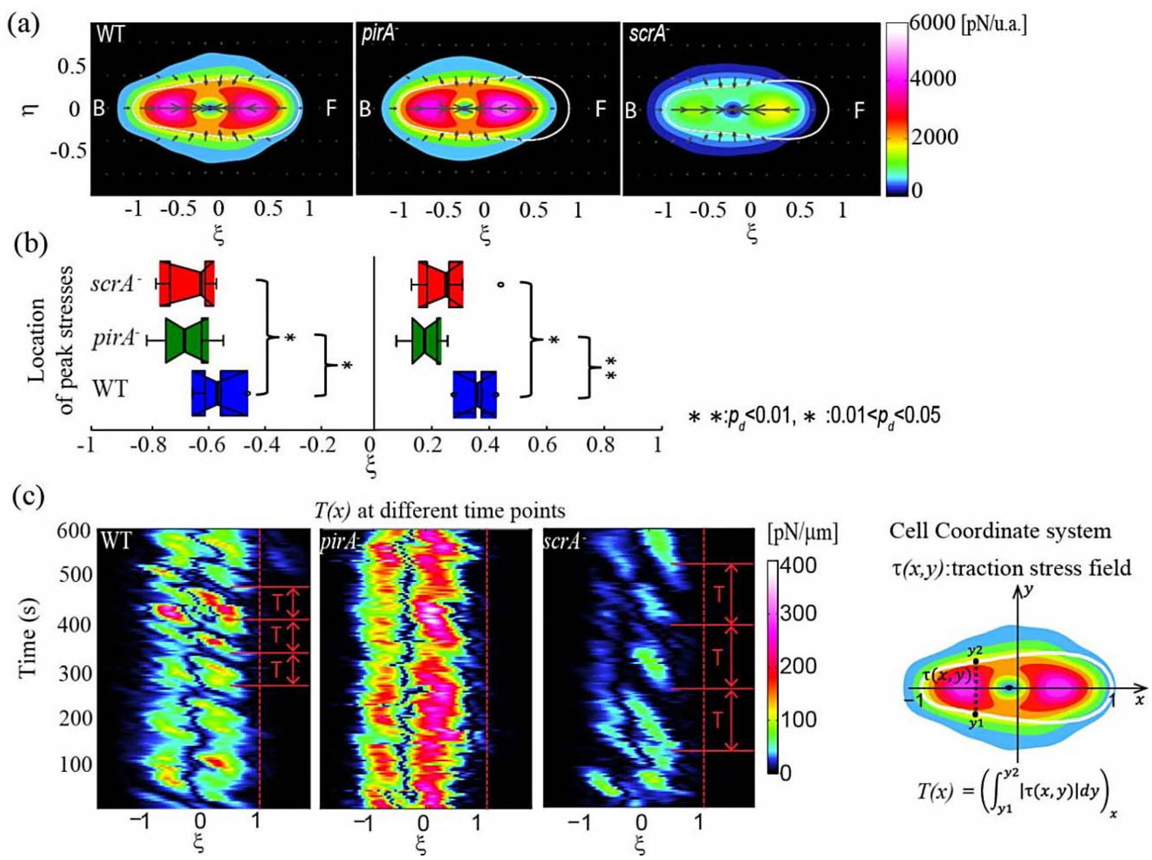

Figure 4.6: Strength of the traction stresses differs on the Scar/Wave mutants and correlates with their F-actin levels. (a) Average stress distribution pattern for wild-type (N = 14), *pirA*⁻ (N = 17), and *scrA*⁻ (N = 14) cells during chemotaxis on elastic polyacrylamide substrate. The contour maps show the average traction stress field, computed in a reference frame rotated to have the *x*- and *y*-axes coincide with the instantaneous principal axes of the cells. All dimensions are scaled with the length of their instantaneous major axis, a. Details of how the cell-coordinate system used in these plots is constructed can be found elsewhere (29). The colors indicate the magnitude of the stresses in pN/unit area, and the arrows indicate their direction. The white contours show the average shape of the cells in this reference frame. The front (F) of the cell corresponds to x > 0 and the back (B) to x < 0. (b) Boxplot showing the average location of the peak stresses at the front and back halves of the cell along the cell length calculated after integrating along the cell width, for wild-type (blue), *pirA*⁻ (green) and *scrA*⁻ (red) cells. The peak stresses are significantly closer to the cell centroid in the mutants than in wild-type, while the opposite happens for the peak stresses at the back half of the cell. (c) Time evolution of the magnitude of the integral of the traction stresses along the width of the cell as a function of the position along the cell length for a representative wild-type, *pirA*⁻, and *scrA*⁻ cell (sketch). Dashed lines indicate the cell front. The adhesion sites of the cell can be clearly seen, as well as the frequency of the formation of frontal adhesions, which coincides with the measured period of the motility cycle (*T*).

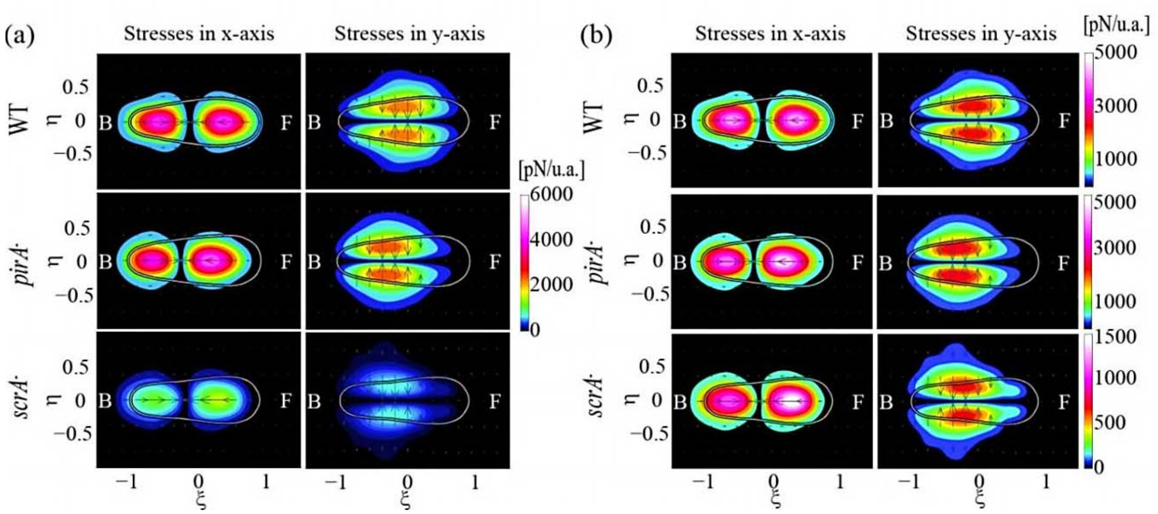

Figure 4.7: Both wild-type and the Scar/Wave mutants move by contracting predominantly axially. (a, b) Components of the traction stresses parallel and perpendicular to the major axis (length) of the cell. In (a) the stresses are shown using the same color map for all cell lines whereas in (b) the color map for each cell line is normalized by the maximum value of the traction stresses in each cell line.

### 4.4.1 Leading edge of the mutants does not exert stresses

In addition to the altered magnitude of the stress applied to the substrate by the mutants, we found that the leading edge of both SCAR/WAVE mutant strains does not exert significant traction stresses (Figure 4.6.b, c). The location of the local maximum in the magnitude of the traction stresses in the mutant cells is shifted towards the center of the cell when compared to that observed in wild-type cells. This shift of the region of the frontal attachment may be due to either defective/decreased attachment of the leading edge of these cells or perhaps to fast blebbing of F-actin free protrusions. However, prompted by earlier findings showing that during cytokinesis *scrA*$^-$ cells produce numerous bulbous projections which do not contain actin, we carefully examined the localization of F-actin in chemotaxing cells (118, 119). In our experiments, actin remained localized at the front of the leading edge, suggesting that there is minimal to no bleb formation (Figure 4.12.a-b).

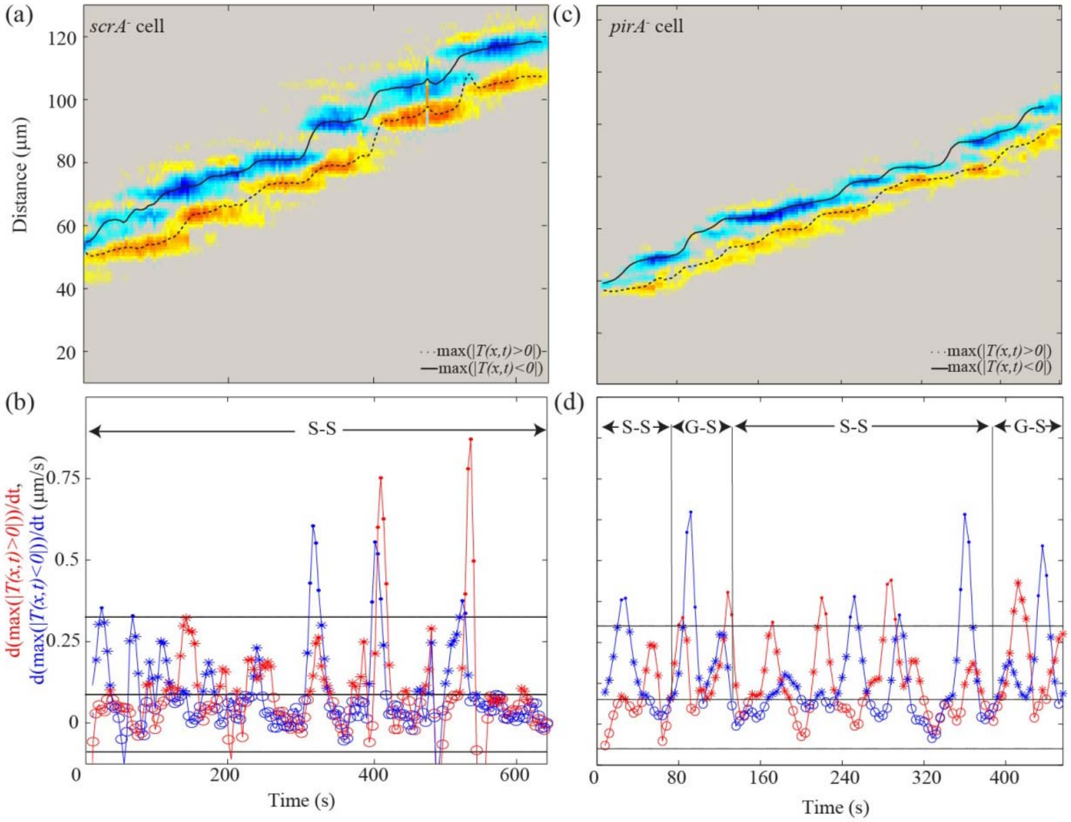

Figure 4.8: Identification of the motility modes of the Scar/WAVE mutants. (a) Traction tension kymograph of a representative *scrA⁻* cell (see Figure 3.2.a). Black solid (dotted) lines track the spatio-temporal evolution of the peak value of the negative (front) (positive (back) traction tension, *T(x,t)*. (b) Criterion for the identification of the motility modes based on the speed of adhesion regions. Blue and red solid lines show the speed of the adhesion regions, defined as the slope of the solid and dotted lines in panel A. Black solid lines indicate the first and third quartiles of the distribution of the adhesion speeds. Speed points that are lower than the first quartile are marked with a hollow circle, while those between the first and third quartiles are marked with an asterisk. Speed points above the third quartile were observed only when new adhesions were created or existing adhesions were broken (see Figure 2.5). Notice that *scrA⁻* cells move by exclusively implementing the S-S motility mode. (c) Same as panel (a) for a representative *pirA⁻* cell. (d) Same as panel B for the cell shown in panel (c).

### 4.4.3.*scrA⁻* implement only the S-S motility mode while *pirA⁻* switch between the S-S and G-S motility modes

As in Chapter 3, we calculated the integrals of stresses across the width of the chemotaxing mutants and plotted them during time, creating traction tension kymographs. We found that *scrA⁻* keep both their frontal and back adhesions stationary, thus implementing only the S-S mode (Figure 4.8.a-b). This suggests that *scrA⁻* cells chemotax similarly to the wild type, but are unable to implement the

S-G mode which is associated with higher migration speed. Nevertheless, we found that unlike wild-type, *scrA*$^-$ cells have, on average, two to three adhesion sites along their length (Figure 4.8.a). A frontal adhesion is created at the front of the cell usually before the previous frontal adhesion has become a back adhesion. Moreover, in certain circumstances when an adhesion is created at the front, it exerts stresses that are pointing towards the front of the cell (Figure 4.8.a). Finally the frontal adhesion formation usually occurs farther away from the leading edge as observed by the calculation of the average stress maps (Figure 4.8.a).

*pirA*$^-$ cells, similar to *scrA*$^-$ cells, have, on average, two to three adhesion sites along their length (Figure 4.8.c). In marked contrast to *scrA*$^-$ cells, the adhesions that they form at their front are not always stationary, but occasionally slide forwards or backwards (Figure 4.8.c-d). Thus, *pirA*$^-$ cells migrate by switching between the S-S and the G-S motility modes (Figure 4.9.a). This suggests that potentially due to the cytoskeletal defects of these cells or the disorganized architecture of the F-actin network, *pirA*$^-$ cells are unable to grab the substrate strongly and maintain their frontal adhesion still. It is interesting that for both mutants the back adhesions are always stationary as opposed to what is observed in the case of wild-type cells. Both mutant strains were transformed with *Lifeact.* Determination of the time history of the actin foci, reconfirmed the above observations.

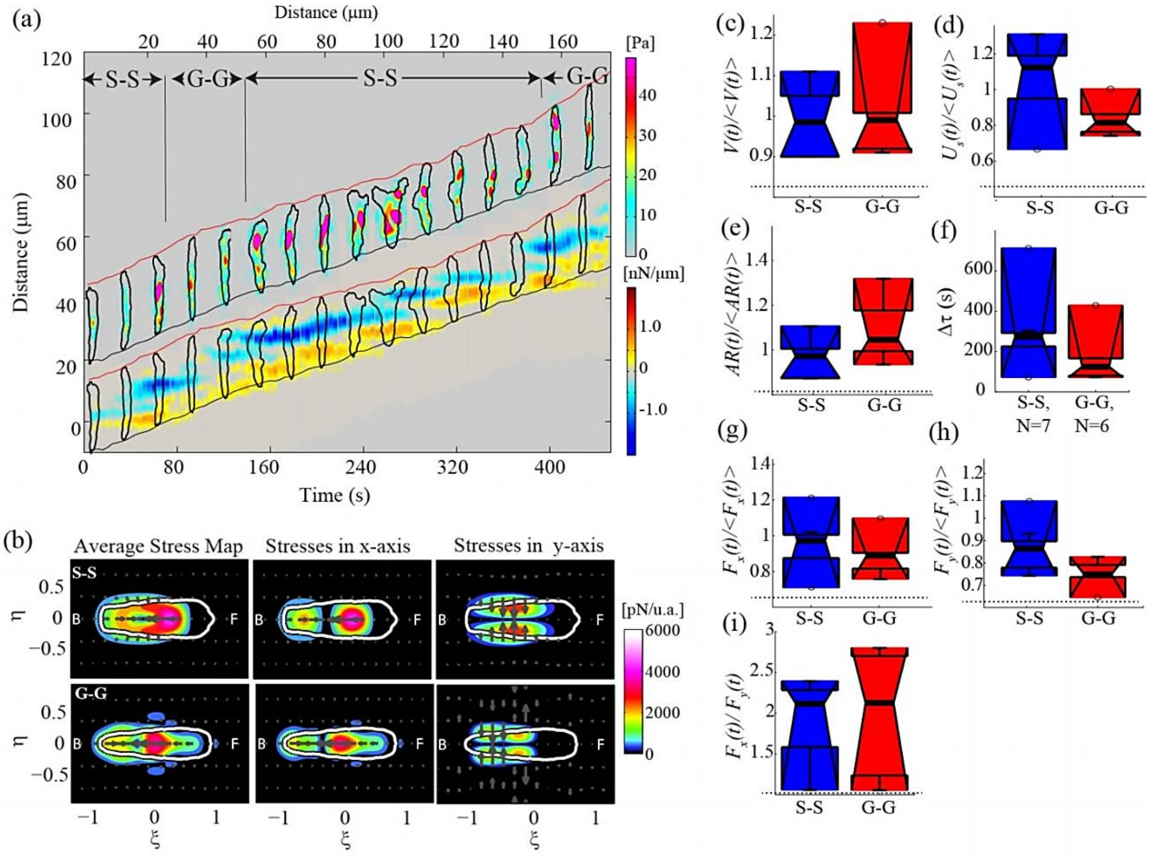

Figure 4.9: Spatio-temporal dynamics and motility modes in *pirA*<sup>-</sup> cells migrating on collagen-functionalized polyacrylamide substrata. (a) Kymographs of traction stresses $\tau(x,y)$ (upper part) and traction tension $T(x,t)$ (lower part) for a representative chemotaxing *pirA*$^-$ cell (for explanation see Figure 3.2.a). The instantaneous traction stresses and cell contours are shown every 28 s. Analysis of spatio-temporal patterns in the traction stresses and tension reveals different motility modes (for explanation see Figure 2.5). The modes observed are the S-S (stepping-stepping) and the G-G (gliding-gliding). The first and second letters correspond to the frontal and to the back adhesion respectively. (b) Average traction stress maps in the cell-based reference frame. The $\xi$ - and $\eta$ -axes coincide with the instantaneous principal cell axes and the origin is the cell centroid. Spatial coordinates are scaled with the instantaneous length of the major axis of each cell, $L(t)$ (Figure 2.4). Left column shows the average stress maps during the S-S (upper) and G-G (lower) motility modes. Details of how the cell-coordinate system used in these plots is constructed can be found elsewhere (29). The color maps indicate the magnitude of the total stresses in [pN/unit area], and the arrows indicate their direction. The white line contours show the average shape of the cells in this reference frame. The front (F) of the cell corresponds to $\xi > 0$ and the back (B) to $\xi < 0$. The second and third columns show the axial and lateral components of the traction stresses respectively. (c-i) Boxplots of the motility parameters corresponding to the S-S (blue), S-G (red) and G-G (green) motility modes, for N=8 wild-type cells. Each motility parameter is normalized with the mean value of the specific parameter during the whole time the cell is migrating. (c) Speed of migration ($V$). (d) Strain Energy ($U_s$). (e) Aspect ratio ($AR$). (f)Mode duration ($\Delta\tau$). Below each boxplot the number of modes N identified is indicated. (g) Axial force ($F_x$). (h) Lateral force ($F_y$). (i) Ratio of axial to lateral forces. Circles represent outliers, and the notched section of the boxplots shows the 95% confidence interval around the median. One and two asterisks denote statistically significant differences between the median of two distributions (<0.05 and <0.01 respectively).

### 4.4.4 Phase average stress pattern of *scrA*$^-$cells is similar to wild-type

The overall time evolutions of the stress patterns during the different phases of the motility cycle are similar for wild-type and *scrA*$^-$ cells except for the aforementioned reduced magnitude in *scrA*$^-$ cells (Figure 4.10.a). During all the phases of the motility cycle, the frontal traction forces in *scrA*$^-$ cells are more focused and intense than those at the rear, with a peak value closer to the cell center (Figure 4.10.c). In wild-type cells such a pattern is only observed during the protrusion phase (Figure 4.10.a, c). During relaxation, the forces are minimal in both cell lines and the cells spread out. The cells elongate during protrusion and exert higher forces of similar magnitude contracting their front and back. The frontal attachment region is closer to the centroid of the cell than the back, suggesting that the frontal part of the cell glides over the substrate during pseudopod extension. In wild-type cells, the magnitude of the traction forces peaks during contraction with the frontal attachment regions located closer to the leading edge of the cell, indicating formation of new adhesion regions. Similarly, stresses are also maximal during contraction in *scrA*$^-$ cells, although there is no shift of the peak stresses towards the front, suggesting a continuous forward shift of adhesion rather than an identifiable event of frontal attachment. During retraction, the peak stress at the back of the cell moves closer to the centroid, meaning that the back of the cell glides or slips forward in both wild-type and *scrA*$^-$ cells. There is also an asymmetry between the front and back due to the accumulation of mass in the front and the retraction of the rear part of the cell (Figure 4.10.a, c). Finally, no dissection into phases was done for *pirA*$^-$ cells since they do not exhibit a motility cycle.

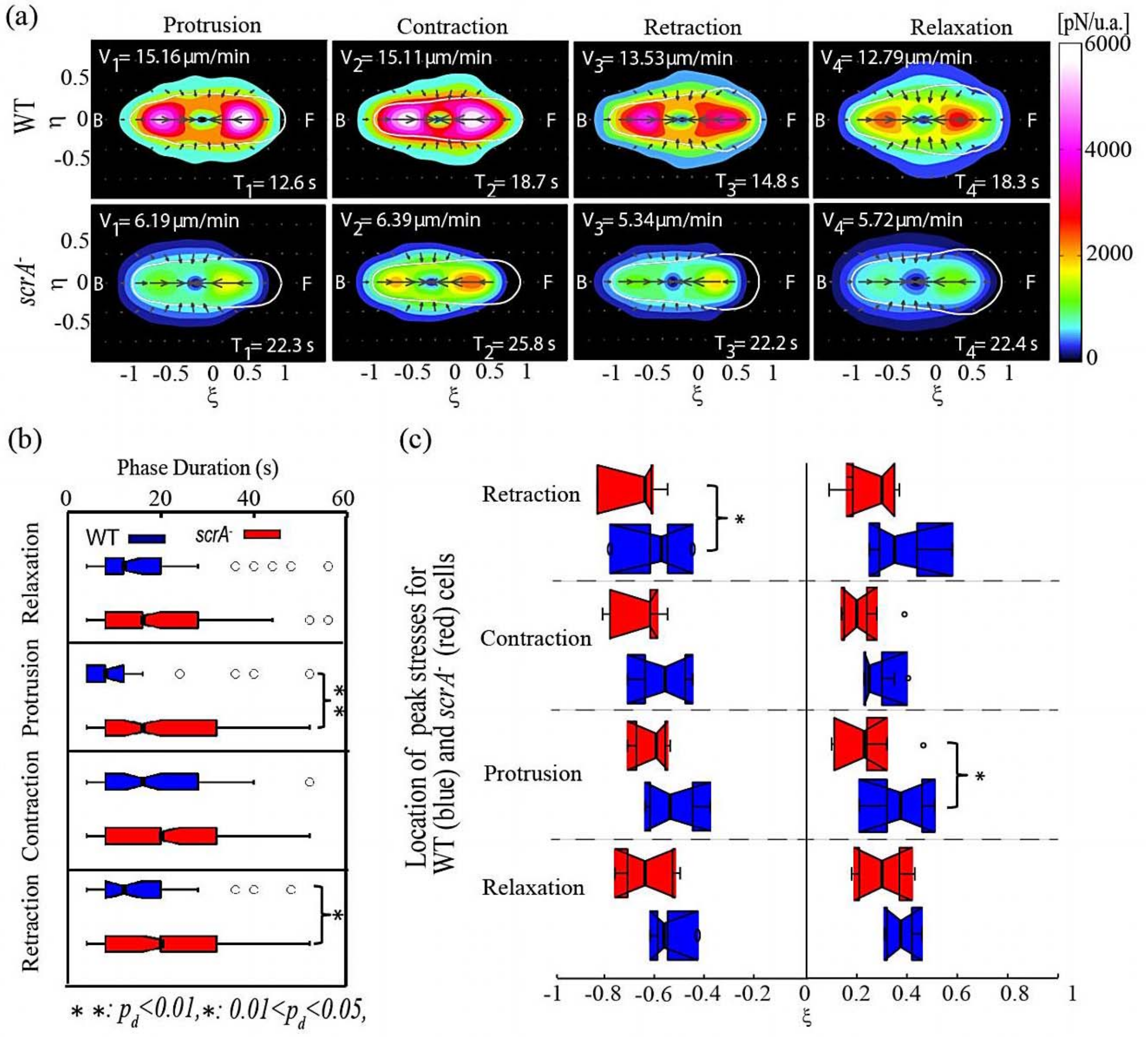

Figure 4.10: Phase-averaged stress maps of *scrA*$^-$ cells are similar to wild-type but strength of stresses is reduced and leading edge is not adhering. (a) Phase-averaged traction stress maps and cell shapes corresponding to the four phases of the motility cycle for wild-type (N = 14) and *scrA*$^-$ (N = 14) cells. The contour maps show the phase-averaged traction stress field computed in a reference frame rotated to have the $x$- and $y$-axes coincide with the instantaneous principal axes of the cells. All dimensions are scaled with the length of their instantaneous major axis, a. The colors indicate the magnitude of the stresses in pN/unit area, and the arrows indicate their direction. The white contours show the average shape of the cells in this reference frame. The front (F) of the cell corresponds to $\xi > 0$ and the back (B) to $\xi < 0$. The legends show the average durations, $T_1, \ldots, T_4$, and the corresponding average speeds during each phase, $V_1, \ldots, V_4$. (b) Boxplots of time duration of each of the four phases for wild-type (blue) and *scrA*$^-$ cells (red). Asterisks, significant differences between distributions: *, $0.01 < p_d < 0.05$; **, $p_d < 0.01$. (c) Boxplot showing the phase averaged location of the peak stresses at the front and back halves of the cell along the cell length calculated after integrating along the cell width, for wild-type (blue) and *scrA-* (red) cells. The peak stresses during protrusion are significantly closer to the cell centroid in *scrA-* cells than in wild-type, while the opposite happens during retraction.

## 4.5 Spatial and Temporal Control of Cellular Kinematics by F-actin in Chemotaxing Cells

The differences found in the traction stresses corroborate that regulated F-actin polymerization is critical to the generation of traction stresses required for the forward movement of the cells. But how the changes in the amount of F-actin of the different strains may relate to the average stresses observed is still unclear and difficult to assess. To examine this question, we quantified the changes in F-actin levels of cells in response to cAMP stimulation. Figure 4.2.e shows that, as previously described (66, 117), cells exhibit a biphasic curve with a sharp initial peak identified with the global cringe response at ~5 sec, and a shallower peak corresponding to pseudopod extension at 25-40 sec (120). The first peak was of comparable intensity for wild-type and *scrA*$^-$ cells and slightly reduced for *pirA*$^-$ cells. The decrease to basal levels occurred within 10 sec for wild-type and *pirA*$^-$ cells but took 20-30 sec for *scrA*$^-$ cells. Interestingly, *scrA*$^-$ cells exhibited a narrow second peak, whereas in *pirA*$^-$ cells, the second peak was extended. In spite of these differences, the results indicate that the mutant strains respond to cAMP effectively, and that actin nucleation is not exclusively regulated by SCAR/WAVE (66).

### 4.5.1. Cell length and frontal *Lifeact* fluorescence oscillate periodically and in phase for *scrA*$^-$ cells

To examine the spatiotemporal control of F-actin, we used the F-actin reporter *Lifeact,* a peptide derived from the F-actin binding protein Abp140 fused to GFP (121) to examine F-actin in vivo during chemotaxis. Joint analysis of the temporal evolution of the fluorescent intensity of *Lifeact* and cell length (Figure 4.11.a, c) revealed that these signals are coordinated for wild-type and *scrA*$^-$ but not *pirA*$^-$ cells. Figure 4.11.d shows the boxplots of the calculated time delays between the instantaneous cell length $L(t)$ and the instantaneous maximum fluorescence at the front $G_{max}(t)$ and

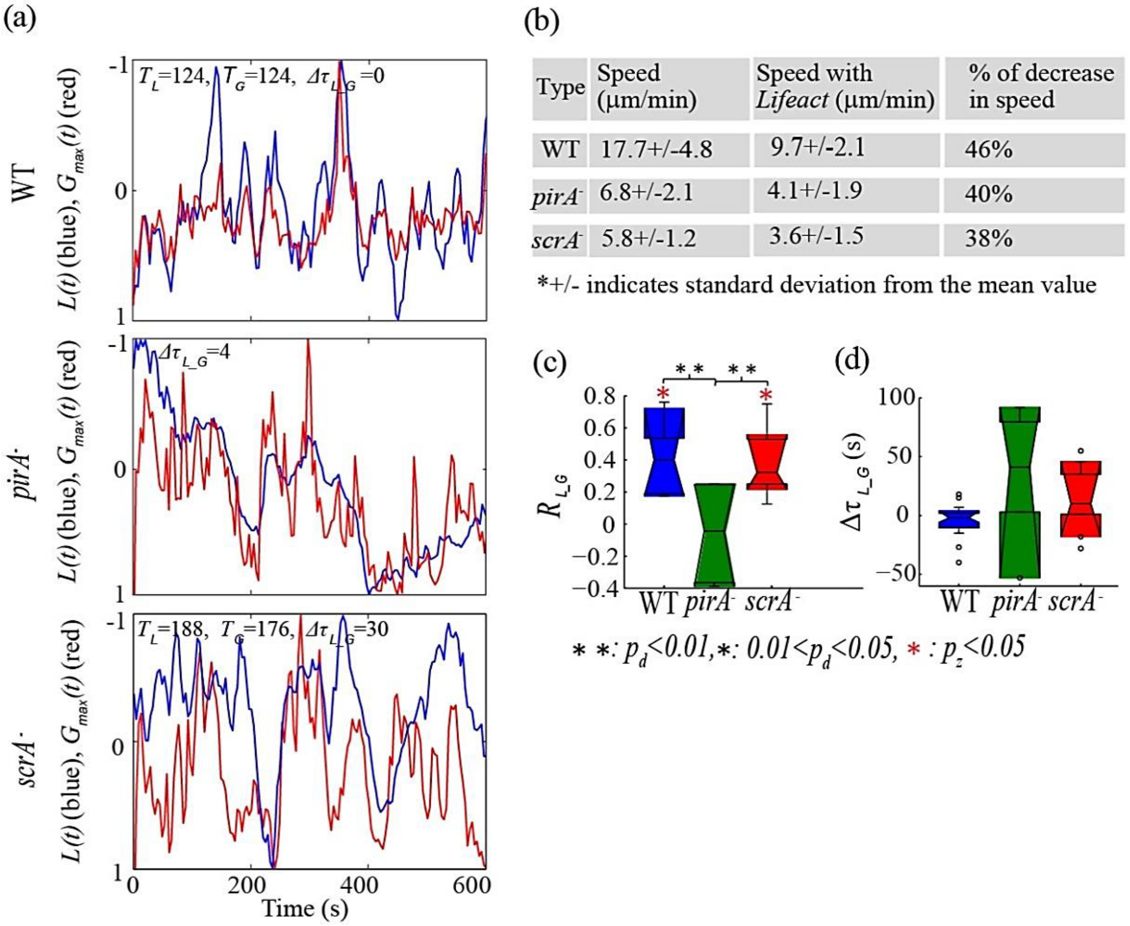

| Type | Speed (μm/min) | Speed with *Lifeact* (μm/min) | % of decrease in speed |
|---|---|---|---|
| WT | 17.7+/-4.8 | 9.7+/-2.1 | 46% |
| *pirA*- | 6.8+/-2.1 | 4.1+/-1.9 | 40% |
| *scrA*- | 5.8+/-1.2 | 3.6+/-1.5 | 38% |

*+/- indicates standard deviation from the mean value

Figure 4.11: Cell length and maximum *Lifeact* fluorescence intensity at the cell's front oscillate in time together for all cell lines. (a) Time evolution of the cell length *L(t)* (blue) and of the maximum *Lifeact* fluorescence intensity at the cell's front *Gmax(t)* (red) for a representative wild-type, *pirA*- and *scrA*- cell. Each plot also shows the periods determined through the time variation of the cell length $T_L$, and through the time variation of the frontal peak fluorescence $T_G$. Also shown is the time delay between the two records ($\Delta\tau_{L\_G}$ ). The time variation of the amplitude of each quantity is normalized between [-1 1]. (b) Table showing the average speed of migration $V$ of the different cell lines with and without *Lifeact* expression. Even though their migration speeds are reduced by approximately 40%, the mutant cells still migrate at much slower speeds (less than half of the wild-type speed). (c) Boxplots of the correlation coefficients between the cell length and the maximum frontal *Lifeact* fluorescence intensity of the cell ($R_{L\_G}$) for each cell line. Observe that in both wild-type and *scrA*- cells the correlation is significant while the two parameters are less correlated in *pirA*- cells. (d) Boxplots of the time delay ($\Delta\tau_{L\_G}$) between the above time records, where the cell length serves as the reference function. The above boxplots refer to wild-type (N = 9, blue), *pirA*- (N = 8, green), and *scrA*- (N = 9, red) cells. Black asterisks, significant differences between distributions: *, $0.01 < p_d < 0.05$, **, $p_d < 0.01$; red asterisks, a distribution with a median significantly different from zero: *, $p_z < 0.05$ (Wilcoxon signed rank test).

suggests that based on p-value tests all three lag distributions are not significantly different than zero. Figure 4.11.c displays the cross-correlation coefficients between the instantaneous cell length, $L(t)$, and the instantaneous maximum of the fluorescent signal in the cell front, $G_{max}(t)$, after correcting for the corresponding time delays. For wild-type and *scrA*$^-$ cells, these correlations are positive and significantly different than zero. On the other hand, *pirA*$^-$ cells show an insignificant correlation between $L(t)$ and $G(t)$, indicating that morphological changes and F-actin localization are not well coordinated in these cells. This is consistent with our finding that these cells do not undergo a synchronized, periodic motility cycle (Figure 4.4.d).

### 4.5.2 Phase average traction stress strength and frontal *Lifeact* fluorescence correlate for *scrA*$^-$ cells

We determined the period of the motility cycle of each cell expressing *Lifeact* from the time evolution of the cell length, $L(t)$, and dissected the cycle into phases using the algorithms described previously in Materials and Methods and Chapter 3. This allowed us to map F-actin localization in both space and time throughout the motility cycle (Figure 4.12.a, b). Figure 4.12.b illustrates the spatial distribution and intensity modulation of *Lifeact* during the four phases of the cycle. Both wild-type and *scrA*$^-$ cells show the highest frontal and back fluorescent intensity during contraction where the cell reaches its maximum length. Wild-type cells present moderate F-actin fluorescent localization during protrusion with a relatively high concentration at the front that is reduced during retraction and further lowered during relaxation. In contrast, *scrA*$^-$ cells present similar frontal fluorescent intensity during protrusion and retraction which is reduced only during relaxation. Although there is more intense fluorescent activity in the front for both wild-type and *scrA*$^-$ cells during protrusion and contraction, most of the F-actin is localized in a confined area, while the F-actin peak is more spread across the frontal edge of the cell, and its intensity is much lower in the preceding phases. In addition, we found that the fluorescence at the back of the cells is considerably lower than at the front and its intensity significantly increases during contraction, reaching values similar to the peak values at the front of the cell. The average fluorescence localization over multiple cycles indicates that *pirA*$^{-}$ cells have a localization similar to *scrA*$^{-}$ at the front, while at the back the intensity of both is slightly

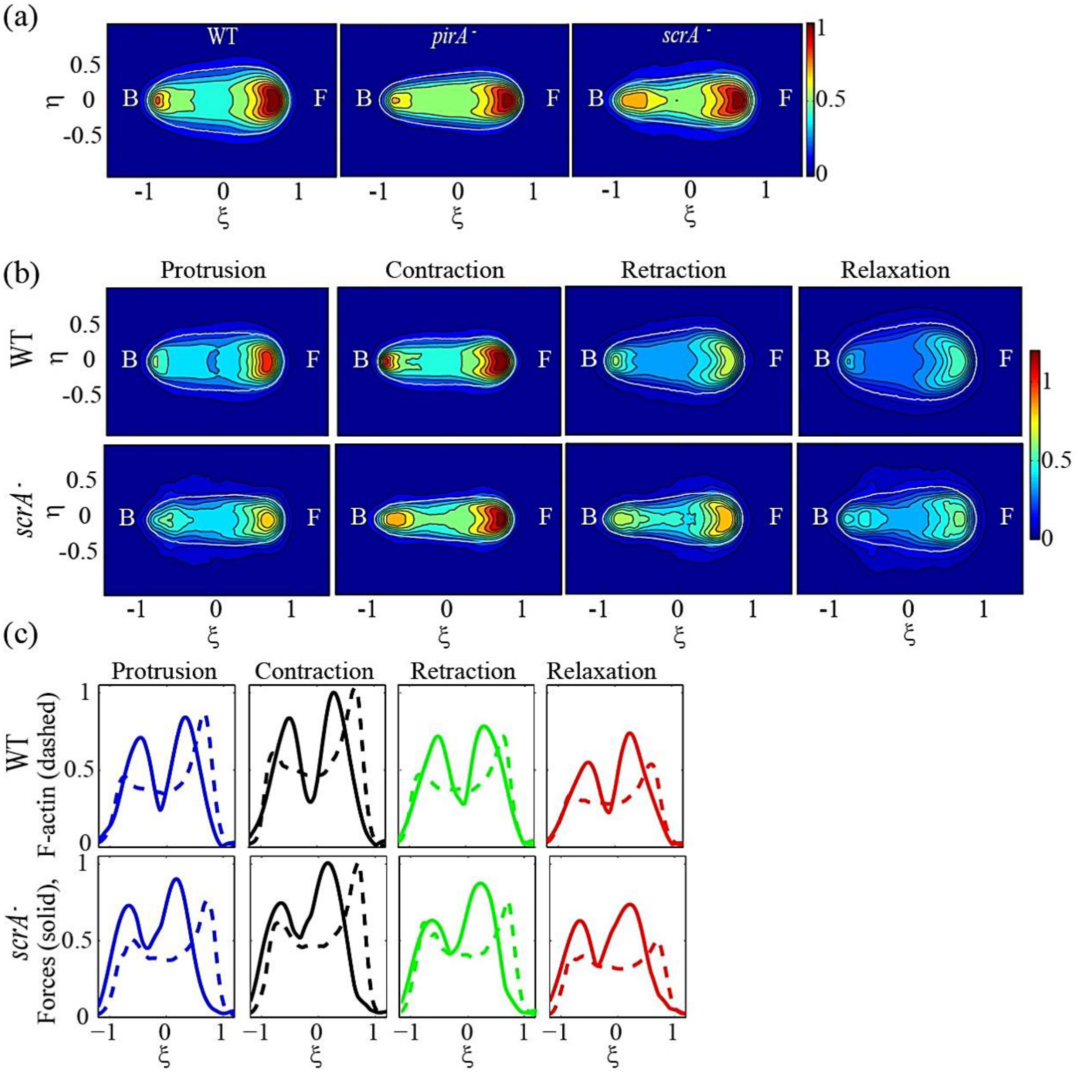

Figure 4.12: Strength of the phase-averaged traction stresses correlates with the maximum *Lifeact* fluorescence intensity at the cell's front for both wild-type and *scrA-* cells. (a) Average cell shape and localization of *Lifeact*, a reporter for F-actin, for wild-type (N = 9), *pirA*$^{-}$ (N = 8), and *scrA*$^{-}$ (N = 9) cells. The contour maps show the average fluorescence, computed in the same cell-based normalized reference frame as used in Figure 4.6.a. The colors indicate the intensity of *Lifeact*. The white contours show the average shape of the cells. The front (F) of the cell corresponds to x > 0 and the back (B) corresponds to x < 0. (B) Phase-averaged cell shape and localization of *Lifeact* during the four stereotypical phases of the motility cycle for wild-type (N = 9) and *scrA*$^{-}$ (N = 9) cells. (C) Phase-averaged values of the *Lifeact* fluorescence intensity (dashed line) and of the traction stresses (solid line) integrated along the width of the cell as a function of the position along the cell length for wild-type (N = 6) and *scrA*$^{-}$ (N = 4) cells. The intensity and force levels are normalized with their maximum value for each cell.

decreased compared to that in wild-type cells (Figure 4.12.a). Further, the aforementioned maps clearly depict that the maximum fluorescence for wild- type is confined to two very specific areas at the cell front and back while it is spread in broader areas for *pirA*$^-$ and *scrA*$^-$ cells (Figure 4.12a, b).

To further assess the variations of the F-actin concentration throughout the cell, we considered the integral of fluorescence across the centerline through the major axis of the cell, normalized with the integral of the mean fluorescent field in each cell (Figures 4.12c). This analysis confirms that the peaks of fluorescence intensity at the front and back of the cell are modulated up and down during the different phases (Figure 4.12.c). Wild-type cells present the peak value of fluorescence at the front during contraction that progressively decreases through protrusion, retraction and relaxation, while the localization of these intensity peaks at the front remain on average almost unchanged. On the contrary, *scrA*$^-$ cells show a build-up of F-actin at the front during protrusion that reaches a maximum during contraction and decreases during retraction to levels similar to those of the protrusion phase (Figure 4.12.b, c). During retraction and relaxation, the peak value in *scrA*$^-$ cells is also clearly displaced toward the cell centroid as compared to what is observed for wild-type cells. In accordance with Figure 4.12.b, it appears that for wild-type and *scrA*$^-$ cells, traction forces and fluorescent intensity are both modulated up and down during the different phases in a similar manner. Furthermore, Figure 4.12.b shows that for wild-type cells, the onset of the F-actin increase is located at the positions where we measure the peak force at the front and at the back of the cell. Similarly, the peak fluorescence at the front and back of the cell is located at the position where the absolute rate of change of the traction forces (first derivative) is maximum. *scrA*$^-$ cells, on the other hand, show an increase in the distance between the locations of the frontal force and fluorescent intensity peaks while the onset of F-actin increase at the front is located in between the position of the peak traction forces and the position of maximum absolute rate of change of the traction forces. We note that the location in the cells where the F-actin levels are highest (maximum fluorescence at the front) is at the position where the traction forces are almost zero, while peak force and peak fluorescence at the back colocalize. Figure 4.12.c also shows that, in the case of *scrA*$^-$ cells, both the peak force at the front and the minimum force in between the front and back are displaced towards the back of the cell. However, for wild-type cells, the point of minimal force exertion is located very near the centroid of the cell. While traction force is clearly displaced towards the cell centroid, the *Lifeact* fluorescence peak remains localized at the leading edge suggesting that *scrA*$^-$ cells have adherence defects (Figure 4.12.c).

## 4.6 Discussion

We measured the time evolution of cell length, traction forces, and strain energy (mechanical work) exerted by *two mutant* cell lines of the SCAR/WAVE complex (*pirA*$^-$ and *scrA*$^-$ cells), with high spatial and temporal resolution and investigated how actin polymerization contributes to the coordination of these quantities during chemotactic migration. By establishing a quantitative comparison between wild-type, *pirA*$^-$ and *scrA*$^-$ cells, we provide new insight into the role that actin polymerization plays in the conservation of the periodicity of cell migration as well as into the spatial and temporal regulation of the traction stresses and adhesion dynamics.

We found that the periodicity of the motility for *pirA*$^-$ cells is considerably reduced when compared to wild-type and *scrA*$^-$ cells. The dramatic disruption of the motility cycle underlines the specific role and importance of regulated actin polymerization at the cell front for the coordination of the motility cycle. For wild-type and *scrA*$^-$ cells, we found that the period $T$ of the oscillations in cell length and strain energy is inversely proportional to the average migration speed for those cell lines which have a clear motility cycle, in agreement with our previous findings (31). This correlation implies that the average migration velocity $V$ of a cell is determined by the frequency at which the cell can perform its motility cycle in a coordinated manner. However, we found that the step length (average distance travelled by the cells each cycle) of the mutants is shorter than for the wild-type, suggesting that actin dynamics play an important role in determining the step length. The observed differences suggest that the step length depends on the regulated dendritic actin polymerization and is therefore modulated by the efficiency of the dendritic polymerization process rather than the cell size.

Cells move by attaching and transmitting forces to the substrate on which they migrate through the formation of adhesion sites whose function is controlled by membrane proteins bound to the cytoskeletal F-actin filaments. Consistent with this notion, the F-actin content and cytoskeletal architecture appear to be key components in determining the magnitude of the traction stresses. Traction force cytometry allows us to compute the traction field produced by the cells during chemotactic migration. We found that for all cell lines under study, the time-averaged traction forces showed a contractile pattern consisting of the localized attachment of the cell at the front and back, while simultaneously contracting the substrate towards the cell's center (pole forces) (29). However, we also found that the strength of the pole forces is stronger in *pirA*$^-$ cells and weaker for *scrA*$^-$ when compared to wild-type cells. This result suggests that there is a correlation between the strength of the traction forces and the F-actin levels measured in the different cell lines, since the amount of F-actin present is higher in wild-type than in *pirA*$^-$ and lower in *scrA*$^-$ cells. Thus, it is the amount of F-actin present that is determining the strength of the applied to the substrate forces. Alternatively the difference may be due to the structure of the F-actin networks (more or less dendritic actin) rather than simply the amount of F-actin. Simultaneous phase average analysis of traction forces and *Lifeact* (a fluorescent marker for F-actin) show that the modulation of F-actin polymerization during the different phases of the motility cycle correlates with the modulation of the traction forces in chemotactic cells.

F-actin and its regulation also play an important role in maintaining the cell's overall geometry. While wild-type cells adopt an ellipsoidal shape with approximately the same area in the front and the back, we found that both *scrA*$^-$ and *pirA*$^-$ cells possess higher frontal areas while their frontal pole force is located further away from the cell's leading edge and closer to the centroid of the cell. There is evidence that the *scrA*$^-$ cells studied during cytokinesis produce numerous bulbous projections which do not contain actin and that are presumably driven by internal gradients of hydrostatic pressure. In addition, these cells often detach from the substrate during mitosis (119). In our investigation of chemotactic motility, we did not observe any blebs devoid of F-actin associated with membrane protrusion, and the peak fluorescence of the *Lifeact* marker remained localized close to the leading edge in wild type and mutant cells. This indicates that in both the *scrA*$^-$ and *pirA*$^-$ cells the displacement of the frontal pole force towards the centroid of the mutant cells is the result of gliding over the substrate. These pleiotropic effects suggest that the role of the proteins forming the SCAR/WAVE complex is not limited to the regulation of the dendritic actin polymerization but that this complex, or some of its components, may also be involved in other pathways potentially regulating the cell-substrate adhesion.

Our phase average analysis of the motility cycle for wild-type and *scrA*$^-$ cells revealed that the longer period observed in *scrA*$^-$ cells was due primarily to an increase in the duration of the protrusion phase and, to a lesser extent, an increase in the duration of retraction phase. The increase in the duration of these two phases indicates that misregulating actin polymerization primarily affects the duration of the phases where the cell is either increasing or decreasing its length. The increase in the duration of protrusion may result from lack of positive feedback from F-actin polymerization. This may also explain why the duration of the contraction and relaxation phases are only slightly prolonged since they do not require changes in F-actin levels. However, the reasons for an increase in the duration of the retraction phase is unclear. One possible explanation could be the effects of the misregulated actin dynamics on the coordination of the actomyosin contractile network.

The phase average analysis of traction forces revealed that the patterns of the average stresses during the different phases of the motility cycle are similar when comparing wild-type to *scrA*$^-$ cells. It was somewhat counterintuitive to observe that for *scrA*$^-$ cells, the frontal traction stresses are stronger relative to the back and are closer to the centroid of the cell for all the phases, a characteristic observed in wild-type cells only during the protrusion phase. This behavior indicated that the leading edge was constantly gliding and that *scrA*$^-$ cells presented reduced adhesion.

We confirmed the previously reported small, but important differences between the F-actin response of wild-type cells and SCAR/WAVE mutants when stimulated with cAMP suspension (66, 117). We also found relative changes in the localization of F-actin marker *Lifeact* between cell lines which confirmed that misregulation of the SCAR/WAVE complex directly affects F-actin polymerization activity. The relative timings of different mechanical variables were also affected. We found that for wild-type cells, there is no significant time delay between the temporal evolution of the cell length, the strain energy, and the maximum F-actin signals. However, *scrA*$^-$ cells showed a significant mean time delay between the cell length and the strain energy of 4 sec, while there was no time delay between the cell length and maximum F-actin at the front. In that case, actin polymerization occurs at the same time as cell lengthening, while force increase follows with a delay of 4 sec suggesting that *scrA*$^-$ cells are slower in generating forces. Moreover, the increase in the time delay between cell length and strain energy exerted by *scrA*$^-$ cells in the substrate indicates the importance of regulated actin polymerization for the maintenance of the precise timing of the various mechanical events occurring during migration. Although *scrA*$^-$ cells still move quasi-periodically, we observed that the mechanical events that drive motility are impaired compared to wild-type cells, as suggested by the increased duration of protrusion and retraction. We therefore conclude that the activity of the SCAR/WAVE complex is essential for the preservation of the timings of actin polymerization and of the various mechanical events driving the cell motility cycle. We suspect that actin turnover may play a role in the determination of the duration of the phases of the cycle, and that it may act as an internal clock regulating the relative timings of events during chemotaxis.

Finally, by constructing and inspecting the traction tension kymographs of both mutants for a number of cells, we concuded that *scrA*$^-$ cells only implement the *Stepping-Stepping* motility mode while *pirA*$^-$ cells alternate between the *Stepping-Stepping* and the *Stepping-Gliding* motility modes. It is interesting that both mutants maintain their back adhesion stationary. In wild-type cells, the sliding of the back adhesion is associated with an increase in the migration speed (S-G mode). This finding suggests that the migration speed may control which motility mode the cell will follow.

Further analysis with better spatial and temporal resolutions are required to elucidate these aspects of motility, and the variables that control the succession of the various mechanical events. In addition, future studies of actin related proteins that affect stabilization, crosslinking, and turnover of

F-actin filaments will help us to better understand the precise role of regulated F-actin polymerization in regulating the mechanics of cell migration.

Chapter 4 has been published in part in the Molecular Biology of the Cell journal. The SCAR/WAVE complex is necessary for proper regulation of traction stresses during amoeboid motility. Bastounis E., Alonso-Latorre B., Meili R., del Álamo J.C., Lasheras J.C., Firtel R.

# Chapter 5
# Cytoskeletal Crosslinking Defects Impair Axial Contractility [†]

In the previous chapters, we showed that an important factor controlling the efficiency of migration is the spatiotemporal coordination of traction forces and adhesion dynamics. In this chapter, to further investigate the role of contractility and adhesion dynamics in regulating motility, we will examine two strains with cytoskeletal crosslinking defects: Myosin heavy chain (MyoII) null cells (*mhcA*$^-$) and filamin (Abp120) null cells (*abp120*$^-$).

The mechanics of migration of *mhcA*$^-$ cells, which lack both Myosin II cross-linking and motor function, have been to a certain degree studied previously (31, 122). Unlike the wild type, they exert increased lateral stresses that may be partially due to defects in F-actin crosslinking resulting in less rigid cells that are unable to develop axial contractility (31, 122). This suggests that the architecture of the actin polymer network is crucial in determining the cell speed through the effect it has on the mechanical properties of the cell (stiffness) (123). On the other hand, Filamin A is known to crosslink the F-actin network in an orthogonal fashion and to be the most efficient cross-linking protein in vitro (72, 124). *Dictyostelium* cells null for filamin, similar to *mhcA*$^-$ cells, are known to have decreased elastic moduli and deeply reduced speed (70, 123, 124)

---

[†] Chapter 5 is being prepared in part for publication. Chemotaxing amoeboid cells migrate by switching between distinct modes of adhesion dynamics and contractility. Bastounis E., Meili R., Alvarez-Gonzalez B., del Álamo J.C., Lasheras J.C., Firtel R.

## 5.1 Cytoskeletal Crosslinking Defects Impair Axial Contractility but Such Cells Still Move Using Motility Modes that Rely on Periodic Lateral Contractions

As indicated in the previous chapters, the spatiotemporal coordination of traction forces plays an important role in establishing different motility modes during migration. To further understand this coordination, we examined two strains with cytoskeletal crosslinking defects that may affect the spatiotemporal coordination of the traction stresses and adhesion dynamics: myosin heavy chain (MyoII) null cells ($mhcA^{-}$) and filamin (Abp120) null cells ($abp120^{-}$).

### 5.1.1 $mhcA^{-}$ cells exert stresses peripherally and form a gliding front adhesion

In agreement with previous studies, we found that $mhcA^{-}$ cells move following a motility cycle but with a much lower migration speed than wild-type cells. Moreover, they have increased lateral contractility, but no major differences in their average length, aspect ratio, or strain energy (Figure 5.1.a-f) (31, 123). Although the magnitude of the traction stresses is not substantially different from wild-type cells, we found that the axial contractility of $mhcA^{-}$ cells is decreased by 21% whereas the lateral contractility is increased by 26% (Figure 5.1.d-f). These findings confirm that the architecture of the F-actin network and/or the motor activity of MyoII are essential to the cell's ability to develop axial contractility, as reported previously (31, 125).

Using the mode sorting algorithm introduced above, we found that $mhcA^{-}$ cells move exclusively by switching between the G-S and G-G modes, suggesting that the lack of contractile MyoII pushes cells to use modes that we seldom observe in wild-type cells migrating on collagen substrates (Figure 5.2.a). The front adhesion of $mhcA^{-}$ cells is always gliding forward whereas the back either glides or remains stationary. We found that the velocity of migration in the G-S mode is lower than in the G-G mode (Figure 5.2.c).

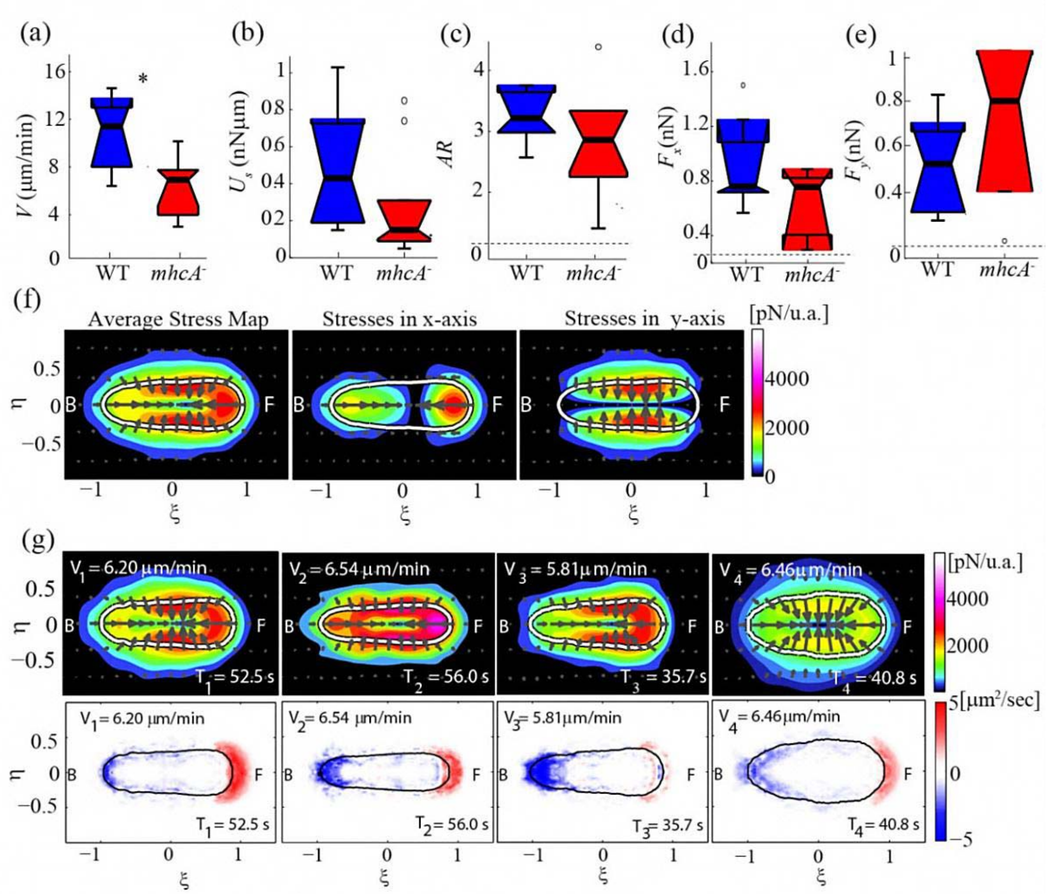

Figure 5.1: Boxplots of motility parameters for N=10 wild-type (blue) and N=8 *mhcA*$^-$ cells (red) . (a) Speed of migration ($V$). (b) Strain Energy ($U_s$). (c) Aspect ratio ($AR$). (d) Axial force ($F_x$). (e) Lateral force ($F_y$). (f) Average stress maps in cell based coordinates (see Figure 2.3). First column shows the average stress distribution pattern for the N=8 *mhcA*$^-$ cells. The second and third columns show the axial and lateral component of the stresses respectively.(g) Phase-averaged traction stress maps and cell shapes corresponding to the four phases of the motility cycle for N=8 *mhcA*$^-$ (for description of the contour maps see Figure 3.8). The legends show the average durations, $T_1, \ldots, T_4$, and the corresponding average speeds during each phase, $V_1, \ldots, V_4$. Second row shows the phase-averaged area fluxes and cell shape corresponding to the four stereotypical stages for the same cell line. The colors indicate the magnitude of the area fluxes in $\mu m^2/s$ (red: positive area flux or gain of cell area; blue: negative area flux or loss of cell area).

The average stress maps also suggest that the shape of the cell is less polarized during the G-G mode, and at the same time, is applying increased lateral stresses all along its periphery (Figure 5.2.b). In contrast, the cell's shape is more polarized during the G-S when the lateral stresses are confined to a region near the centroid of the cell (Figure 5.2.b). Inspection of the tension kymographs for *mhcA*$^-$ cells also suggests that when the back adhesion reaches the back edge of the cell, its strength increases, and the cell is always in a G-S mode (Figure 5.2.a), consistent with its inability to detach the rear by contraction. We observed no significant differences in the rest of the motility parameters analyzed for these two modes (Figure 5.2.d-i). The mean time duration of both modes was ~200 s (Figure 5.2.f).

Table 5.1: Summary and comparison of average motility parameters for wild-type (N=10) and *mhcA*$^-$ cells (N=8). The parameters shown include the averages of speed of migration ($V$); aspect ratio ($AR$); cell length ($L$); strain energy ($U_s$); axial force ($F_x$); lateral force ($F_y$). Red colored numbers indicate the percentage increase (+) or decrease (-) of $F_x$ and $F_y$ with respect to control.

| Cell Type | $V$ (μm/min) | $AR$ | $L$ (μm) | $U_s$ (nNμm) | $F_x$ (nN)+%incr | $F_y$ (nN)+%incr |
|---|---|---|---|---|---|---|
| Wild-type | 11.10 | 3.39 | 28.3 | 0.51 | 0.92 | 0.53 |
| *mhcA*$^-$ | 6.26 | 3.07 | 28.0 | 0.29 | 0.72-21% | 0.67+26% |

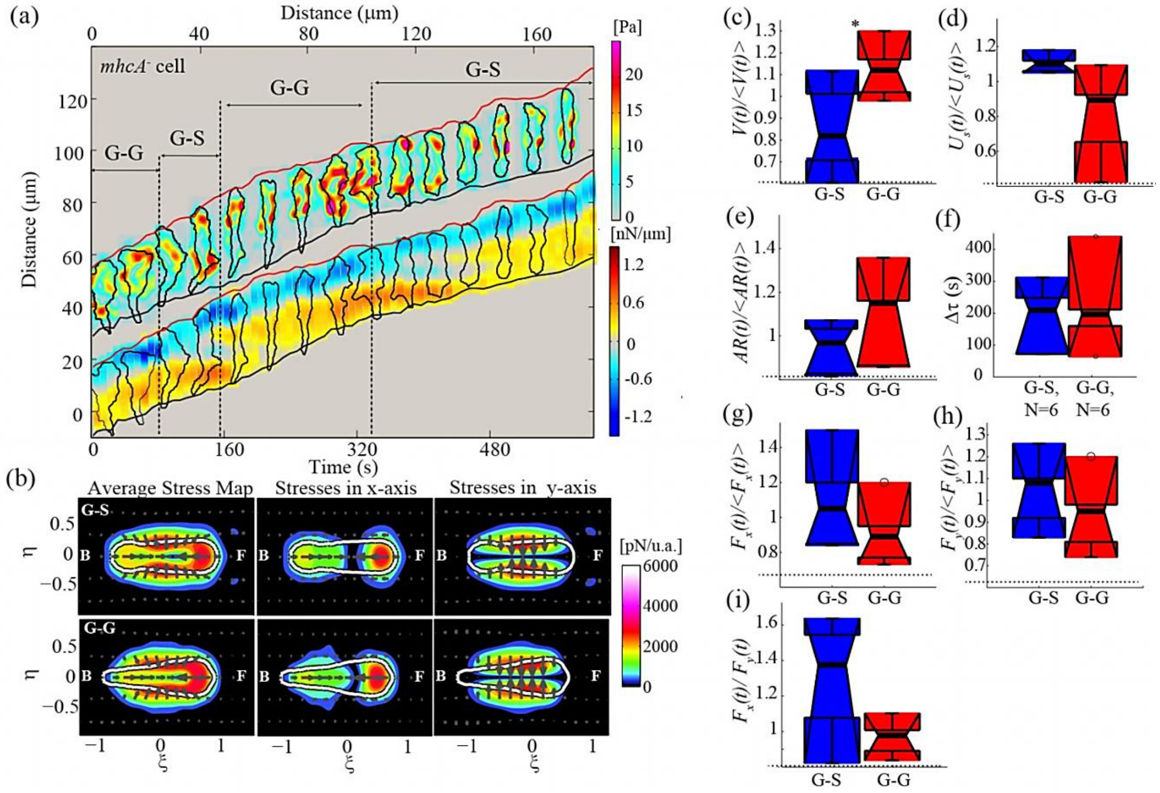

Figure 5.2: Spatio-temporal dynamics and statistics of motility modes in *mhcA*$^-$ cells. (a) Kymograph of traction stresses $\tau(x,y)$ (upper part) and tension $T(x,t)$ (lower part) for a representative *mhcA*$^-$ cell, showing that the cell implements the G-S and G-G modes. (b) Average stress maps in cell-based coordinates during G-S (upper row) and G-G (lower row) motility modes. (c-i) Boxplots of the motility parameters corresponding to the G-S (blue) and G-G (red) motility modes for N=5 *mhcA*$^-$ cells, similar to Figure3.6.a-g.

### 5.1.2. *abp120⁻* cells move extremely slowly and exert very low stresses with the lateral component higher than the axial

We used cells lacking the F-actin cross-linker filamin (Abp120) to investigate the role that F-actin crosslinking at the leading edge may play in controlling the ability of the cell to develop axial tension. Filamin null (*abp120⁻*) cells polymerize F-actin but are unable to properly cross-link it at the leading edge. Thus, they are defective in protruding the frontal pseudopod (71, 74, 126); accordingly, *abp120⁻* cells exhibit poor cortical F-actin localization at the front of the cells (Figure 5.3.a).

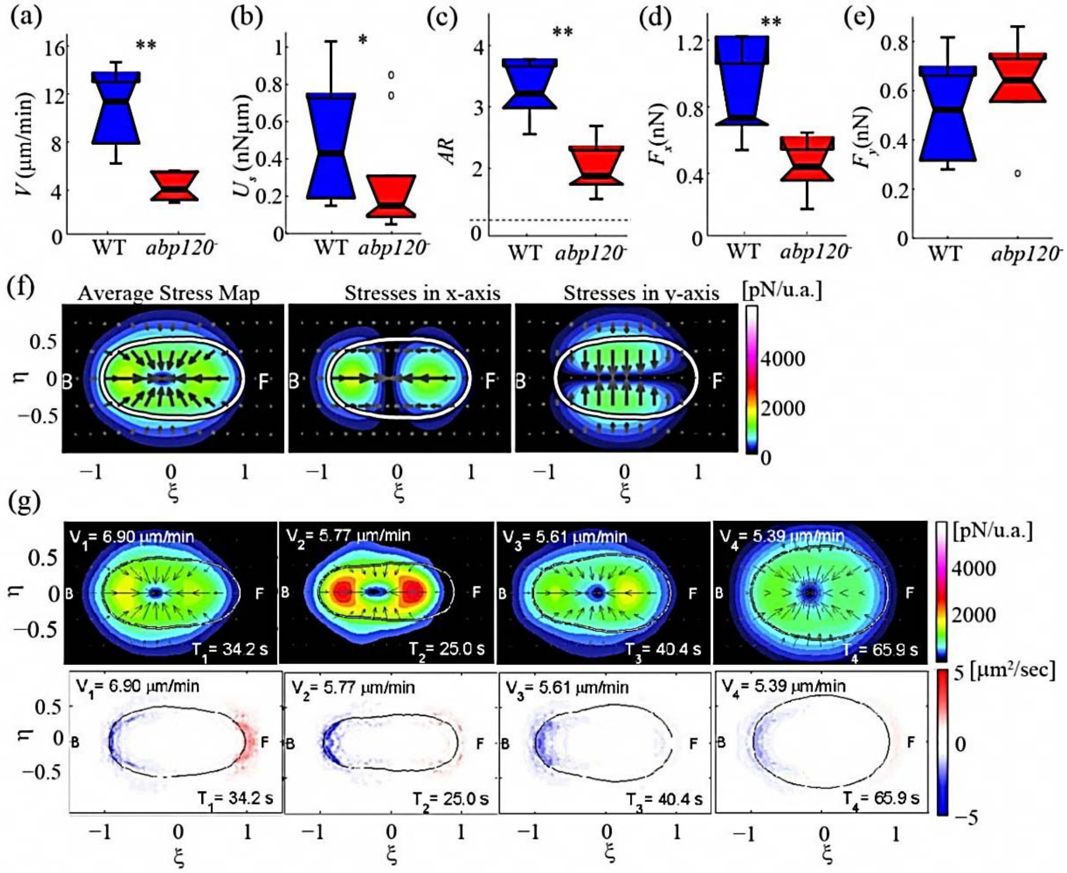

Figure 5.3: Boxplots of motility parameters for N=10 wild-type (blue) and N=9 *abp120⁻* cells (red). (a) Speed of migration ($V$). (b) Strain Energy ($U_s$). (c) Aspect ratio ($AR$). (d) Axial force ($F_x$). (e) Lateral force ($F_y$). (f) Average stress maps in cell based coordinates (see Figure 2.3). First column shows the average stress distribution pattern for the N=9 *abp120⁻* cells. The second and third columns show the axial and lateral component of the stresses respectively.(g) Phase-averaged traction stress maps and cell shapes corresponding to the four phases of the motility cycle for N=9 *abp120⁻* cells. Second row shows the phase-averaged area fluxes and cell shape corresponding to the four stereotypical stages for the same cell line (for further description see Figure 5.1).

We found that *abp120*$^-$ cells have greatly reduced speed (<50% that of wild-type cells), a smaller aspect ratio and cell length, and lower strain energy (Figure 5.3.h, i and Table 5.2). Consistent with the reduction in strain energy, we found that the overall traction stresses in these cells are much lower than those of wild-type cells (Figure 5.4.j-k and Table 5.2). However, this strain map shows a slightly stronger lateral squeezing (~18% higher than wild-type cells) while exerting axial tensions that are almost 50% lower (Figure 5.4.j and Figure 5.3.j-k).

Table 5.2: Summary and comparison of the average motility parameters for wild-type (N=10) and *abp120*$^-$ (N=9) cells (see Table 5.1).

| Cell Type | $V$ (μm/min) | $AR$ | $L$ (μm) | $U_s$ (nNμm) | $F_x$ (nN)+%incr | $F_y$ (nN)+%incr |
|---|---|---|---|---|---|---|
| Wild-type | 11.10 | 3.39 | 28.3 | 0.51 | 0.92 | 0.53 |
| *abp120*$^-$ | 4.31 | 2.00 | 17.3 | 0.29 | 0.46-50% | 0.63+18% |

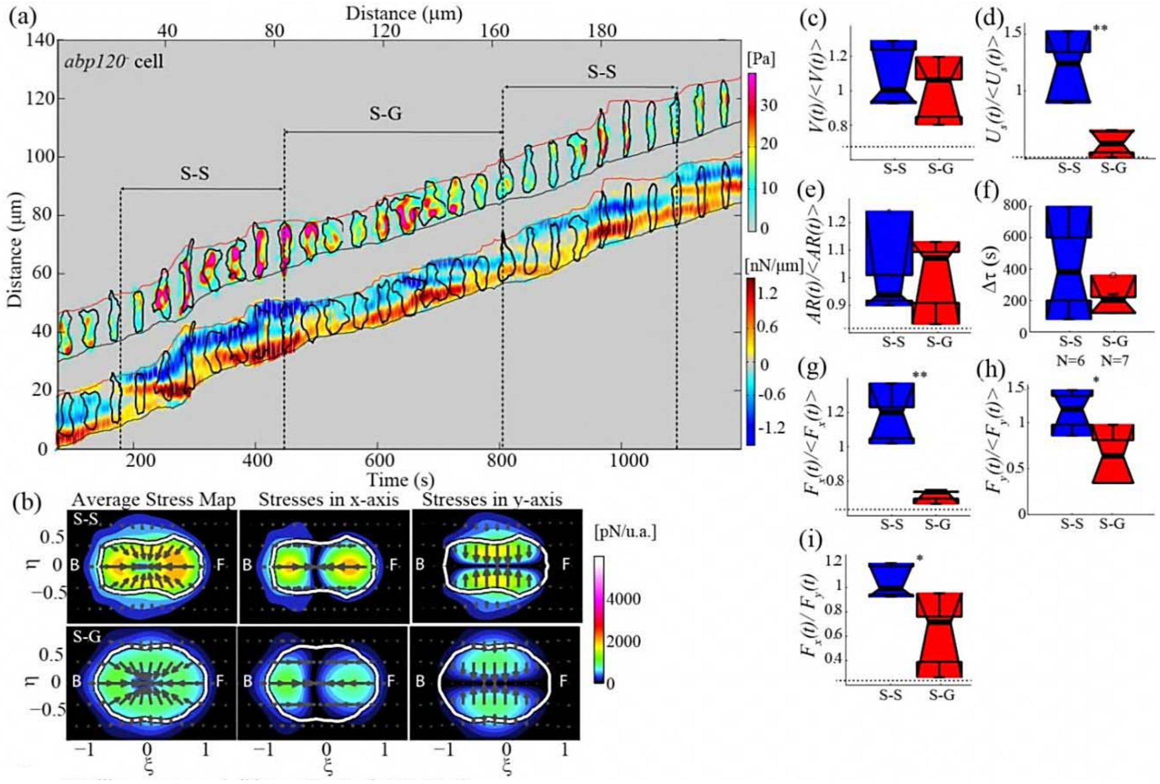

Figure 5.4: Spatio-temporal dynamics and statistics of motility modes in *abp120*$^-$ cells. (a) Kymograph of traction stresses $\tau(x,y)$ (upper part) and tension $T(x,t)$ (lower part) for a representative *abp120*$^-$ cell, showing that the cell implements the S-S and S-G modes, similar to wild type. (b) Average stress maps in cell-based coordinates during S-S (upper row) and S-G (lower row) motility modes. (c-i) Boxplots of the motility parameters corresponding to the S-S (blue) and S-G (red) motility modes for N=6 *abp120*$^-$ cells, similar to Figure3.6 .a-g.

### 5.1.3 *abp120$^-$* cells follow a well-defined motility cycle

We also found that *abp120$^-$* cells show a high degree of periodicity in the time variation of their strain energy and cell length (Figure 5.5.b-c). The stress kymograph in Figure 5.3.a illustrates that *abp120$^-$* cells alternate between phases of roundness followed by periodic elongations, which are produced by lateral contractions (Figure 5.3.a). Thus, their motility cycle is controlled by the frequency of lateral squeezing that produces periodic oscillations of roundness and elongations rather than by axial contractions. Consistent with that, splitting the motility cycle into phases and calculating the phase-averaged traction stresses reveal that they retain the phase characteristics of wild type, with the exception that they exert much higher lateral stresses.

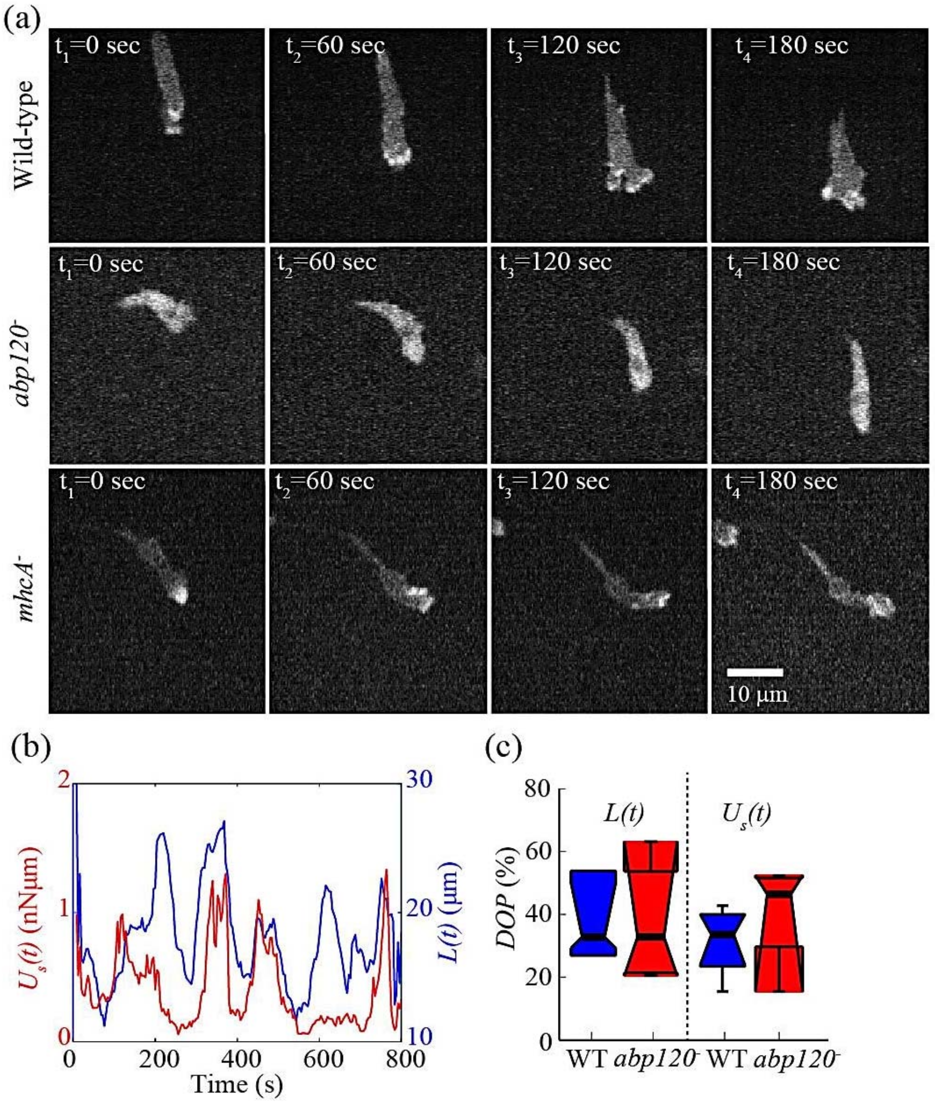

Figure 5.5: *abp120*$^{-}$ cells undergo a motility cycle when chemotaxing but without showing any F-actin localization. (a) Snapshots of a representative wild type (first row), *abp120*$^{-}$ (middle row) and *mhcA*$^{-}$ cell (third row) expressing *lifeact*-GFP, showing that the *abp120*$^{-}$ cell shows no apparent F-actin localization. (b) Cell length, $L(t)$ (blue) and strain energy, $U_s(t)$ (red) oscillations over time for an *abp120*$^{-}$ representative cell. Notice that both oscillate periodically. (c) Characterization of the DOP of $L(t)$ and $U_s(t)$ for N=10 wild-type cells and N=9 *abp120*$^{-}$ cells.

### 5.1.4 *abp120*$^{-}$ cells alternate between the same motility modes as wild-type cells

To further investigate the motility of *abp120*$^{-}$ cells, we split motility into modes applying our analytical sorting tool and found that during movement, *abp120*$^{-}$ cells switch between the S-S and S-G modes, in a manner similar to wild-type (Figure 5.3.a and Figure 2.5.g-h). This suggests that although the lateral stresses of *abp120*$^-$ cells increase similarly to those of *mhcA*$^-$ cells, the motility modes of these two cell lines, which both exhibit crosslinking defects, are completely different. Unlike *mhcA*$^-$ cells, yet similar to wild-type, the front adhesion of *abp120*$^-$ cells is always stationary, while the back adhesion is either stationary (S-S) or gliding (S-G). However, we found no significant differences in the migration speed and aspect ratio between these two modes (Figure 5.3.c, d). We did, however, find a significant increase in strain energy when switching from the S-G to the S-S mode that was primarily due to the increase in the axial stresses (Figure 5.3.d, g-h). This is consistent with the ratio of axial to lateral stresses being significantly reduced in the S-G mode, where the lateral stresses become more important (Figure 5.3.b, i). As a result, during the S-G mode, the back edge of the *abp120*$^-$ cell moves forward almost continuously, whereas the speed of the frontal edge oscillates in phase with the modulated lateral squeezing. Finally, we did not find significant differences in the mean time duration of these two modes (Figure 5.3.f). The above findings suggest that, as a result of ineffective cytoskeletal crosslinking, the cells cannot effectively implement a motility cycle driven by axial contractions and must rely on lateral squeezing for their motion.

### 5.1.4 *roco2*$^-$ cells have similar motility phenotype to *abp120*$^-$ cells

We observed a similar stress phenotype in those cells lacking Roco2 (*roco2*$^-$ cells), a (LRRK2)-related Roco kinase that binds to and lies upstream from filamin in controlling cell polarization and chemotaxis (Figure 5.6) (74). This finding supports the model that Roco2 is a regulator of filamin (74). The traction tension kymographs of *Roco2*$^-$ cells and their motility phenotype are similar to those of *abp120*$^-$ cells, with the exception that the former move slightly faster, and their traction stresses are stronger (Figure 5.7 and Table 5.3).

Table 5.3: Summary and comparison of the average motility parameters for wild-type (N=10) and *roco2*$^-$ (N=5) cells (see Table 5.1).

| Cell Type | $V$ (µm/min) | $AR$ | $L$ (µm) | $U_s$ (nNµm) | $F_x$ (nN)+%incr | $F_y$ (nN)+%incr |
|---|---|---|---|---|---|---|
| Wild-type | 11.10 | 3.39 | 28.3 | 0.51 | 0.92 | 0.53 |
| *roco2*$^-$ | 7.10 | 2.34 | 18.6 | 0.40 | 0.76-17% | 0.60+13% |

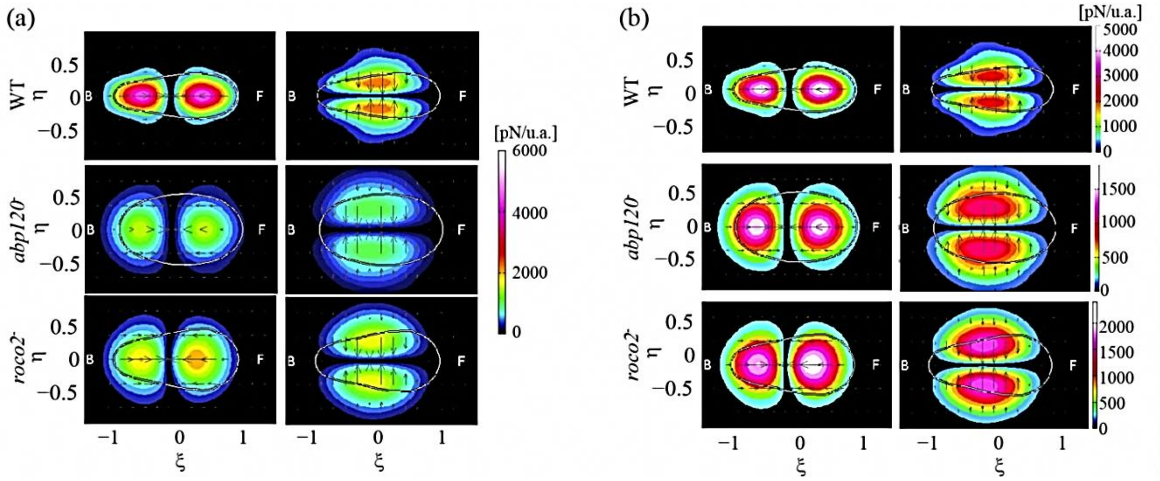

Figure 5.6: Average traction stress maps reveal similar force distribution in *abp120⁻* and *roco2⁻* cells, characterized by increased lateral contractility. (a) Axial (first row) and lateral (second row) components of the average stress maps for N=14 wild-type cells, N=9 *abp120⁻* cells and N=6 *roco2⁻* cells. Details of how the cell-coordinate system used in these plots is constructed can be found elsewhere (29). The color maps indicate the magnitude of the total stresses in [pN/unit area], and the arrows indicate their direction. The white line contours show the average shape of the cells in this reference frame. The front (F) of the cell corresponds to $\xi > 0$ and the back (B) to $\xi < 0$. The second and third columns show the axial and lateral components of the traction stresses respectively. The stresses are shown using the same color map for all cell lines whereas in (b) the color map for each cell line is normalized by the maximum value of the traction stresses in each cell line.

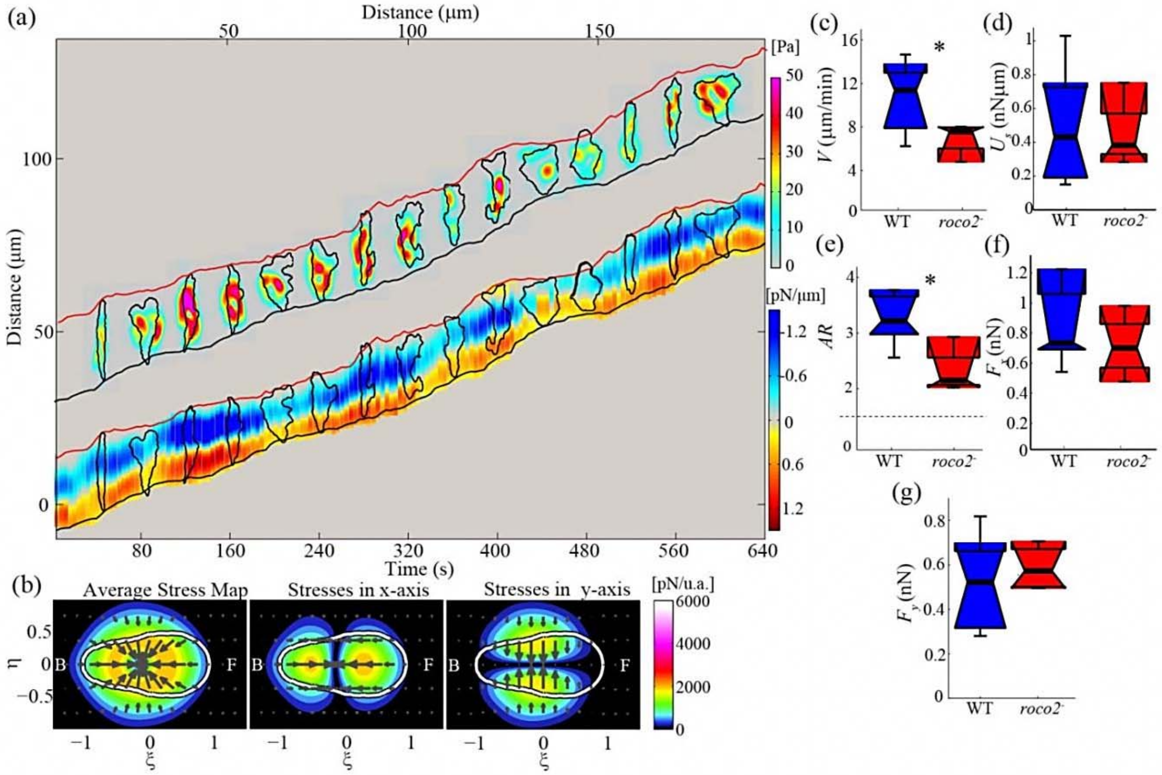

Figure 5.7: Spatio-temporal dynamics and statistics of motility in *roco2*$^-$ cells. (a) Kymographs of traction stresses *τ(x,y)* (upper part) and traction tension *T(x,t)* (lower part) for a representative *roco2*$^-$ cell. (b) Same as Figure 5.3.f for the *roco2*$^-$ cell shown in panel (a). (c-g) Same as Figure 5.3.a-e for N=10 wild type (blue) and N=5 *roco2*$^-$ cells (red).

## 5.2 Discussion

Our analysis of two mutant strains that lack distinct F-actin crosslinkers supports a key role for lateral contractions in amoeboid cell motility. We have shown that, compared to wild-type cells, *mhcA*$^-$ cells exert increased lateral stresses. This may be partially due to defects in F-actin crosslinking that result in cells unable to develop axial contractility (31, 77, 127). This observation confirms the idea that the architecture of the F-actin polymer network is crucial to the dynamics of cell motility. By analyzing *mhcA*$^-$ cells migrating on elastic substrata, we found that these cells move by developing an axial contractility similar to that of wild-type cells while also exerting periodic lateral contractions.

Unlike wild-type cells, we found that the front adhesions of *mhcA*$^-$ cells are always gliding forward, whereas the back adhesions are either stationary (G-S) or gliding (G-G). We found that *mhcA*$^-$ cells placed on substrates of increased adhesiveness are unable to migrate. This is consistent with previous studies performed on glass substrates that demonstrated the importance of increased actin-myosin contractility when the adhesiveness of the substrate increases (80).

We also found that cells lacking Filamin A (abp120), an orthogonal F-actin crosslinker that localizes to the leading-edge F-actin network and is required for pseudopod protrusion, have a significantly reduced speed and move by using enhanced lateral contractility (70, 72, 128). Unlike *mhcA*$^-$ cells, which constantly contract laterally using many adhesion sites located at the cell's periphery, *abp120*$^-$ and *roco2*$^-$ cells, which lack an effective pseudopod, move by establishing two adhesion areas and by periodically switching from a mode in which they contract axially to a mode in which they contract laterally. This observation suggests a new mechanism by which cells can move. Although we do not know the precise biochemical reasons for the difference between *mhcA*$^-$ and *abp120*$^-$ cells, we expect that some of the differences may be due to the motor function of MyoII present in *abp120*$^-$ cells, and that Abp120 may function primarily in the front of cells. It is clear that defects in cytoskeletal crosslinking give rise to ineffective axial contractility and migration that relies on lateral contractions, resulting in a significantly reduced migration speed.

In conclusion, in this chapter we have demonstrated a critical role for lateral contractility in driving cell migration in mutant cells lacking essential cytoskeletal crosslinkers (*mhcA*$^-$ and *abp120*$^-$).

Chapter 5 is being prepared in part for publication. Chemotaxing amoeboid cells migrate by switching between distinct modes of adhesion dynamics and contractility. Bastounis E., Meili R., Alvarez-Gonzalez B., del Álamo J.C., Lasheras J.C., Firtel R.

# Chapter 6

# Mechanics of Amoeboid Cell Migration on Substrates of Varying Stiffness and Adhesivity †

In the previous chapters, we investigated the role of dendritic actin polymerization at the frontal cell edge and of proper F-actin crosslinking in the mechanics of cell migration, by comparing the motility phenotype of wild-type cells with a number of mutant cell lines. In the current chapter, we are examining another important factor controlling the efficiency of migration, namely the mechanical properties of the substrate on which cells migrate.

Cell migration of anchorage-dependent cells depends on both chemical and mechanical interactions (129). Various cells following a chemoattractant gradient are known to adjust their morphology and migration speed in response to environmental factors including substrate stiffness and adhesiveness (101, 102, 130, 131). The mechanisms underlying cell-substrate adhesion and their role in the locomotion efficiency have been investigated in fibroblasts, keratocytes, and other eukaryotic cells that attach to the substrate via discrete and localized focal adhesions (83, 132). Unlike fibroblasts, *Dictyostelium* and other amoeboid cells do not form localized focal adhesions, but rather attach to the substrate via more diffuse areas (38, 84, 85). The composition and structure of these adhesions is less well understood in molecular terms. More importantly, the high speed of these cells means that they undergo much quicker assembly and disassembly of adhesions, which renders them challenging to study. For these two classes of motile cells, little is known about how key biochemical

---

† Chapter 6 is being prepared in part for publication. Chemotaxing amoeboid cells migrate by switching between distinct modes of adhesion dynamics and contractility. Bastounis E., Meili R., Alvarez-Gonzalez B., del Álamo J.C., Lasheras J.C., Firtel R.

processes coordinate the formation and breakage of adhesions with the generation of traction stresses to control movement.

Although extensive studies have been made on the responses of *Dictyostelium* to chemical cues, little is known about the effect of the mechanics of the substrate on the migration and adhesion of the cells. To address this question and to gain more insight into the role of cell-substrate adhesions in cell migration, we have analyzed the mechanics of migration of wild-type cells chemotaxing on adhesive (poly-L-Lys treated) substrates as well as on substrates of increased stiffness. We then compared the motility phenotype of these cells with that of cells migrating on standard collagen substrates. Thus, the present study examines the coordinated dynamics of substrate adhesions and traction stress generation by which fast-moving, amoeboid cells adjust their migration.

## 6.1 Migration on Highly Adhesive Substrates Requires Lateral as well as Axial Contractions

As indicated in the previous chapters, the spatiotemporal coordination of traction forces and adhesion dynamics plays an important role in establishing different motility modes during migration. To further understand this coordination and to assess the role that the strength of the adhesions and the dynamics of their assembly and disassembly play in the migration process, we examined the movement of cells chemotaxing on substrates coated with collagen plus poly-L-Lys. Poly-L-Lys, is a polycation that when used for coating, enhances the electrostatic interaction between the negatively charged cell membrane and the positively charged substrate, thus increasing cell adherence (80).

### 6.1.1 Wild-type cells chemotaxing on adhesive substrates implement completely different motility modes

When plated on a substrates coated with collagen plus poly-L-Lys (20mg/ml), the wild-type cells initially round up and contract uniformly inward, as can be seen by the build-up of traction stress and tension (Figure 6.1.a-b). In a chemoattractant gradient on this type of substrate, the cells exhibit two main motility modes, but only one of them seems derived from the modes observed on collagen only substrates (Figure 6.1.a).

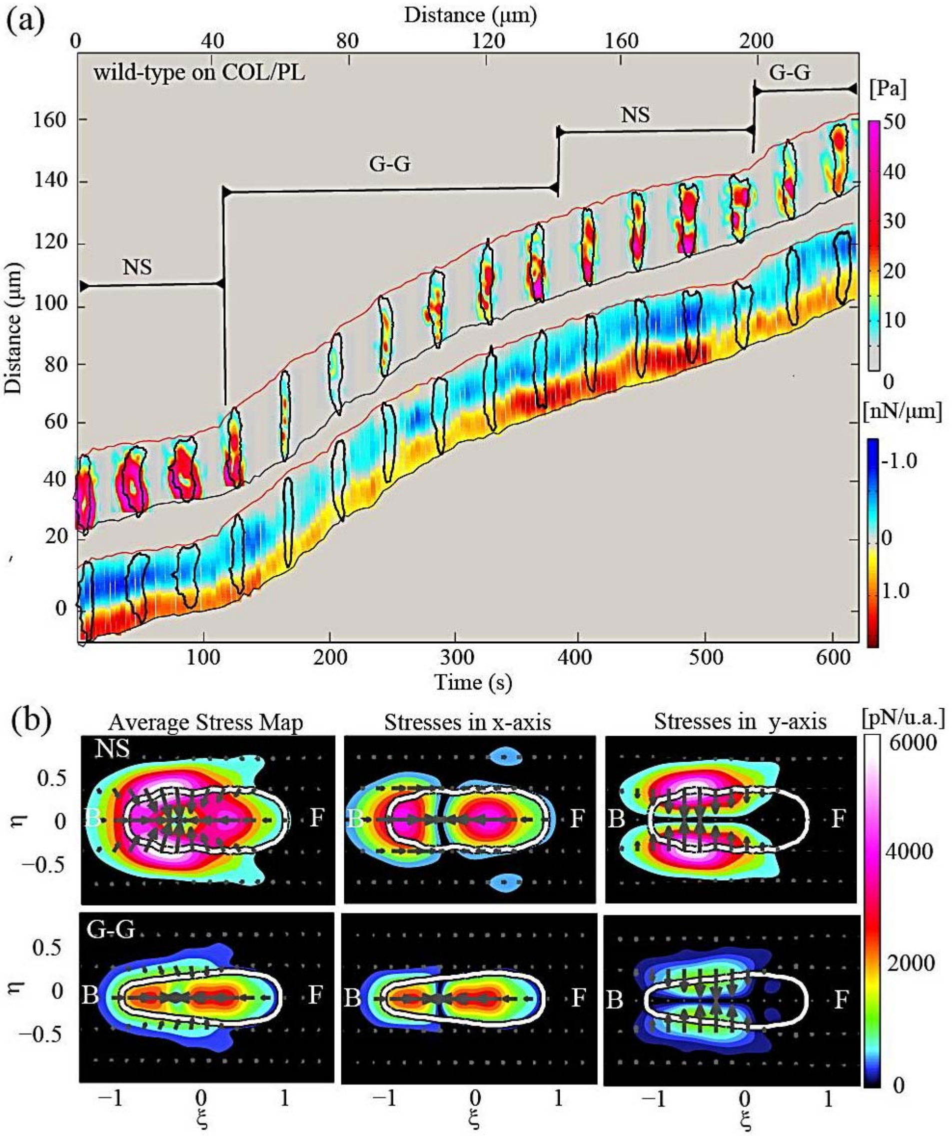

Figure 6.1: Spatio-temporal dynamics of motility modes in wild-type cells migrating on highly adhesive, poly-L-Lys-functionalized polyacrylamide substrata. (a) Kymographs of traction stresses *τ(x,y)* (upper part) and tension *T(x,t)* (lower part) for a representative wild-type cell chemotaxing on a 20mg/ml poly-L-Lys coated substratum (for explanations see Figure 2.5), showing that the cell alternates between two motility modes: the NS mode (nearly-stationary) and the G-G mode. (b) Average stress maps in cell based coordinates for the cell in panel (a), during the NS (upper row) and G-G (lower row) motility modes. The second and third columns show the axial and lateral component of the stresses respectively.

On poly-L-Lys, initially, both front and back adhesions are stationary (Figure 2.5.c-d). We named this new mode "NS" (*nearly stationary*), referring to the extremely low velocity of migration. The cells initiate movement from the NS mode by producing strong lateral contractions (lateral squeezing) with values similar to those of the axial contractions (Figure 6.1.b and Figure 6.2.e-g).

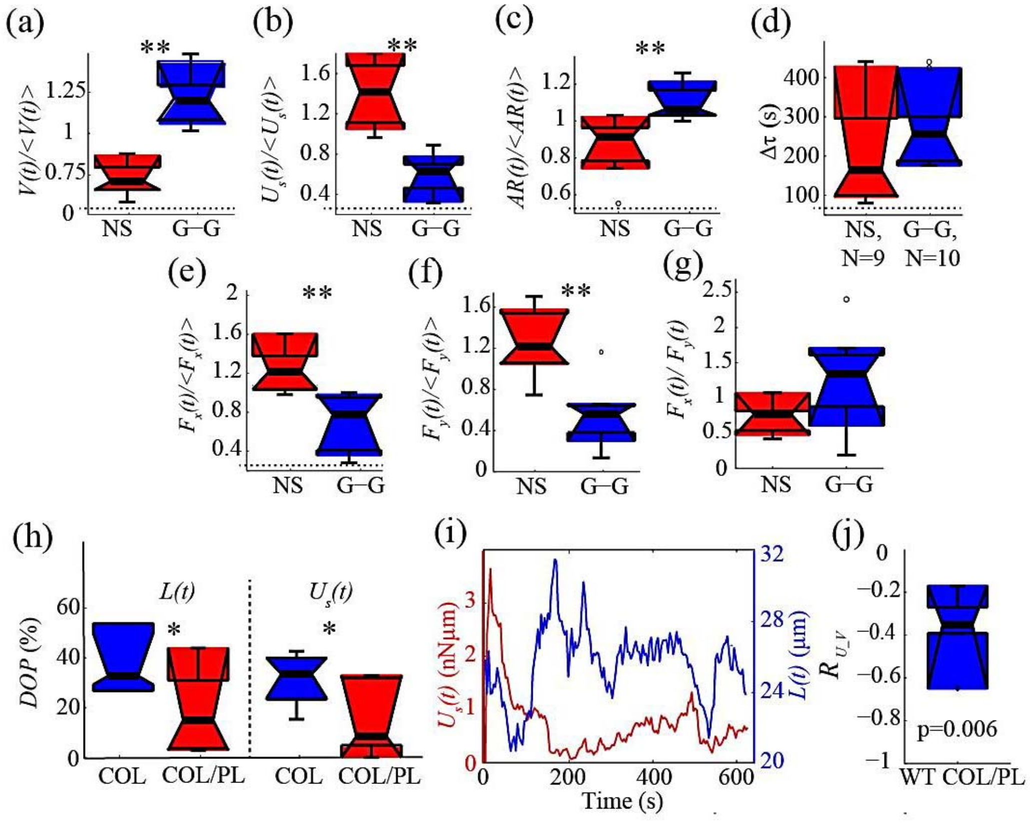

Figure 6.2: Statistics of motility modes in wild-type cells migrating on highly adhesive, poly-L-Lys-functionalized polyacrylamide substrata. (a-g) Boxplots of the motility parameters corresponding to the NS (red) and G-G (blue) motility modes for N=6 wild-type cells chemotaxing on 20mg/ml poly-L-Lys coated substrata, similar to Figure 3.5.a-g. (h) Degree of periodicity (*DOP*) of the cell length and strain energy for N=8 and N=6 wild-type cells on normal (COL) and poly-L-Lys coated substrates (COL/PL) respectively. (i) Cell length, *L(t)* (blue) and strain energy, $U_s(t)$ (red) as a function of time for the cell shown in Figure 6.1.a. (j) Boxplot of the correlation coefficient between the strain energy, $U_s(t)$ and the velocity of migration, *V(t)* for N=6 wild-type cells showing negative correlation ($p$=0.006).

This directed, lateral contractility leads to an elongation of the cell's body and the protrusion of a pseudopod. Cells randomly switch from the NS to a G-G like mode in which the cell forms no persistent front nor back adhesions, but forms numerous, weak, transient adhesions all along the cell's length instead (Figure 6.1.a and Figure 6.3).

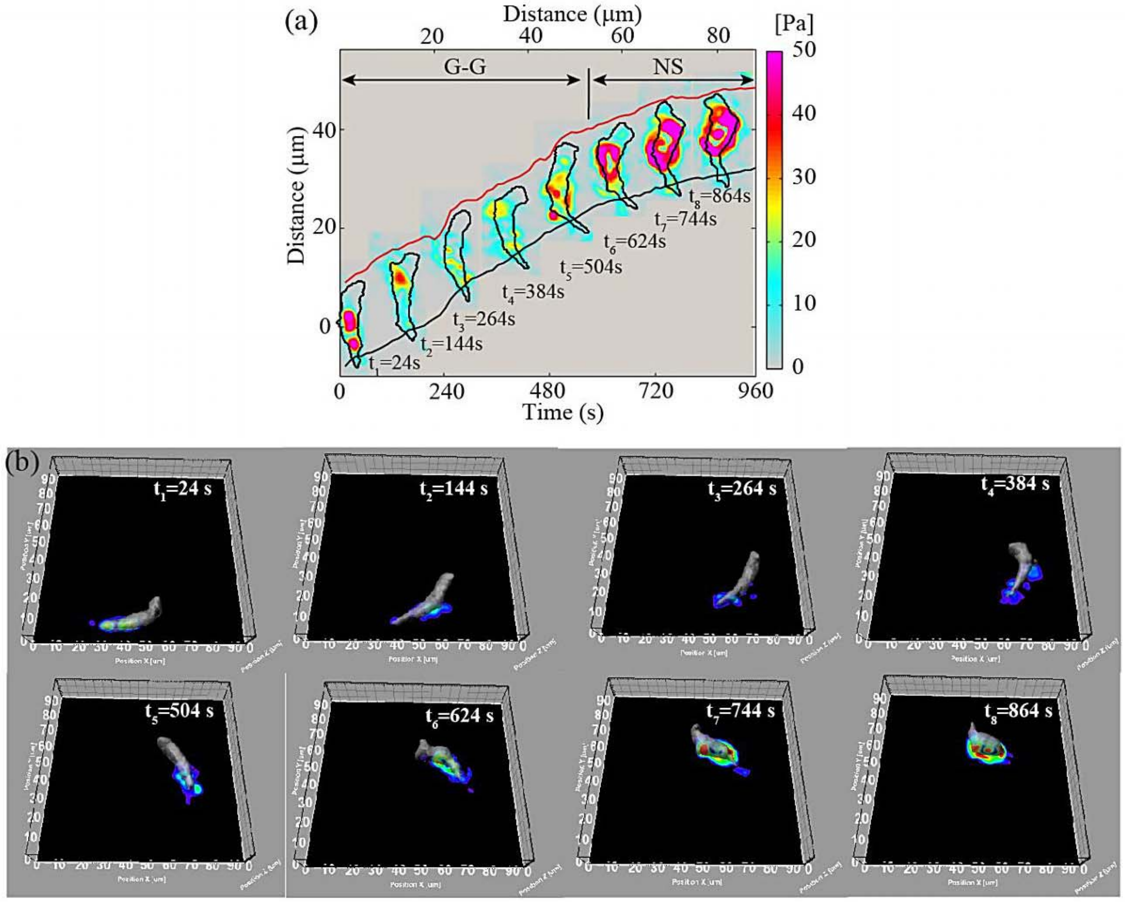

Figure 6.3: Three-Dimensional Characterization of NS and G-G motility modes on highly adhesive substrata. (a) Time evolution of the magnitude of the instantaneous traction stresses $\tau(x,y)$ for a representative wild-type cell expressing *lifeact*-GFP (F-actin marker) that is migrating on a poly-L-Lys coated substratum, while it is implementing the G-G ($t_1$-$t_5$) and NS ($t_6$-$t_8$) motility modes respectively. (b) Time evolution of the traction stresses and the 3D shape of the same cell. Notice that in the *G-G* mode the cell is barely touching the substrate, exerts weak stresses at various adhesion sites, which are gliding ($t_1$-$t_5$), whereas in the NS mode the cell is essentially stationary, and exerts high lateral stresses ($t_6$-$t_8$). Notice that during the G-G mode the cell is barely attaching at the substrate, its front is always lifted and it forms multiple, weak, transient adhesions. On the contrary, during the NS mode the cell rounds up and exerts higher stresses all around the cell periphery.

The cell's aspect ratio in the NS mode is considerably larger than in the G-G mode (Figure 6.2.c). When comparing the two main modes for cells migrating on collagen surfaces (S-S and S-G) and for cells migrating on poly-L-Lys coated substrates (NS and G-G), we observed that the strain energy in the S-G and G-G modes is lower than that in the S-S and NS modes, but this difference was greater on the more adhesive substrate (Figure 6.2.b). We also found that in the NS mode, the cells move even slower (3.3 μm/min; occasionally even seeming to get stuck and be unable to continue moving) than they do in the G-G mode (6.5 μm/min). While the speeds of the cells in both modes on poly-L-Lys are 40-50% slower than those of cells on collagen alone, the strain energy in the NS mode is >200% higher than in the G-G mode (Figure 6.2.b and Table 6.1). The duration is similar for both modes and is >2-fold higher than those of the two main modes of wild type migrating on regular substrates (Figure 6.2.d).

Table 6.1: Summary and comparison of the average motility parameters for wild-type cells on poly-L-Lys coated substrate (N=6) versus control (collagen-coated substratum, N=10). The parameters shown include the averages of speed of migration (*V*); aspect ratio (*AR*); cell length (*L*); strain energy ($U_s$); axial force ($F_x$); lateral force ($F_y$). Red colored numbers indicate the percentage increase (+) or decrease (-) of $F_x$ and $F_y$ with respect to control.

| Cell Type | *V* (μm/min) | *AR* | *L* (μm) | $U_s$ (nNμm) | $F_x$ (nN)+%incr | $F_y$ (nN)+%incr |
|---|---|---|---|---|---|---|
| WT on COL | 11.10 | 3.39 | 28.3 | 0.51 | 0.92 | 0.53 |
| WT on COL/PL | 4.94 | 2.76 | 17.80 | 0.76 | 0.84-9% | 0.73+43% |

### 6.1.2 Axial and lateral stresses do not increase proportionally when the cell switches from the G-G to the NS mode

To understand the role of contractility in the G-G and NS modes under conditions of increased adherence, we compiled average traction stress maps for both modes in cell-based coordinates and dissected their axial and lateral components (Figure 6.1.b). Interestingly, we found that on the very adhesive substrates, the axial and lateral stresses do not increase proportionally when the cell switches from the G-G to the NS mode (Figure 6.2.e-g).

In the G-G mode, the magnitude of the axial stresses decreases by half while the lateral squeezing decreases by only one third (Figure 6.2.e-g). Moreover, we found that the change in the magnitude of both axial and lateral traction stresses between the two main modes implemented by wild-type cells migrating on poly-L-Lys coated substrates (NS, G-G) is more pronounced compared to the change between the two main modes implemented by wild-type cells on collagen-coated control substrates (S-S, S-G). In addition, we found a strong negative correlation between the velocity of migration and the strain energy (Figure 6.2.j).

### 6.1.3 Wild-type cells migrating on adhesive substrates do not follow a motility cycle

Inspection of the traction tension kymograph of a large number of wild-type cells chemotaxing on highly adhesive substrate, reveals that the positions of the front and back edges of the cells are parallel to the trajectory of the cells' centroid (Figure 6.1.a). The above observation suggests that cells migrate on highly adhesive surfaces without undergoing significant changes in their length. Consistent with this observation, we found that the time evolution of cell length as well as the strain energy show a considerably reduced level of periodicity when compared to the modes described above for wild-type cells chemotaxing on collagen only substrates (Figure 6.2.h, i). Figure 6.3.b shows the traction stresses together with the three-dimensional (3D) reconstruction of the cell when migrating on a poly-L-Lys coated substrate (Figure 6.3.a-b). Notice that the cell is initially in the G-G mode, forming numerous, weak, transient adhesions while its body (especially the front) is barely in contact with the substrate. When the cell enters the NS mode, it starts rounding and exerting stresses of higher magnitude all around its periphery.

### 6.1.4 *abp120$^-$* and *mhcA$^-$* cells are unable to migrate on highly adhesive substrate

Unlike wild-type cells, *mhcA$^-$* cells are unable to move on a poly-L-Lys coated substrate as previously reported (80). We also observed this for *abp120$^-$* cells, but the effect is not as dramatic as in *mhcA$^-$* cells. When *mhcA$^-$* and *abp120$^-$* cells are placed on poly-L-Lys, they firmly attach to the substrate, generating contractile traction stresses. However, most of these cells are unable to generate enough lateral squeezing to break the adhesions, adopt a rounder shape, and eventually lyse (Figure 6.4).

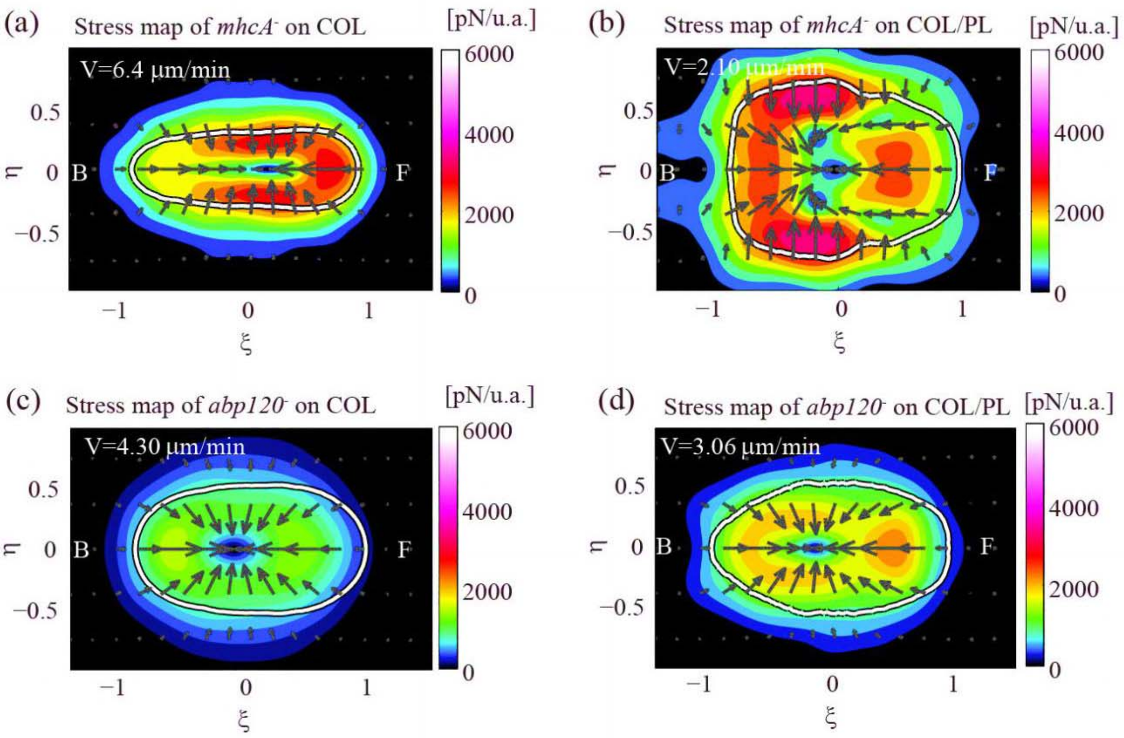

Figure 6.4: Average stress maps of mutants with F-actin crosslinking defects placed on substrates coated additionally with poly-L-Lys. (a, b). Average stress distribution pattern for (a) *mhcA*$^-$ cells (N = 8) on regular collagen-coated substrates and (b) on substrates additionally coated with 20mg/ml poly-L-Lys (N = 5). The contour maps show the average traction stress field, computed in a reference frame rotated to have the *x*- and *y*-axes coincide with the instantaneous principal axes of the cells. All dimensions are scaled with the length of their instantaneous major axis, a. Details of how the cell-coordinate system used in these plots is constructed can be found elsewhere (29). The colors indicate the magnitude of the stresses in pN/unit area, and the arrows indicate their direction. The white contours show the average shape of the cells in this reference frame. The front (F) of the cell corresponds to x > 0 and the back (B) to x < 0. The migration speed (*V*) is indicated on the upper left corner of the stress maps, in white color. Notice that *mhcA*$^-$ cells cannot essentially move on highly adhesive substrates. They exert stresses of slightly higher magnitude to the ones they exert on regular substrates, all around the cell periphery and round up. (c) Same as panels a for *abp120*$^-$ cells (N=9 cells). (d) Same as panels b for *abp120*$^-$ cells (N=5 cells).

In order to understand why these two mutant strains are unable to move on adhesive substrates, we placed the cells on the poly-L-Lys treated substrates and recorded the displacements of the beads embedded on the substrate. Few cells would move with an extremely slow speed before eventually lysing. Thus, we recorded the movement of these cells and extracted their displacement field. Alternatively, before the cells eventually would lyse, we could have added some detergent to the substrate and remove the cells to obtain a reference image of the beads in order to extract the displacement field induced by the cells during the period that they would be unable to move. We found that *mhcA*⁻ cells on adhesive substrates exert similar magnitude stresses compared to regular substrates, and like in the control wild type case these contractile stresses are found all around the periphery of these cells. This finding suggests that *mhcA*⁻ cells cannot really modulate their traction stresses, as wild-type cells do, which increase their traction stresses' strength when placed on an adhesive environment. Moreover, this finding suggests that it is Myosin II responsible for the ability of wild-type cells to squeeze strongly laterally and eventually achieve migration when placed on adhesive substrate.

We performed the same experiment for *abp120*⁻ to assess whether the cells can modulate the strength of their stresses when placed on adhesive substrates, similar to *mhcA*⁻ cells, or not. In marked contrast to *mhcA*⁻ cells, we found that *abp120*⁻ when placed on adhesive substrate, similar to wild-type increase their traction stress strength significantly and maintain a stress distribution similar as the one observed on regular collagen coated substrates but with increased lateral squeezing. Nevertheless, the increase in the traction stress strength and lateral stresses is not sufficient for the cells to achieve efficient movement forward. This finding confirms our hypothesis that Myosin II is involved in the ability of the cells to develop lateral stresses, since *abp120*⁻ indeed increase their lateral squeezing. In addition, it suggests that for cells to migrate on adhesive environments, apart from their ability to squeeze laterally crucial is also their proper cytoskeletal organization (crosslinking) that will permit the cells to protrude efficiently a front.

## 6.2 Cells become less polarized, exert higher stresses and only implement the S-S motility mode when migrating on stiffer substrates

As indicated in the previous chapters, the spatiotemporal coordination of traction forces and adhesion dynamics plays an important role in establishing different motility modes during migration.

To further understand this coordination and to assess the role that the strength of the adhesions and the dynamics of their assembly and disassembly play in the migration process, we examined the movement of cells chemotaxing on substrates of different stiffness.

It has been shown that *Dictyostelium* cells as well as other cell types spread much more on rigid surfaces (glass or stiff gels) than on soft surfaces (130). In certain cases, cell migration has been shown to be guided by gradients in substrate rigidity so that the cells move preferentially towards regions where the substrate is stiffer in a process called durotaxis (133). From these observations, one may predict that cells can sense the mechanical properties of their substrate and respond to them. Lo et al. suggested that cells go through a truly active, tactile exploration process by exerting contractile forces, and then, by interpreting the deformation of their substrate, they determine a preferred direction for their movement (133). It has also been suggested that certain cell types adapt/regulate their contractility in accordance with the substrate's stiffness, increasing both their contact area and traction forces when on stiff substrates (129, 133).

In the section 6.2 of this chapter, we investigate the effect of increasing substrate stiffness on the mechanics of wild-type *Dictyostelium* migration. The cells were placed on regular 1.2 kPa polyacrylamide substrates and on stiffer 5.6 kPa substrates. Using stiffer substrates leads to displacement fields that cannot be detected. The cells were also placed on glass substrates to further compare the kinematics of migration with the softer gels. The present study showed that *Dictyostelium* cells, similar to other cell types, respond differently when their substrate stiffness is tuned.

### 6.2.1 Migration speed and Aspect ratio is lower for cells migrating on stiffer substrates

We compared the kinematics of wild-type cell migration on soft substrates of 1.2 kPa, on medium stiffness 5.6 kPa substrates and on glass. We found that cells on soft substrates (1.2 kPa) migrate with an average speed ~13μm/min. The speed is reduced 23% on 5.6 kPa gels and 38% on glass (Figure 6.5.a). As shown in Figure 6.5.b, we also found that the aspect ratio of the cells is reduced when migrating on stiffer surfaces.

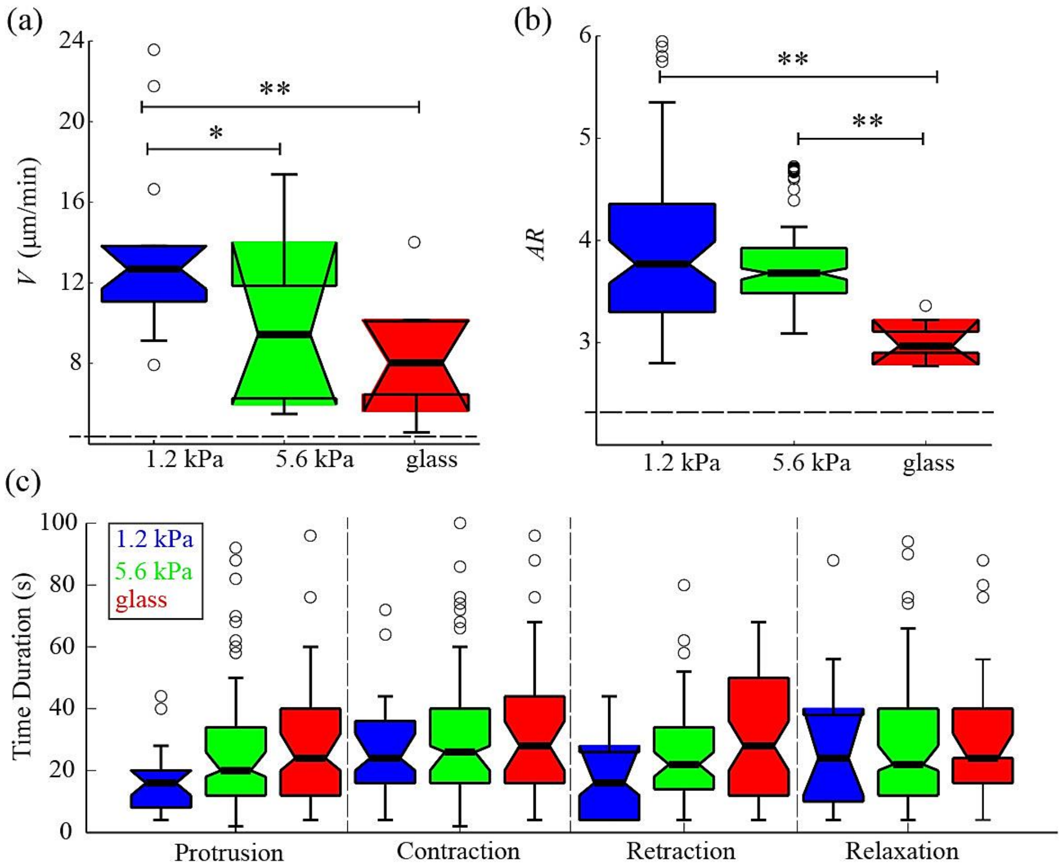

Figure 6.5:Boxplots of kinematic parameters of chemotaxing wild-type cells on regular 1.2 kPa substrates (blue), stiffer 5.6 kPa substrates (green), and *on glass* (red) cells. (a) Speed of migration (μm/min). (b) Aspect ratio (cell length divided by cell width). (c) Time duration of each of the four phases comprising the motility cycle. Splitting into phases was performed using the cell length time record after verifying that in all three cases cells still migrate periodically. Open circles represent outliers, and the notched section of the boxplots shows the 95% confidence interval around the median. Asterisks denote significant differences between distributions: *, $0.01 < p_d < 0.05$; **, $p_d < 0.01$ (Wilcoxon rank sum test for equal medians).

Figure 6.6.a shows the area fluxes, or else area gains and losses (red: positive are flux or gain in cell area; blue: negative area flux or loss in cell area), for all substrates which range from 1 to 5 μm$^2$/s, in agreement with previous findings (89). We found that cells on stiffer substrates adopt a more spread out shape compared to the softer substrates where the shape of the cells is more polarized.

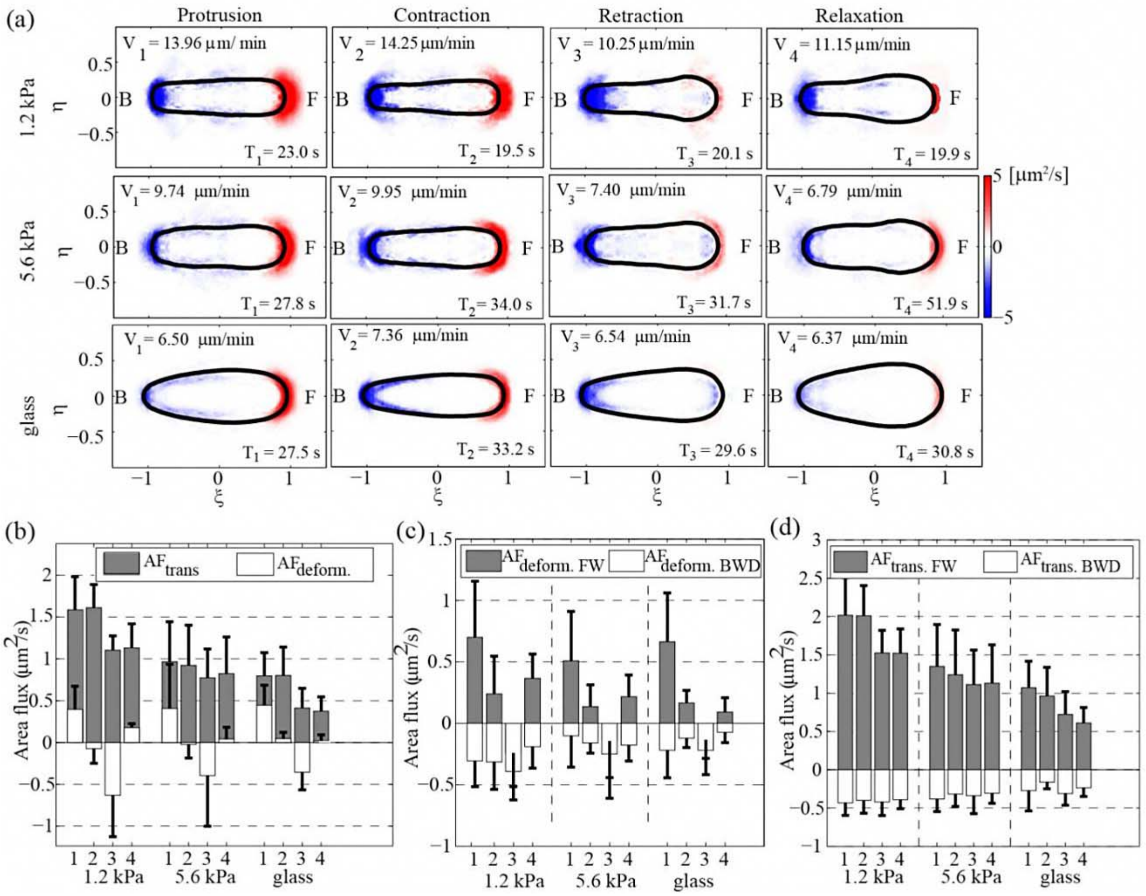

Figure 6.6: Phase-averaged area fluxes of wild-type cells on substrates of varying stiffness. (a) Phase-averaged area fluxes and cell shape corresponding to the four stereotypical stages of the motility cycle.First row refers to chemotaxing wild-type cells on regular 1.2 kPa substrates, second row to stiffer 5.6 kPa substrates, and third row *to glass* substrate. The contour maps show the average area flux field, measured in a reference frame rotated to coincide with the length of their instantaneous major axis, a. The colors indicate the magnitude of the area fluxes in μm$^2$/s (red: positive area flux or gain of cell area; blue: negative area flux or loss of cell area). (b) Area flux due to cell shape change (area flux of deformation, white boxes) and area flux attributable to continuous translocation (area flux of translocation, in gray). Both types of average area fluxes during each phase are shown as determined by our phase statistical analysis. (b) Phase-averaged area flux of deformation at the front half (forward) in gray and at the back half (backward) in white of the cells. (c) Phase-averaged area flux of translocation at the front half (forward) in gray and at the back half (backward) in white of the cells.

### 6.2.2 Area flux of deformation remains constant when the stiffness of the substrate changes

As shown by Alonso-Latorre et al. (89), if a cell simply moves forward without altering/deforming its shape, the area fluxes at the front of the cell is equal and opposite to the area fluxes at the back of the cell. That is not the case in amoeboid cells, since while migrating they also deform their body, giving rise to an additional component of area flux, namely, that of deformation. To distinguish between shape preserving translocation and the component of cell movement that involves deformation, two different types of area flux have been calculated $AF_{\mathrm{trans}}$ and $AF_{deform}$ respectively, as shown elsewhere (89). We compared both types of area fluxes in the case of wild-type cells migrating on soft substrates of 1.2 kPa, on medium stiffness 5.6 kPa substrates, and on glass (70 GPa) (134). Figure 6.5.b shows the phase-averaged total area fluxes of deformation and translocation.

We found that, similar to the cell length, the area fluxes vary periodically (Figure 6.6.b-d). These plots also confirm that our cycle splitting algorithm, which sorts the motility cycle into phases, can capture the physical events defining it. Figure 6.6.b shows that the area fluxes of translocation, for all three cases and for all phases, are always positive. On the other hand, in all three cases, the area fluxes of deformation are positive in protrusion where the cell deforms its front, protruding a pseudopod, by means of F-actin polymerization (Figure 6.6.b). In addition, during retraction, all area fluxes of deformation are negative, suggesting that during the specific phase the cell breaks its back adhesions and retracts forward. During contraction and relaxation, the area fluxes of deformation are low, especially on stiffer substrates. Figure 6.6.c, which shows the area flux of deformation at the front and back of the cell respectively, confirms the above observation, showing that on stiffer substrates, the ability of the cell to deform both at the front and at the back is reduced primarily during contraction and retraction. Most importantly Figure 6.5.b, shows that when moving on stiffer substrates what mostly changes is the area flux of translocation rather than of deformation (Figure 6.6.b,c). That suggests that the amount by which the cell body is deformed does not depend strongly on the substrate's stiffness. Conversely, the translocation of the cell strongly depends on the Young's modulus of the substrate.

### 6.2.3 Cells exert higher stresses on stiffer substrates, migrate following a motility cycle and implement the S-S motility only

We found that when wild-type cells are placed on a stiffer substrate (1.2 kPa versus 5.6 kPa), they exert ~80% higher magnitude stresses (Figure 6.7.a, b and Figure 6.8.a).

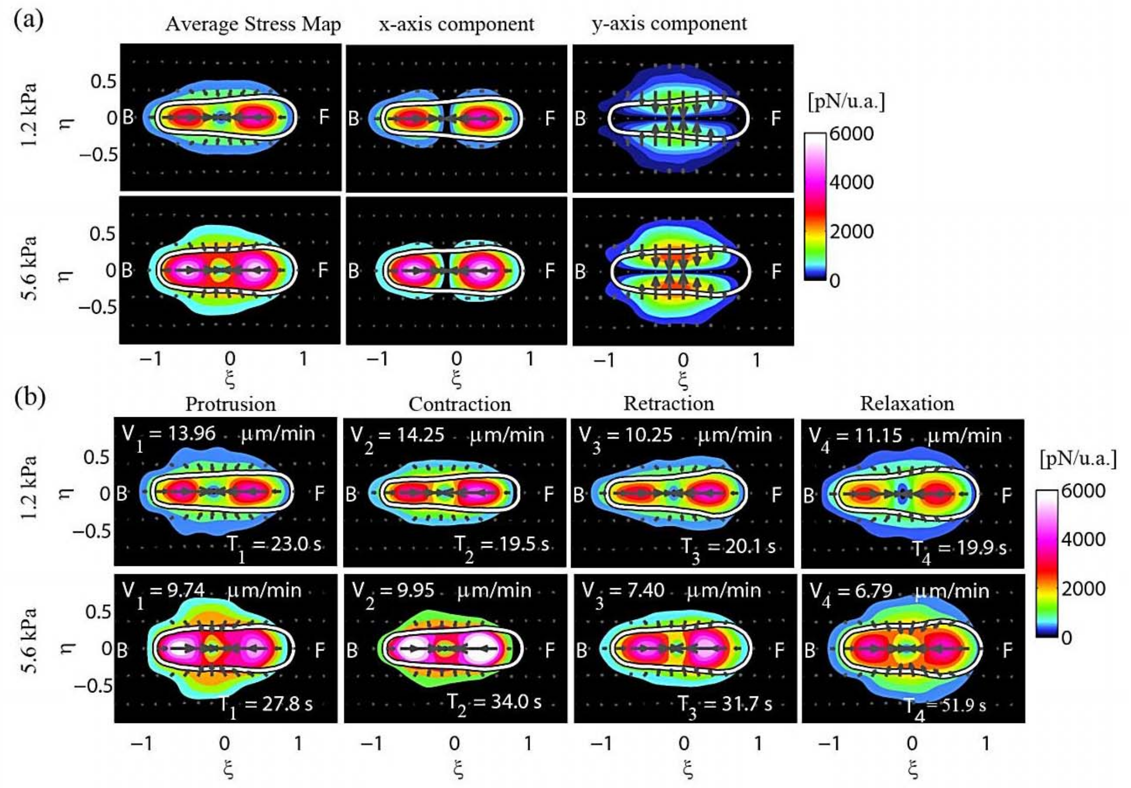

Figure 6.7: Traction stresses on substrates of varying stiffness. (a) Upper and lower rows refer to wild-type cells chemotaxing on substrate of 1.2 kPa and 5.6 kPa stiffness, respectively. The stress maps on the left column show the average stress field for both categories, measured in a reference frame rotated to coincide with the instantaneous principal axes of the cells and scaled with their length. The colors of the contour maps indicate the magnitude of the stresses in pN/unit area, and the arrows indicate their direction. The white contours show the average shape of the cells in this reference frame. The front (F) of the cell corresponds to $\xi > 0$ and the back (B) to $\xi < 0$. Middle and right column stress maps show the components of the axial and lateral traction stresses, which are parallel and perpendicular to the major axis of the cell respectively. (B) Phase-averaged traction stress maps for wild-type cells chemotaxing on substrate of 1.2 kPa (upper row) and 5.6 kPa stiffness (bottom row) (for explanation see panel (a). The legends show the average durations, $T_1, \ldots, T_4$, and the corresponding average speeds during each phase, $V_1, \ldots, V_4$ of the motility cycle. Notice that in all cases the traction stresses are at least twice as high when cells are chemotaxing on the stiffer substrate. In addition, in the latter case, the cells are more spread-out and their migration speed is lower.

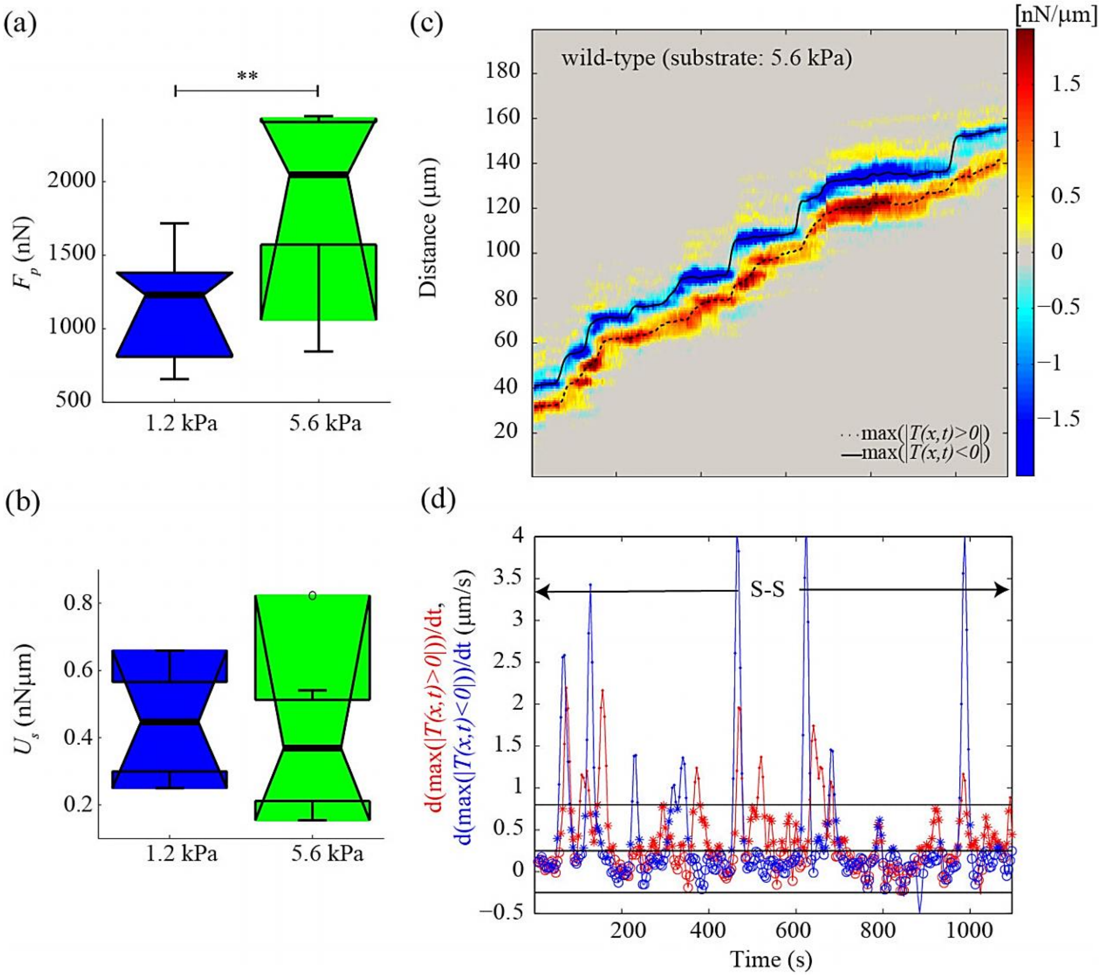

Figure 6.8: Traction stresses significantly increase when cells migrate on stiffer substrates while only the S-S motility mode is implemented. (a) Boxplot of the pole forces, $F_p$ for chemotaxing wild-type cells on regular 1.2 kPa substrates (blue) and stiffer 5.6 kPa substrates (green). (b) Boxplot of the strain energy, $U_s$ for chemotaxing wild-type cells on regular 1.2 kPa substrates (blue) and stiffer 5.6 kPa substrates (green). Open circles represent outliers, and the notched section of the boxplots shows the 95% confidence interval around the median. Asterisks denote significant differences between distributions: *, $0.01 < p_d < 0.05$; **, $p_d < 0.01$ (Wilcoxon rank sum test for equal medians). (c) Traction tension kymograph, $T(x,t)$ of a representative wild-type cell chemotaxing on a stiffer 5.6 kPa substrate. Black solid (dotted) lines track the spatio-temporal evolution of the peak value of the negative (front) (positive (back)) traction tension, $T(x,t)$. The two lines are smoothed in time using a triangular 5-point kernel. (d) Identification of the motility modes based on the speed of adhesion regions for the traction tension kymograph shown in panel (c). Blue and red solid lines show the speed of the adhesion regions, defined as the slope of the solid and dotted lines in panel (a). The green line shows the velocity of the cell centroid, obtained after smoothing its trajectory with the same kernel used for the adhesion regions. Black solid lines indicate the first and third quartiles of the distribution of the adhesion speeds. Speed points that are lower than the first quartile are marked with a hollow circle, while those between the first and third quartiles are marked with an asterisk. Speed points above the third quartile were observed only when new adhesions were created or existing adhesions were broken. These points are not considered for mode sorting, together with their two previous and posterior data points. Notice that only one mode arises, the S-S or stepping-stepping when wild type migrates on stiffer substrate.

Nevertheless, the strain energy when comparing the two cases is not significantly different (Figure 6.8.b). This suggests that the displacements that the cells induce to their substrate are smaller when they are moving on stiffer substrates. Nevertheless, to induce the smaller displacement observed in the 5.6 kPa gels, the cells need to apply twice as much force (Figure 6.8.a). Figure 6.7.b, shows the phase-averaged stresses of wild-type cells moving on both types of substrate and confirms that in both cases, cells move following a well-defined motility cycle, preserving the phase characteristics observed on regular 1.2 kPa, although both the velocity of migration and the aspect ratio is lower on the stiffer substrate.

Finally, we applied our mode-splitting algorithm to dissect motility into modes using the traction tension kymographs of a large number of wild-type cells chemotaxing on substrates of 5.6 kPa. Unlike wild-type cells chemotaxing on 1.2 kPa gels, we found that on stiffer substrates cells just implement the S-S mode (Figure 6.8.c-d). This finding supports our hypothesis, that the switching from the S-S to the S-G mode observed on the soft 1.2 kPa gels may be due to inhomogeneities of the substrate, most probably related to the collagen spreading. Thus, it is possible that when the cell senses a stiffer environment/substrate, it switches to the S-S mode while when the substrate is softer, it switches back to the S-G motility mode.

## 6.3 Discussion

In this chapter, we have used FTFM to measure the spatial and temporal evolution of traction stresses and shape dynamics during migration, using kymograph representations of the traction tension to determine, for the first time, how motile cells coordinate the formation and disassembly of adhesions as well as the generation of axial and lateral traction stresses when the mechanics of their substrate are altered. The mechanical aspects of the substrate, we examined, were the adhesivity and the stiffness.

Our previous studies on the movement of wild-type cells on our “standard” collagen-coated substrate and those described herein indicate that the anterior/posterior traction stresses are approximately double the lateral stresses that result from the “squeezing” inward from the sides of the cells perpendicular to the AP axis. We envision that these lateral forces play important roles in cell motility, possibly by allowing the cell to respond differently to such specific environmental conditions as increased substrate adhesiveness. These lateral forces may also be part of the underlying mechanism that produces blebs, which, along with anterior, dendritic F-actin polymerization, are thought to be important components underlying cell motility. On poly-L-Lys-coated substrates, we showed that wild-type cells also exhibit a bimodal motility, although the dominant modes are the NS and the G-G modes. In contrast to movement on collagen, on poly-L-Lys during the NS mode, cells exert lateral contractions that are ~2-fold stronger than those exerted on collagen. Cells use these increased lateral contractions, localized in the back half of the body, to break the strong adhesions with the substrate, while simultaneously promoting the protrusion of the front pseudopod and elongating along the direction of motion. When cells are first placed in a chemoattractant gradient on poly-L-Lys, it takes more time to initiate cell movement than when cells are plated on standard collagen-coated substrates, presumably because the cells must develop sufficient directional forces to break the cell-substrate adhesions produced by the lateral contractions.

In the G-G mode on poly-L-Lys, multiple, weaker adhesion sites are observed, that are not stationary. As the cell moves, its length remains almost constant and no apparent periodicity is observed in the time evolution of the strain energy appearing as if the cell is “skipping” along the surface. On a sticky surface, however, the cell overcomes the increased resistance to motion by forming and disassembling adhesions rapidly. This is consistent with the amount of F-actin fluorescence present in the plane of poly-L-Lys coated substrate, thereby indicating that the surface area of the cell in contact with the substrate is considerably reduced both during the protrusion of the frontal pseudopod in the NS mode and throughout the G-G mode as compared to the collagen-only substrates. When stronger adhesions are formed, the cell’s speed rapidly decreases. The cell then remains in the NS mode until a sufficient proportion of adhesive bonds are broken by strong lateral contractions.

We found that cells lacking essential F-actin crosslinkers (*abp120*$^-$ and *mhcA*$^-$ cells) are unable to move on highly adhesive substrates. We examined the reason of this behavior by measuring the traction stresses of these cells prior to lysis. We found that *mhcA*$^-$ cells, when placed on highly adhesive substrates, round up, exerting stresses all around the periphery of the cell, which are not significantly different in strength from those on regular substrates. This suggests that MyosinII is essential to the movement under conditions of increased adhesivity, due to its motor role and/or due to the integrity it provides to the F-actin cytoskeleton acting as a crosslinker. We also found that *abp120*$^-$ cells, on highly adhesive substrates, prior to lysis, increase their traction stress strength and lateral squeezing. These findings suggest that the ability of the cell to produce high lateral squeezing when placed on adhesive environments is most probably due to the activity of the Myosin II motor, since lack of it results in cells that are unable to squeeze strongly laterally and thus migrate. Furthermore, it suggests that both the activity of Myosin II and the cell's cytoskeletal integrity/crosslinking are necessary conditions for movement on adhesive substrates.

When the stiffness of the substrate is altered, the migration pattern of wild-type cells is altered as well. Although they continue migrating following a motility cycle, their migration speed is reduced, their shape becomes less polarized, and the traction stresses they exert on their substrate are increased significantly. The cells stop migrating by switching between different motility modes and just implement the S-S or Stepping-Stepping mode. This finding suggests that the switching between modes on regular 1.2 kPa substrates may be due to substrate inhomogeneities.

In conclusion, the present chapter has shed more light on a more precise understanding of how the coordination of traction stresses together with the adhesion dynamics, result in efficient amoeboid cell migration. We showed that cells migrate by switching between several modes of distinct adhesion dynamics when placed on soft substrates and/ or adhesive ones. Our findings also reveal that changes in cell migration speed are concomitant to changes in both contractility and adhesion dynamics. Nevertheless, we did not see this switch on stiffer substrates where the cells move even more periodically by just “Stepping” both at the front and at their back adhesion sites. We have further demonstrated a critical role for lateral contractility in driving cell migration in cells placed on highly adhesive substrates. We have shown that mutant cells lacking the Abp120 F-actin crosslinker and the Myosin II motor are unable to increase their traction stresses so as to be able to migrate on adhesive substrates, suggesting that both the integrity of the F-actin cytoskeleton and the motor activity of Myosin II are essential for movement under these conditions and for the development of lateral contractility. We propose that these are highly conserved mechanisms that function in a range of amoeboid cells, including leukocytes, as well as other forms of cell motility.

Chapter 6 is being prepared in part for publication. Chemotaxing amoeboid cells migrate by switching between distinct modes of adhesion dynamics and contractility. Bastounis E., Meili R., Alvarez-Gonzalez B., del Álamo J.C., Lasheras J.C., Firtel R.

# Chapter 7
# Concluding Remarks and Future Work

This dissertation deals with a detailed analysis of the spatiotemporal coordination between the kinematics, traction forces and adhesion dynamics of amoeboid cells migrating towards a chemical stimulus over elastic substrates. Using an improved analytical Fourier method for the calculation of the traction stresses exerted by cells, we have systematically studied and compared the behavior of wild-type cells on regular collagen-coated substrates to those on substrates of different mechanical properties. We have also studied and compared the behavior of wild-type cells to cells that lack key cytoskeletal proteins. Following the above methodology allowed us to understand the role and the importance that the substrate and specific cytoskeletal proteins assume and play during guided amoeboid single cell migration.

This specific chapter reflects on the results of this dissertation. Section 7.1 recapitulates the work presented in the previous chapters and summarizes the specific contributions/conclusions. Section 7.2 presents the possible directions of future work that can be carried out on the foundations of this thesis. Finally, Section 7.3 recapitulates the objective and contribution of the studies carried out and presented in this Dissertation.

## 7.1 Summary of the Chapters and Their Specific Conclusions

### 7.1.1 Chapter 1 – Introduction

Chapter 1 introduces the background and motivation of this work. It points out the importance of cell migration for many physiological as well as pathological biological processes. It also clarifies that while there are many ways cells can move, this dissertation is focused on the study of the amoeboid type of crawling as it occurs in neutrophils or the simplified amoeboid model *Dictyostelium discoideum*. The main method followed to study the mechanics of single cell locomotion, Traction Force Cytometry (TFC), is introduced here. In addition, background information and previous knowledge related to the mechanical contribution of key cytoskeletal components, crucial to the cell migration process, is also provided., Moreover, the vision and specific aims of this work, the main problems to be solved, as well as the goals to be achieved are presented. Finally, a short outline of the dissertation and the structure of its chapters is provided.

### 7.1.2 Chapter 2 – Experimental Methods

In Chapter 2, we present the experimental methodology followed to perform the experiments carried out for this dissertation. We also offer a detailed description of the techniques that were developed to analyze and calculate various parameters characterizing the mechanics of motility. We show how we calculated both the axial and lateral components of the traction stresses, using an exact solution of the elastostatic equation based on Fourier expansions that express the tractions explicitly as functions of the deformations. In addition, we present how by jointly stacking the above measurements in space and time we could produce traction tension kymographs that allowed us to gain deep insight into the adhesion dynamics of cell locomotion. Moreover, we present the methodology followed to sort motility into different modes based on the adhesion dynamics of the cells, as revealed through thorough analysis of the traction tension kymograph data. Finally, by studying and characterizing the periodicity of the cell length and strain energy time records, we categorize the various cell lines depending on whether they move quasi-periodically or not. And, in the former case, we apply our cycle-splitting algorithm to gain further insight on the cyclic movement of the specific strains. The significance and innovation of this chapter can be further appreciated by reading the following chapters, which present the results obtained using all the aforementioned techniques.

### 7.1.3 Chapter 3 – *Dictyostelium* Cells Regulate Their Migration Speed by Alternating Between Two Motility Modes

In Chapter 3, using the aforementioned methodology, we study how the formation and disassembly of adhesions coupled with the generation of axial and lateral traction stresses control the migration efficiency of chemotaxing *Dictyostelium* amoebae. We reconfirm and show that their migration is composed of a repetitive sequence of canonical steps (phases of motility cycle) whereby the cells adhere, on average, at two sites at their back and front halves while constantly in a contractile state. Our analysis shows that the temporal evolution of the cell length, strain energy exerted on the substrate, and maximum F-actin florescence at the front of the cell, present a quasi-periodic evolution. All three-time records oscillate with the same frequency and are in phase while their frequency correlates with the mean migration velocity of the cells. Using the traction tension kymographs, we splitted motility into different modes and found that wild-type cells move by switching mainly between two modes of distinct adhesion and contractility dynamics. Moreover, we found that changes in adhesion dynamics accompany contractility and migration speed changes. The main conclusions of Chapter 3 are:

- Amoeboid wild-type cells undergoing chemotaxis on elastic substrates establish, on average, two stationary adhesion sites located at the front and back halves of their body and move by periodically modulating the strength of the axial contractility, following a relatively coherent (periodic) motion largely dominated by the front protrusion and rear retraction.
- Wild-type cells migrate by mainly switching between two motility modes (S-S and S-G) with distinct migration speed, adhesion dynamics, and periodic modulation of axial and lateral contractions of varying strength.
- *T*he S-S mode, characterized by two discrete, stationary adhesion sites located at the front and back halves of the cell, is associated with a slower velocity of migration.

- In the S-G mode, the cell also establishes anterior and posterior adhesion sites, although the back adhesion is continuously dragged forward while the magnitude of the traction stresses and motility speed are considerably reduced compared to the S-S mode.

### 7.1.4 Chapter 4 – Role of the Scar/WAVE Complex in Regulating Traction Forces During Amoeboid Motility

In Chapter 4, we elucidate the role of the dendritic F-actin polymerization at the cell's leading edge for efficient cell migration. To do that, we analyzed similarly to wild type, two mutant strains that lack two key proteins of the SCAR/WAVE complex that regulates the Arp2/3-mediated dendritic F-actin architecture at the leading cell edge (*scrA*$^-$ and *pirA*$^-$ cells). By establishing a quantitative comparison between wild-type, *pirA*$^-$ and *scrA*$^-$ cells, we provide new insight into the role that actin polymerization plays in the conservation of the periodicity of cell migration and also in the spatial and temporal regulation of the traction stresses and adhesion dynamics. The main findings/conclusions of this study are:

- Polarity and speed of the SCAR/WAVE mutants do not correlate with their F-actin levels. *pirA*$^-$ cells have higher F-actin content than wild type but move as slowly as *scrA*$^-$ that have less F-actin content than wild type.
- Disruption of the SCAR/WAVE complex causes the misregulation of the motility cycle. *pirA*$^-$ cells do not migrate in a periodic manner; thus, the ability of a cell to migrate efficiently does not depend on its F-actin content, but rather on its ability to move in a coordinated periodic manner.
- The strength of traction stresses differs in the SCAR/WAVE mutants and correlates with their altered F-actin levels. Phase-averaged F-actin levels at the frontal cell edge also correlate with the phase-averaged strength of traction stresses. Thus, the level of leading edge, SCAR/WAVE complex-mediated F-actin polymerizations is critical for the level and spatiotemporal control of the traction stresses.

### 7.1.5 Chapter 5 – Cytoskeletal Crosslinking Defects Impair Axial Contractility

In Chapter 5, we compare the mechanics of cell migration of wild-type cells with cells with defects in F-actin crosslinking. Two cell lines are chosen for this purpose: a) *abp120*$^-$ cells that lack the Abp120 protein which crosslinks actin filaments in an orthogonal fashion and b) *mhcA*$^-$ cells that lack the motor protein MyoII, which together with its motor function also has a crosslinking one. Following the same comparative approach of wild type to mutants used in Chapter 4 we arrived at the following main findings:

- Cells with cytoskeletal crosslinking defects rely on lateral contractility in order to move, underlining the key role of lateral contractility for cell migration.
- Unlike *mhcA*$^-$ cells which constantly contract laterally using many adhesion sites located at the cell's periphery, *abp120*$^-$ lack an effective pseudopod, move by establishing two adhesion areas, and by switching periodically from a mode in which they contract axially to a mode in which they contract laterally.

### 7.1.6 Chapter 6 – Mechanics of Amoeboid Cell Migration on Substrates of Varying Stiffness and Adhesivity

In Chapter 6, we investigate the role of adhesion in amoeboid cell migration by altering the mechanical properties of the substrate on which cells migrate. Using the same methodology as in the previous chapters, we compare the motility phenotype of our control group (wild-type cells on regular 1.2 kPa collagen-coated substrates) to wild-type cells moving on substrates that differ either in stiffness or in adhesivity. The chapter's main conclusions are:

- Wild-type cells chemotaxing on substrates of increasing stiffness increase the strength of their traction stresses but decrease their velocity while their shape becomes less polarized. They migrate with increased periodicity implementing just the S-S motility mode.
- The area flux of deformation remains constant while the area flux of translocation reduces when moving on stiffer substrates. Thus, the degree by which a cell gets deformed does not depend on

the elastic properties of its substrate.

- On substrates of increased adhesiveness, lateral contractility becomes essential for wild-type cell migration as well as the ability of the cells to increase the strength of their traction stresses. As a consequence, mutants with F-actin crosslinking defects are unable to migrate under such conditions.
- On substrates of increased adhesiveness, the motility modes employed by chemotaxing wild-type cells are completely different from those observed on regular substrates. The first mode consists of lateral squeezing aiming to break back adhesions while protruding a frontal pseudopod. During the second mode, the cells barely attach to the substrate forming adhesions that are transient, weak and gliding. Thus, the cell appears to act in an intelligent way in order to achieve migration in an adhesive environment.

## 7.2 Future Work

The work presented in this thesis provides several possibilities for further work. Whereas some of them concern straightforward extensions of the approach utilized and the developed techniques, there are also possibilities to combine the results of the thesis with other research areas. Among the most important and interesting issues (some of which are already being addressed in ongoing work), the following can be mentioned along with their potential limitations/boundaries:

### 7.2.1 Using the same tools to investigate whether the specific mechanisms are conserved in different cell types

We have already proposed that the migration mechanisms discussed in the current dissertation may be highly conserved and may function in a range of amoeboid cells, including leukocytes, as well as other forms of cell motility. Thus, to confirm and further investigate that, further experiments using cell types that exhibit amoeboid type motility, such as neutrophils are required. Additional work is needed to find the optimal conditions required for such cells to migrate on polyacrylamide substrates, including verifying with what protein to coat the substrates so that the specific cell type can attach and migrate, what chemoattractant to use, etc.

In addition, the method can also be used to study the mechanics of migration of less motile cells, implementing for instance mesenchymal type of motility (keratocytes, endothelial cells, neurons, etc.). Since the specific cells move significantly more slowly, it is possible that treatment with detergent will be needed at the end of the time-lapse recording of migration in order to remove the cells attached to the substrate and to be able to obtain a reference image of the beads to extract the displacement field.

### 7.2.2 Using the same tools to investigate the behavior of cells: (a) under different external conditions; (b) lacking key proteins involved in migration; (c) in the presence of toxins; (d) expressing different cytoskeletal protein fluorescent markers

In the present dissertation, we have investigated how wild-type *Dictyostelium* cells migrate on substrates of varying stiffness and adhesivity. There are many other parameters related to the external environment of the cell that can be further investigated using the methodology presented in this dissertation. Some examples are: 1. Varying the concentration of the protein coating the substrate (collagen); 2. Varying the concentration of the chemoattractant; 3. Using substrates with gradient of stiffness (durotaxis) as proposed by (135); 4. Using substrates with varying height; 5. Using substrates with varying porosity etc. We believe that in so doing, both the mechanosensivity and mechanoresponse of the cell will be better understood.

Throughout this dissertation, we have investigated and studied the migration of a wide range of mutant strains by comparing them to the migration of wild-type cells. Some mutants lacked specific F-actin crosslinkers (*abp120*$^-$ and *mhcA*$^-$), while others had misregulated dendritic F-actin misregulation (*pirA*$^-$ and *scrA*$^-$). Mutants lacking MyoII motor components (*elc*$^-$ and *mhcA*$^-$) were studied previously (31). Still, there are a number of other mutants with cytoskeletal defects available (described in the literature), and many more cytoskeletal proteins and upregulators known to play a crucial role in the mechanics of cell migration. Using the methodologies presented in this dissertation to examine more mutant strains will eventually allow us to have a more complete understanding of the biomechanics of cell migration.

Prior studies showed that amoeboid cells move by generating front to back traction stresses that are caused by protrusion of the leading edge by F-actin polymerization and by retraction of the trailing edge by MyoII/F-actin contraction (31, 111, 120, 136). Since F-actin polymerization and Myosin based contraction are so crucial to the cell's ability to move, we believe further studies should be conducted in that area. Toxins are commonly used to alter actin (cytochalasin, latrunculin, jasplakinolide, phalloidin) (137) and myosin II (blebbistatin) (138) dynamics. By performing experiments such as the ones described in this dissertation that use wild-type cells and adding gradually, increasing concentrations of these toxins could potentially answer many of the remaining questions related to the specific role of these two key components of cell migration.

Finally, the same way in which we used the *Lifeact* marker for F-actin to elucidate the relationship between the F-actin's localization and the traction stresses and to understand the relative timing of events that take place during the phases of the motility cycle, different markers could also be used and studied. These markers could include GFP-myosin (139) as well as upregulators of actin or myosin. Moreover, 3-channel time-lapse experiments could be performed using two fluorescent probes within the cell (for example, RFP and GFP) and a third for the substrate beads. Information about the relative timing and localization of different signaling molecules together with the traction stresses would lead to a more complete image of the biochemical and signaling events taking place during the specific phases of the motility cycle.

### 7.2.3 Extension of the current 2D method to 3D Flat: (a) planar 3D substrates; (b) 3D volumetric matrices

Previous methods to calculate cell traction stresses have usually assumed that the vertical stresses exerted by the cells on their substrate are negligible. Recent evidence shows that in many instances the vertical stresses are comparable to tangential stresses (140, 141). Nevertheless, it has been shown that the assumption that vertical stresses are negligible in the calculation of the cell traction stresses is not inaccurate. Recent calculations showed that with the 2D compared to the 3D method, the tangential stresses differ by just ≈ 10% (89). The above finding is important since it provides a proof that our studies of the 2D cell traction stresses are indeed meaningful, and that the 2D technique still provides useful information even if the vertical stresses are not taken into consideration (89). However, the presence of significant vertical stresses (the cell pushing down the substrate at its center and pulling it up from the sides) indicates the need for a more refined interpretation of the mechanical interaction of the cell with its substrate, possibly involving signaling processes triggered through the deformation of the cell nucleus (142). Both experimental and modeling efforts will be required to answer these questions.

Another possible extension of this work, apart from studying the 3D traction stresses exerted on a planar substrate, is to study cell migration across 3D matrices. Studying cell migration across a 3D matrix is crucial since that is the way migration occurs in the case of tumor cells or fibroblasts that are surrounded by tissue and ECM (143, 144). Although the impact and importance of such an experiment is expected to be tremendous, there are still a number of challenges that need to be addressed and solved. For instance, the mechanical characterization of such a matrix is difficult since it is constantly being remodeled due to the degrading activity of enzymes secreted by the cells (MMPs). In that sense, the matrix cannot be considered homogenous, and its non-linear mechanical properties need to be considered.

### 7.2.4 Studying the cell mechanoresponse to applied external forces: (a) mild hydrodynamic shear stress experiment; (b) micro-aspiration; (c) hypertonic/hypotonic buffers

It has been previously shown that a variety of eukaryotic cells exhibit force sensitivity, especially in the context of cell adhesion (145). For instance, fibroblasts adhere to the ECM through focal adhesions, whose number and surface area increase with the mechanical tension applied to the cell (Choquet et al., 1997; Riveline et al., 2001). Epithelial cells form closed vessels through the apposition of membranes bearing adhesion proteins (145). These structures are mechanically stabilized by expressing genes induced by the blood flow shear stress (Chappell et al., 1998; Nerem et al., 1998). Thus, the mechanosensitivity seems to have evolved from mechanisms of cell osmotic protection since stress-activated membrane channels exist in all organisms from bacteria to humans (Hamill and Martinac, 2001). Application of a mild, hydrodynamic shear stress (unable to detach cells from the substrate ) to *Dicytostelium* triggers a cellular response consisting of steady membrane peeling at the rear edge of the cell and periodic cell contact extensions at its front edge (146). When the flow is reversed, cells respond almost instantaneously and move in the opposite direction. The origin of the signaling taking place is still unknown (145). One possible reason for this behavior may be the mechanical deformation of the actin cortex, which results in protein recruitment at the most stressed side of the cell. We propose to apply our TFC techniques on single *Dictyostelium* cells under steady state, shear stress to further investigate the shear flow response in terms of distribution and dynamics of traction stresses and adhesions as well as F-actin localization. We believe that such a study could shed light on the mechanism behind the specific behavior of *Dictyostelium* on shear flow.

By studying neutrophils, Houk et al. intended to answer why cells establish a single zone of actin assembly at their front during migration (147). They showed that diffusion-based mechanisms are not sufficient for long-range inhibition by the pseudopod. Through their experiments involving micropipette aspiration, they y concluded that tension, rather than diffusible molecules generated or sequestered at the leading edge, is the dominant, long-range inhibitor that constrains the spread of the existing front and prevents the formation of secondary fronts (147). Another interesting experiment, to perform in neutrophils and potentially in *Dictyostelium*, would be to induce deformation locally at the cell's body by aspiring it (suction) with a definite amount of pressure thereby increasing its surface tension), using a microaspirator. At the same time, TFC could be performed to calculate the traction stresses together with tracking of the localization of some fluorescent marker, for instance for F-actin or MyoII. The specific experiment would demonstrate what occurs when surface tension is increased in terms of both F-actin localization and stress application. Another alternative would be the use of both hypertonic and hypotonic buffers to understand the mechanical effect of decreased (cell shrinks) and increased (cell expands) surface tension on cell migration (148). Nevertheless, we would need to make sure that the components used in the buffer do not affect other aspects (chemical) of the cell.

### 7.2.5 Switch from single cell migration to collective: (a) multiple cells on the row and slug; (b) monolayer; (c) cancer

The life cycle of *Dictyostelium* consists of the vegetative and the developmental phase (149). In the presence of adequate levels of nutrients, *Dictyostelium* cells exist as undifferentiated, single cells capable of dividing indefinitely by mitosis every ~6 hr and of exhibiting random motility (149). The developmental phase can be induced by starvation (environment becoming depleted of nutrients). The amoebas then stop dividing and start responding to the depleted levels of nutrients by attracting other starving cells chemotactically with pulses of extracellular cAMP. It is in this specific phase that we record where the cells migrate as single cells. As time passes (>3hr), the cAMP signal is amplified by the cells which start migrating towards each other (forming streams) and eventually towards the aggregation center where they form a mound of cells. The formation of the multicellular aggregate (slug) marks the developmental phase (149). Various groups have focused their studies on the migration of the *Dictyostelium* slug (99, 150), since coordinated movements of cells is a topic of great interest aimed at contributing to the understanding of tissue development and repair. Using our techniques, we can investigate: (a) The mechanics of migration of *Dictyostelium* cells just as they start streaming (two or three cells on a row); (b) The mechanics of migration of slugs. This study can shed light onto the changes in the migration mechanism between single and progressively collective cell migration. It could also contribute in understanding whether there are any advantages and if so, which ones in the choice of cells to move collectively (for instance more efficient migration). Nevertheless, cell-cell interactions have to be taken into account, which could potentially complicate the problem.

Finally, collective cell migration can also be studied in the context of different cell types that are more medically relevant. Epithelial wound healing and cancer are two areas where understanding the mechanics of collective cell migration is crucial. Recent works have investigated traction force organization and have identified coherent motions during the migration of cell monolayers (151-153). There is still much more to learn about the mechanics and rules of collective cell migration and many limitations/restrictions that prevent in depth studies of the specific process. First, there is the need to obtain detailed information about the coupling between the dynamics of cell-cell and cell-substrate interaction. Second, as discussed earlier, the need to mimic the real environment of the cells and develop the appropriate techniques and tools to analyze migration in that case (ie cancer cells in 3D matrices).

## 7.3 Conclusion

The overall objective of the studies carried out and presented in this Dissertation was to investigate and determine in a quantitative manner the spatiotemporal relationship between the mechanical events and the biochemical processes taking place during amoeboid cell migration. For that purpose, we have used Microscopy and Fourier Traction Force Cytometry techniques to calculate the traction stresses exerted by *Dictyostelium discoideum* amoeboid cells on the substrate on which they migrate. We have used a number of mutants and compared their mechanical phenotype to that of wild type, aiming to elucidate the role and importance of key cytoskeletal proteins in the mechanics of cell migration.

We found that for all the strains under study, the migrating cells attached at a reduced number of adhesion sites and contracted the substrate inwards, consistent with the idea of the cytoskeleton being subjected to internal tension. We confirmed that for wild type and a range of mutants the strength of the traction stresses and the cell length follow a quasi-periodic temporal evolution. This quasi-periodic evolution supports and confirms the idea that amoeboid cells move by following discrete repetitive steps, termed as phases of their motility cycle. In addition, we found for the first time that these oscillations are highly correlated with the maximum fluorescence of F-actin at the frontal cell edge.

Nevertheless, unlike previous studies we found that not all cells move periodically. Cells with misregulated SCAR/WAVE-mediated dendritic F-actin polymerization at the cell’s leading edge, are unable to move periodically, which renders the efficiency of their migration really poor. By measuring and comparing the traction stresses of wild-type *Dictyostelium* cells with cells lacking the SCAR/WAVE complex proteins PIR121 (*pirA*$^-$) and SCAR (*scrA*$^-$), we found that, compared to the wild-type, both mutant strains exert stresses of different strength that correlate with their levels of F-actin, suggesting that F-actin is a key determinant of the traction stress strength.

In addition to the use of the Fourier Traction Force Microscopy (FTFM) to measure the spatiotemporal evolution of shape and traction stress dynamics during migration, we constructed traction tension kymographs. The kymographic representation of the traction stresses allowed us to to determine, for the first time, how the formation and disassembly of adhesions are coupled with the generation of axial and lateral traction stresses to control cell migration. We showed that wild-type cells migrate by switching between two motility modes with distinct adhesion and contractility dynamics. In the “*Stepping-Stepping”* mode, the adhesion sites remain stationary while the body moves forward by periodic axial contractions. The back adhesions break after new frontal adhesions are formed. In the *“Stepping-Gliding”* mode, the cell reduces the magnitude of the traction stresses, increases the frequency of axial contractions and its migration speed, and keeps the frontal adhesion stationary while sliding the back adhesion forward.

We showed that these two motility modes are not conserved when cells move on highly adhesive poly-L-lysine coated substrates, where cells alternate between a *"Nearly Stationary"* mode, characterized by strong lateral contractions and extremely low migration speed and a *"Gliding-Gliding"* mode where multiple weak and transient adhesions are formed which are gliding forward as the cell moves by barely adhering at the substrate. We thus showed that the cells migrate not only by contracting axially but also perpendicularly to their direction of motion and that the ability of the cells to contract laterally is crucial when migration occurs under conditions of increased adherence. We also showed that cells can adjust the way they move in distinct ways to achieve efficient migration when their environment (substrate adhesivity and stiffness) is altered.

Finally, we found that cells with cytoskeletal crosslinking defects (*mhcA*$^-$ and *abp120*$^-$ cells), also move by developing increased lateral contractility implementing distinct motility modes, which slightly differ from those observed in wild-type cells. Surprisingly, we found that these cells are unable to move on highly adhesive substrates. In the case of *mhcA*$^-$ cells, we identified that the reason for that is the inability of the cells to increase their traction stress strength suggesting that the increased lateral contraction observed in wild-type is originated from the action of the MyoII motor. Unlike *mhcA*$^-$ cells, we found that *abp120*$^-$ cell increase their traction stress strength on highly adhesive substrates but not enough to be able to migrate, which underlines the importance of the cytoskeletal integrity in the migration process.

In summary, we have contributed to a more precise understanding of the mechanics of the amoeboid cell migration and the specific roles of key cytoskeletal proteins in the above process. We believe that these are highly conserved mechanisms that function in a range of amoeboid cells, including leukocytes, as well as other forms of cell motility. Cell migration is known to be central in many pathological processes such as cancer metastasis and inflammatory diseases, both of which are still poorly understood and remain partially treated. It is thus of major importance through a multidisciplinary approach to investigate the causes of the aforementioned diseases starting from the origin: “How does the cell migrate?”. Only then will we be able to control and predict cell migration, finding novel therapeutic approaches and efficient treatments.

# References

1. Lauffenburger D.A., Horwitz A.F.: Cell migration: a physically integrated molecular process. Cell, 84, 359-369, 1996.

2. Ridley A.J., Schwartz M.A., Burridge K., Firtel R.A., Ginsberg M.H., Borisy G., Parsons J.T., Horwitz A.R.: Cell migration: integrating signals from front to back. Science, 302, 1704-1709, 2003.

3. Pollard T.D., Borisy G.G.: Cellular motility driven by assembly and disassembly of actin filaments. Cell, 112, 453-465, 2003.

4. Wallingford J.B., Fraser S.E., Harland R.M.: Convergent Extension: The Molecular Control of Polarized Cell Movement during Embryonic Development. Developmental Cell, 2, 695-706, 2002.

5. Discher D., Janmey P., Wang Y.: Tissue cells feel and respond to the stiffness of their substrate. 1139-1143, 2005.

6. Martin P.: Wound healing - Aiming for perfect skin regeneration. Science, 276, 75-81, 1997.

7. Miller M., Wei S., Parker I., Cahalan M.: Two-photon imaging of lymphocyte motility and antigen response in intact lymph node. Science, 296, 1869-1873, 2002.

8. Geiger B., Bershadsky A., Pankov R., Yamada K.: Transmembrane extracellular matrix-cytoskeleton crosstalk. Nat Rev Mol Cell Biol, 2, 793-805, 2001.

9. Luster A., Alon R., von Andrian U.: Immune cell migration in inflammation: present and future therapeutic targets. Nat. Immunol., 2005, pp. 1182-1190.

10. Gillette B., Jensen J., Tang B., Yang G., Bazargan-Lari A., Zhong M., Sia S.: In situ collagen assembly for integrating microfabricated three-dimensional cell-seeded matrices. Nature Mater., 7, 636-640, 2008.

11. Kumar S., Weaver V.: Mechanics, malignancy, and metastasis. Cancer Metastasis Rev, 2009, pp. 113–127.

12. Machesky L.M.: Lamellipodia and filopodia in metastasis and invasion. FEBS Letters, 582, 2102-2111, 2008.

13. Yamaguchi H., Wyckoff J., Condeelis J.: Cell migration in tumors. Current Opinion in Cell Biology, 17, 559-564, 2005.

14. Chien S., Li S., Shiu Y.T., Li Y.S.: Molecular basis of mechanical modulation of endothelial cell migration. Front Biosci, 10, 1985-2000, 2005.

15. Zigmond S., Hirsch J.: Leukocyte locomotion and chemotaxis. New methods for evaluation, and demonstration of a cell-derived chemotactic factor. J Exp Med, 137, 387-410, 1973.

16. Kraemer R.: Regulation of cell migration in atherosclerosis. Current Atherosclerosis Reports, 2, 445-452, 2000.

17. Sánchez-Madrid F., del Pozo M.: Leukocyte polarization in cell migration and immune interactions. EMBO J., 1999.

18. Del Pozo M., Price L., Alderson N., Ren X., Schwartz M.: Adhesion to the extracellular matrix regulates the coupling of the small GTPase Rac to its effector PAK. EMBO J, 19, 2008-2014, 2000.

19. Griffith L., Naughton G.: Tissue Engineering--Current Challenges and Expanding Opportunities. Science, 2002, pp. 1009-1014.

20. Bray D.: Cell movements; from molecules to motility. Garland Pub., New York, second edition, 2001.

21. Small J.V., Stradal T., Vignal E., Rottner K.: The lamellipodium: where motility begins. Trends in Cell Biology, 12, 112-120, 2002.

22. Friedl P., Borgmann S., Brocker E.: Amoeboid leukocyte crawling through extracellular matrix: lessons from the Dictyostelium paradigm of cell movement. J Leukoc Biol, 70, 491-509, 2001.

23. Cukierman E., Pankov R., Stevens D., Yamada M.: Taking cell-matrix adhesions to the third dimension. Science, 2001, pp. 1708-1712.

24. Dembo M., Oliver T., Ishihara A., Jacobson K.: Imaging the traction stresses exerted by locomoting cells with the elastic substratum method. Biophys J, 70, 2008-2022, 1996.

25. Lombardi M.L., Knecht D.A., Dembo M., Lee J.: Traction force microscopy in Dictyostelium reveals distinct roles for myosin II motor and actin-crosslinking activity in polarized cell movement. J Cell Sci, 120, 1624-1634, 2007.

26. Oliver T., Dembo M., Jacobson K.: Traction forces in locomoting cells. Cell Motil. Cytoskeleton, 31, 225-240, 1995.

27. Landau L.D., Lifshitz E.M.: Theory of elasticity, 1970.

28. Butler J.P., Tolic-Norrelykke I.M., Fabry B., Fredberg J.J.: Traction fields, moments, and strain energy that cells exert on their surroundings. American Journal of Physiology-Cell Physiology, 282, C595-C605, 2002.

29. del Álamo J.C., Meili R., Alonso-Latorre B., Rodríguez-Rodríguez J., Aliseda A., Firtel R.A., Lasheras J.C.: Spatio-temporal analysis of eukaryotic cell motility by improved force cytometry. Proc. Nat. Acad. Sci., 104, 13343-13348, 2007.

30. Alonso-Latorre B., Meili R., Bastounis E., Del Alamo J.C., Firtel R.A., Lasheras J.C.: Distribution of traction forces and intracellular markers associated with shape changes during amoeboid cell migration. 31th Annual International Conference of the IEEE Engineering in Medicine and Biology Society, 3346-3349, 2009.

31. Meili R., Alonso-Latorre B., Álamo J.C.d., Firtel R.A., Lasheras J.C.: Myosin II is Essential for the Spatiotemporal Organization of Traction Forces during Cell Motility. MBoC, 21, 405-417, 2010.

32. Li S., Guan J.L., Chien S.: Biochemistry and biomechanics of cell motility. Annu Rev Biomed Eng, 7, 105-150, 2005.

33. Webb D.J., Parsons J.T., Horwitz A.F.: Adhesion assembly, disassembly and turnover in migrating cells - over and over and over again. Nat. Cell Biol., 4, E97-E100, 2002.

34. Trepat X., Lenormand G., Fredberg J.J.: Universality in cell mechanics. Soft Matter, 4, 1750-1759, 2008.

35. Bastounis E., Meili R., Alonso-Latorre B., del Álamo J., Lasheras J., Firtel R.: The SCAR/WAVE complex is necessary for proper regulation of traction stresses during amoeboid motility. Mol Biol Cell, 21, 3995–4003, 2011.

36. Charest P.G., Firtel R.A.: Big roles for small GTPases in the control of directed cell movement. Biochem. J., 401, 377-390, 2007.

37. Uchida K.S., Kitanishi-Yumura T., Yumura S.: Myosin II contributes to the posterior contraction and the anterior extension during the retraction phase in migrating Dictyostelium cells. J. Cell Biol., 116, 51-60, 2003.

38. Uchida K.S., Yumura S.: Dynamics of novel feet of Dictyostelium cells during migration. J. Cell Sci., 117, 1443-1455, 2004.

39. Wessels D., Voss E., Von Bergen N., Burns R., Stites J., Soll D.: A computer-assisted system for reconstructing and interpreting the dynamic three-dimensional relationships of the outer surface, nucleus and pseudopods of crawling cells. Cell Motil. Cytoskeleton, 41, 225-246, 1998.

40. Wessels D., Vawter-Hugart H., Murray J., Soll D.: Three-dimensional dynamics of pseudopod formation and the regulation of turning during the motility cycle of Dictyostelium. Cell Motil. Cytoskeleton, 27, 1-12, 1994.

41. John Murray H.V.-H.E.V.D.R.S.: Three-dimensional motility cycle in leukocytes. Cell Motil. Cytoskeleton, 22, 211-223, 1992.

42. Felder S., Kam Z.: Human neutrophil motility: time-dependent three-dimensional shape and granule diffusion. Cell Motil Cytoskeleton, 28, 285-302, 1994.

43. Mizuno T., Kagami O., Sakai T., Kawasaki K.: Locomotion of neutrophil fragments occurs by graded radial extension. Cell Motil Cytoskeleton, 35, 289-297, 1996.

44. Shutt D.C., Wessels D., Wagenknecht K., Chandrasekhar A., Hitt A.L., Luna E.J., Soll D.R.: Ponticulin Plays a Role in the Positional Stabilization of Pseudopods. J. Cell Biol., 131, 1495-1506, 1995.

45. Pollard T.D.: Cellular motility powered by actin filament assembly and disassembly. Harvey Lect, 98, 1-17, 2002.

46. Insall R.H., Machesky L.M.: Actin Dynamics at the Leading Edge: From Simple Machinery to Complex Networks. Developmental Cell, 17, 310-322, 2009.

47. Pollard T.D.: The cytoskeleton, cellular motility and the reductionist agenda. Nature, 422, 741-745, 2003.

48. Pollard T.: Regulation of actin filament assembly by arp2/3 complex and formins. Annu. Rev. Biophys. Biomol. Struct., 36, 451-477, 2007.

49. Svitkina T.M., Borisy G.G.: Arp2/3 complex and actin depolymerizing factor/cofilin in dendritic organization and treadmilling of actin filament array in lamellipodia. J Cell Biol, 145, 1009-1026, 1999.

50. Higgs H., Pollard T.: Regulation of actin filament network formation through Arp2/3 complex: Activation by a diverse array of proteins. Annu Rev Biochem, 70, 649-676, 2001.

51. Miller K.G.: Extending the Arp2/3 complex and its regulation beyond the leading edge. J Cell Biol, 156, 591-593, 2002.

52. Beltzner C.C., Pollard T.D.: Identification of functionally important residues of Arp2/3 complex by analysis of homology models from diverse species. Journal of Molecular Biology, 336, 551-565, 2004.

53. Beltzner C.C., Pollard T.D.: Pathway of actin filament branch formation by Arp2/3 complex. Journal of Biological Chemistry, 283, 7135-7144, 2008.

54. Higgs H.N., Pollard T.D.: Regulation of actin filament network formation through ARP2/3 complex: activation by a diverse array of proteins. Annu. Rev. Biochem., 70, 649-676, 2001.

55. Kiselar J.G., Mahaffy R., Pollard T.D., Almo S.C., Chance M.R.: Visualizing Arp2/3 complex activation mediated by binding of ATP and WASp using structural mass spectrometry. Proceedings of the National Academy of Sciences of the United States of America, 104, 1552-1557, 2007.

56. Mullins R.D., Heuser J.A., Pollard T.D.: The interaction of Arp2/3 complex with actin: nucleation, high affinity pointed end capping, and formation of branching networks of filaments. Proc. Nat. Acad. Sci., 95, 6181-6186, 1998.

57. Pollard T.D., Beltzner C.C.: Structure and function of the Arp2/3 complex. Current Opinion in Structural Biology, 12, 768-774, 2002.

58. Ibarra N., Insall R.H.: Regulation of actin assembly by SCAR/WAVE proteins. Biochem Soc Trans, 33, 1243-1246, 2005.

59. Machesky L.M., Insall R.H.: Scar1 and the related Wiskott-Aldrich syndrome protein, WASP, regulate the actin cytoskeleton through the Arp2/3 complex. Curr. Biol., 8, 1347-1356, 1998.

60. Moreau V., Frischknecht F., Reckmann I., Vincentelli R., Rabut G., Stewart D., Way M.: A complex of N-WASP and WIP integrates signalling cascades that lead to actin polymerization. Nat Cell Biol, 2, 441-448, 2000.

61. Miki H., Miura K., Takenawa T.: N-WASP, a novel actin-depolymerizing protein, regulates the cortical cytoskeletal rearrangement in a PIP2-dependent manner downstream of tyrosine kinases. EMBO J., 15, 5326-5335, 1996.

62. Miki H., Suetsugu S., Takenawa T.: WAVE, a novel WASP-family protein involved in actin reorganization induced by Rac. EMBO J., 17, 6932-6941, 1998.

63. Miki H., Takenawa T.: Regulation of actin dynamics by WASP family proteins. J. Biochem., 134, 309-313, 2003.

64. Mullins R.D.: How WASP-family proteins and the Arp2/3 complex convert intracellular signals into cytoskeletal structures. Curr Opin Cell Biol, 12, 91-96, 2000.

65. Myers S.A., Han J.W., Lee Y., Firtel R.A., Chung C.Y.: A Dictyostelium homologue of WASP is required for polarized F-actin assembly during chemotaxis. Mol. Biol. Cell, 16, 2191-2206, 2005.

66. Ibarra N., Blagg S.L., Vazquez F., Insall R.H.: Nap1 regulates Dictyostelium cell motility and adhesion through SCAR-dependent and -independent pathways. Curr Biol, 16, 717-722, 2006.

67. Basu D., El-Assal S.E.D., Le J., Mallery E.L., Szymanski D.B.: Interchangeable functions of Arabidopsis PIROGI and the human WAVE complex subunit SRA1 during leaf epidermal development. Development, 131, 4345-4355, 2004.

68. Cory G.O., Ridley A.J.: Cell motility: braking WAVEs. Nature, 418, 732-733, 2002.

69. Davidson A.J., Insall R.H.: Actin-Based Motility: WAVE Regulatory Complex Structure Reopens Old SCARs. Current Biology, 21, R66-R68, 2011.

70. Cox D., Condeelis J.S., Wessels D., Soll D.R., Kern H., Knecht D.A.: Targeted disruption of the ABP-120 gene leads to cells with altered motility. J Cell Biol, 116, 943-955, 1992.

71. Cox D., Ridsdale J.A., Condeelis J.S., Hartwig J.: Genetic deletion of ABP-120 alters the three-dimensional organization of actin filaments in Dictyostelium pseudopods. J Cell Biol, 128, 819-835, 1995.

72. Cunningham C.C., Gorlin J.B., Kwiatkowski D.J., Hartwig J.H., Janmey P.A., Byers H.R., Stossel T.P.: Actin-binding protein requirement for cortical stability and efficient locomotion. Science, 255, 325-327, 1992.

73. Janssen K.P., Eichinger L., Janmey P.A., Noegel A.A., Schliwa M., Witke W., Schleicher M.: Viscoelastic properties of F-actin solutions in the presence of normal and mutated actin-binding proteins. Arch Biochem Biophys, 325, 183-189, 1996.

74. Kicka S., Shen Z., Annesley S.J., Fisher P.R., Lee S., Briggs S., Firtel R.A.: The LRRK2-related Roco kinase Roco2 is regulated by Rab1A and controls the actin cytoskeleton. Mol Biol Cell, 22, 2198-2211, 2011.

75. De Lozanne A., Spudich J.A.: Disruption of the Dictyostelium myosin heavy chain gene by homologous recombination. Science, 236, 1086-1091, 1987.

76. Chen P., Ostrow B.D., Tafuri S.R., Chisholm R.L.: Targeted disruption of the Dictyostelium RMLC gene produces cells defective in cytokinesis and development. J Cell Biol, 127, 1933-1944, 1994.

77. Bosgraaf L., van Haastert P.J.: The regulation of myosin II in Dictyostelium. Eur. J. Cell Biol., 85, 969-979, 2006.

78. Pollenz R., Chen T., Trivinos-Lagos L., Chisholm R.: The Dictyostelium essential light chain is required for myosin function. Cell, 69, 951-962, 1992.

79. Fukui Y., Yumura S.: Actomyosin dynamics in chemotactic amoeboid movement of Dictyostelium. Cell Motility and the Cytoskeleton, 6, 662-673, 1986.

80. Jay P.Y., Pham P.A., Wong S.A., Elson E.L.: A mechanical function of myosin II in cell motility. J Cell Sci, 108, 387-393, 1995.

81. Huttenlocher A., Sandborg R.R., Horwitz A.F.: Adhesion in cell migration. Curr Opin Cell Biol, 7, 697-706, 1995.

82. Balaban N.Q., Schwarz U.S., Riveline D., Goichberg P., Tzur G., Sabanay I., Mahalu D., Safran S., Bershadsky A.D., Addadi L., Geiger B.: Force and focal adhesion assembly: a close relationship studied using elastic micropatterned substrates. Nat Cell Biol, 3, 466-472, 2001.

83. Gov N.S.: Modeling the size distribution of focal adhesions. Biophys J, 91, 2844-2847, 2006.

84. Cornillon S., Gebbie L., Benghezal M., Nair P., Keller S., Wehrle-Haller B., Charette S.J., Brückert F., Letourneur F., Cosson P.: An adhesion molecule in free-living Dictyostelium amoebae with integrin beta features. EMBO Rep, 7, 617-621, 2006.

85. Weber I., Wallraff E., Albrecht R., Gerisch G.: Motility and substratum adhesion of Dictyostelium wild-type and cytoskeletal mutant cells: a study by RICM/bright-field double-view image analysis. J Cell Sci, 108, 1519-1530, 1995.

86. Engler A. B.L., Newman C.,Hategan A., Griffin M., Discher D.: Substrate Compliance versus Ligand Density in Cell on Gel Responses. Biophysical Journal, 2004, pp. 617-628.

87. Wang Y.L., Pelham R.L.J.: Preparation of a flexible, porous polyacrylamide substrate for mechanical studies of cultured cells. 1998, pp. 489-496.

88. Jay P.Y., Pham P.A., Wong S.A., Elson E.L.: A mechanical function of myosin II in cell motility. J Cell Sci, 108 ( Pt 1), 387-393, 1995.

89. Alonso-Latorre B.: Force and shape coordination in amoeboid cell motility. Mechanical and Aerospace Engineering. PQDT, University of California, San Diego, 2010, p. 152.

90. Tse J., Engler A.: Stiffness Gradients Mimicking In Vivo Tissue Variation Regulate Mesenchymal Stem Cell Fate. PLoS ONE, 6, e15978, 2011.

91. Gui L., Wereley S.T.: A correlation-based continuous window-shift technique to reduce the peak-locking effect in digital PIV image evaluation. Exp. Fluids, 32, 506-517, 2002.

92. Willert C.E., Gharib M.: Digital particle image velocimetry. Experiments in Fluids, 10, 181-193, 1991.

93. Bastounis E., Meili R., Alonso-Latorre B., del Álamo J., Lasheras J., Firtel R.: The SCAR/WAVE complex is necessary for proper regulation of traction stresses during amoeboid motility. Mol Biol Cell., 2011, pp. 3995–4003.

94. Adam E., Lucie B., Cynthia N., Alina H., Maureen G., Dennis D.: Substrate Compliance versus Ligand Density in Cell on Gel Responses. Biophysical Journal, 2004, pp. 617-628.

95. Frey M.T., Engler A.J., Discher D.E., Lee J., Wang Y.L.: Microscopic methods for measuring the elasticity of gel substrates for cell culture: microspheres, microindenters, and atomic force microscopy. Methods Cell Biol, 83, 47-65, 2007.

96. Alonso-Latorre B.: Force and shape coordination in amoeboid cell motility. PhD Thesis, University of California, San Diego, 2010.

97. Tamim N., Ghani F.: Techniques for optimization in time delay

estimation from cross correlation function. IJET-IJENS, 2010, pp. 69-75.

98. Abercrombie M., Heaysman J., Pegrum S.: The locomotion of fibroblasts in culture. I. Movements of the leading edge. Exp Cell Res, 59, 393-398, 1970.

99. Rieu J.P., Barentin C., Maeda Y., Sawada Y.: Direct mechanical force measurements during the migration of Dictyostelium slugs using flexible substrata. Biophys. J., 89, 3563-3576, 2005.

100. Pollard T.D., Borisy G.G.: Cellular motility driven by assembly and disassembly of actin filaments (vol 112, pg 453, 2002). Cell, 113, 549-549, 2003.

101. Dimilla P.A., Barbee K., Lauffenburger D.A.: Mathematical-model for the effects of adhesion and mechanics on cell migration speed. Biophys, 60, 15-37, 1991.

102. Galbraith C.G., Sheetz M.P.: Forces on adhesive contacts affect cell function. Curr Opin Cell Biol, 10, 566-571, 1998.

103. Jacobelli J., Bennett F.C., Pandurangi P., Tooley A.J., Krummel M.F.: Myosin-IIA and ICAM-1 regulate the interchange between two distinct modes of T cell migration. J Immunol, 182, 2041-2050, 2009.

104. Li L., Nørrelykke S.F., Cox E.C.: Persistent cell motion in the absence of external signals: a search strategy for eukaryotic cells. PLoS ONE, 3, e2093, 2008.

105. Palecek S.P., Loftus J.C., Ginsberg M.H., Lauffenburger D.A., Horwitz A.F.: Integrin-ligand binding properties govern cell migration speed through cell-substratum adhesiveness. Nature, 385, 537-540, 1997.

106. Weber I., Wallraff E., Albrecht R., Gerisch G.: Motility and substratum adhesion of Dictyostelium wild-type and cytoskeletal mutant cells: a study by RICM/bright-field double-view image analysis. J Cell Sci, 108 ( Pt 4), 1519-1530, 1995.

107. Fukui Y.: Mechanistics of amoeboid locomotion: signal to forces. Cell Biol Int, 26, 933-944, 2002.

108. Wessels D., Soll D., Knecht D., Loomis W., De Lozanne A., Spudich J.: Cell motility and chemotaxis in Dictyostelium amebae lacking myosin heavy chain. Dev. Biol., 128, 164-177, 1988.

109. Tuxworth R., Stephens S., Ryan Z., Titus M.: Identification of a myosin VII-talin complex. J. Biol. Chem., 280, 26557-26564, 2005.

110. Yumura S., Kitanishi-Yumura T.: Release of myosin II from the membrane-cytoskeleton of Dictyostelium discoideum mediated by heavy-chain phosphorylation at the foci within the cortical actin network. J. Cell Biol., 117, 1231-1239, 1992.

111. Iwadate Y., Yumura S.: Actin-based propulsive forces and myosin-II-based contractile forces in migrating Dictyostelium cells. J Cell Sci, 121, 1314-1324, 2008.

112. Devreotes P.N., Zigmond S.H.: Chemotaxis in eukaryotic cells - a focus on leukocytes and dictyostelium. Ann Rev Cell Biology, 4, 649-686, 1988.

113. Trappmann B., Gautrot J.E., Connelly J.T., Strange D.G.T., Li Y., Oyen M.L., Cohen Stuart M.A., Boehm H., Li B., Vogel V., Spatz J.P., Watt F.M., Huck W.T.S.: Extracellular-matrix tethering regulates stem-cell fate. Nat Mater, 11, 642-649, 2012.

114. Sahai E., Marshall C.J.: Differing modes of tumour cell invasion have distinct requirements for Rho/ROCK signalling and extracellular proteolysis. Nat Cell Biol, 5, 711-719, 2003.

115. Ibarra N., Pollitt A., Insall R.: Regulation of actin assembly by SCAR/WAVE proteins. Biochem. Soc. Trans., 33, 1243-1246, 2005.

116. Bear J.E., Rawls J.F., Saxe C.L.: SCAR, a WASP-related protein, isolated as a suppressor of receptor defects in late Dictyostelium development. J Cell Biol, 142, 1325-1335, 1998.

117. Blagg S.L., Stewart M., Sambles C., Insall R.H.: PIR121 regulates pseudopod dynamics and SCAR activity in Dictyostelium. Curr Biol, 13, 1480-1487, 2003.

118. Pollitt A.Y., Insall R.H.: Abi Mutants in Dictyostelium Reveal Specific Roles for the SCAR/WAVE Complex in Cytokinesis. Current Biology, 18, 203-210, 2008.

119. King JS V.D., Georgiou M, Baum B, Insall RH.: SCAR/WAVE is activated at mitosis and drives myosin-independent cytokinesis. J Cell Sci., 2010, pp. 2246-2255.

120. Condeelis J.S., Hall A.L., Bresnick A.R., Warren V., Hock R., Bennett H., Ogihara S.: Actin polymerization and pseudopod extension during amoeboid chemotaxis. Cell Motil Cytoskeleton, 10, 77-90, 1988.

121. Riedl J., Crevenna A.H., Kessenbrock K., Yu J.H., Neukirchen D., Bista M., Bradke F., Jenne D., Holak T.A., Werb Z., Sixt M., Wedlich-Soldner R.: Lifeact: a versatile marker to visualize F-actin. Nat Meth, 5, 605-607, 2008.

122. Lasheras J.C., Alonso-Latorre B., Meili R., Bastounis E., del Alamo J.C., Firtel R.A.: Distribution of traction forces and intracellular markers associated with shape changes during amoeboid cell migration. International Journal of Transport Phenomena, 2010.

123. Egelhoff T., Naismith T., Brozovich F.: Myosin-based cortical tension in Dictyostelium resolved into heavy and light chain-regulated components. J Muscle Res Cell Motil, 1996, pp. 269-274.

124. Kasza K.E., Nakamura F., Hu S., Kollmannsberger P., Bonakdar N., Fabry B., Stossel T.P., Wang N., Weitz D.A.: Filamin A Is Essential for Active Cell Stiffening but not Passive Stiffening under External Force. Biophysical Journal, 96, 4326-4335, 2009.

125. Katoh H., Negishi M.: RhoG activates Rac1 by direct interaction with the Dock180-binding protein Elmo. Nature, 424, 461-464, 2003.

126. Cox D., Wessels D., Soll D.R., Hartwig J., Condeelis J.: Re-expression of ABP-120 rescues cytoskeletal, motility, and phagocytosis defects of ABP-120(-) Dictyostelium mutants. Molecular Biology of the Cell, 7, 803-823, 1996.

127. Lasheras J.C., Alonso-Latorre B., Meili R., Bastounis E., del Alamo J.C., Firtel R.A.: Distribution of traction forces and intracellular markers associated with shape changes during amoeboid cell migration. Internat J Transport Phenomena, 12, 3-12, 2011.

128. Kasza K.E., Nakamura F., Hu S., Kollmannsberger P., Bonakdar N., Fabry B., Stossel T.P., Wang N., Weitz D.A.: Filamin A is essential for active cell stiffening but not passive stiffening under external force. Biophys, 96, 4326-4335, 2009.

129. Jannat R., Robbins P., Ricart G., Dembo M., Hammer D.: Neutrophil adhesion and chemotaxis depend on substrate mechanics. J. Phys.: Condens. Matter, 2010, p. 194117.

130. Engler A., Bacakova L., Newman C., Hategan A., Griffin M., Discher D.: Substrate compliance versus ligand density in cell on gel responses. Biophys, 2004, pp. 617-628.

131. Barnhart E.L., Lee K.-C., Keren K., Mogilner A., Theriot J.A.: An Adhesion-Dependent Switch between Mechanisms That Determine Motile Cell Shape. PLoS Biol, 9, e1001059, 2011.

132. Balaban N., Schwarz U., Riveline D., Goichberg P., Tzur G., Sabanay I., Mahalu D., Safran S., Bershadsky A., Addadi L., Geiger B.: Force and focal adhesion assembly: a close relationship studied using elastic micropatterned substrates. Nat Cell Biol, 3, 466-472, 2001.

133. Lo C., Wang H., Dembo M., Wang Y.: Cell movement is guided by the rigidity of the substrate. Biophys J, 79, 144-152, 2000.

134. Merkel R., Kirchgeßner N., Cesa C.M., Hoffmann B.: Cell Force Microscopy on Elastic Layers of Finite Thickness. Biophys J, 93, 3314-3323, 2007.

135. Tse J.R., Engler A.J.: Stiffness Gradients Mimicking In Vivo Tissue Variation Regulate Mesenchymal Stem Cell Fate. PLoS ONE, 6, e15978, 2011.

136. Fukui Y., Murray J., Riddelle K.S., Soll D.R.: Cell behavior and actomyosin organization in Dictyostelium during substrate exploration. Cell Struct Funct, 16, 289-301, 1991.

137. Cingolani L.A., Goda Y.: Actin in action: the interplay between the actin cytoskeleton and synaptic efficacy. Nat Rev Neurosci, 9, 344-356, 2008.

138. Lucas-Lopez C., Allingham J.S., Lebl T., Lawson C.P., Brenk R., Sellers J.R., Rayment I., Westwood N.J.: The small molecule tool (S)-(-)-blebbistatin: novel insights of relevance to myosin inhibitor design. Org Biomol Chem, 6, 2076-2084, 2008.

139. Steimle P.A., Yumura S., Cote G.P., Medley Q.G., Polyakov M.V., Leppert B., Egelhoff T.T.: Recruitment of a myosin heavy chain kinase to actin-rich protrusions in Dictyostelium. Current biology, 11, 708-713, 2001.

140. del Alamo J., Alvarez-Gonzalez B., Meili R., Alonso-Latorre B., Firtel R., Lasheras J.: Three-dimensional traction force distribution in migrating amoeboid cells. Bulletin of the American Physical Society, 2011.

141. Franck C., Maskarinec S.A., Tirrell D.A., Ravichandran G.: Three-Dimensional Traction Force Microscopy: A New Tool for Quantifying Cell-Matrix Interactions. PLoS ONE, 6, e17833, 2011.

142. Lammerding J., Hsiao J., Schulze P.C., Kozlov S., Stewart C.L., Lee R.T.: Abnormal nuclear shape and impaired mechanotransduction in emerin-deficient cells. *J. Cell Biol.*, 2005, pp. 781-791.

143. Baker E.L., Srivastava J., Yu D., Bonnecaze R.T., Zaman M.H.: Cancer Cell Migration: Integrated Roles of Matrix Mechanics and Transforming Potential. PLoS ONE, 6, e20355, 2011.

144. Wolf K., Wu Y.I., Liu Y., Geiger J., Tam E., Overall C., Stack M.S., Friedl P.: Multi-step pericellular proteolysis controls the transition from individual to collective cancer cell invasion. Nat Cell Biol, 9, 893-904, 2007.

145. Decave E., Rieu D., Dalous J., Fache S., Brechet Y., Fourcade B., Satre M., Bruckert F.: Shear flow-induced motility of Dictyostelium discoideum cells on solid substrate. J. Cell Sci., 116, 4331-4343, 2003.

146. Decave E., Garrivier D., Brechet Y., Fourcade B., Bruckert F.: Shear flow-induced detachment kinetics of Dictyostelium discoideum cells from solid substrate. Biophysical Journal, 82, 2383-2395, 2002.

147. Houk Andrew R., Jilkine A., Mejean Cecile O., Boltyanskiy R., Dufresne Eric R., Angenent Sigurd B., Altschuler Steven J., Wu Lani F., Weiner Orion D.: Membrane Tension Maintains Cell Polarity by Confining Signals to the Leading Edge during Neutrophil Migration. Cell, 148, 175-188, 2012.

148. Du F., Edwards K., Shen Z., Sun B., De Lozanne A., Briggs S., Firtel R.A.: Regulation of contractile vacuole formation and activity in Dictyostelium. EMBO J, 27, 2064-2076, 2008.

149. Loomis W.F.: The development of Dictyostelium discoideum. New York: Ac. Press., 1982.

150. Vasiev B., Weijer C.J.: Modelling of Dictyostelium discoideum slug migration. J Theor Biol, 223, 347-359, 2003.

151. Trepat X., Wasserman M.R., Angelini T.E., Millet E., Weitz D.A., Butler J.P., Fredberg J.J.: Physical forces during collective cell migration. Nat Phys, 5, 426-430, 2009.

152. Farooqui R., Fenteany G.: Multiple rows of cells behind an epithelial wound edge extend cryptic lamellipodia to collectively drive cell-sheet movement. J Cell Sci, 118, 51-63, 2005.

153. Gov N.S.: Collective cell migration patterns: Follow the leader. Proc. Nat. Acad. Sci., 2007.